

SPIN AND PARITY ASSIGNMENTS IN ^{34}P USING
THE POLARIZED (d,α) AND $(d,\alpha\gamma)$ REACTIONS

By

© ANNE JANINE TRUDEL

A Thesis

Submitted to the School of Graduate Studies
in Partial Fulfillment of the Requirements

for the Degree

Doctor of Philosophy

McMaster University

January 1987

J^π ASSIGNMENTS IN ³⁴P USING THE (d⁺,αγ) REACTION

DOCTOR OF PHILOSOPHY (1987)
(Physics)

McMASTER UNIVERSITY

TITLE: Spin and Parity Assignments in ^{34}P Using the
Polarized (d,α) and $(d,\alpha\gamma)$ Reactions

AUTHOR: Anne Janine Trudel, B.Sc. (McGill University)

SUPERVISOR: Professor J.A. Kuehner

NUMBER OF PAGES: x, 151

ABSTRACT

A measurement of method II (d, $\alpha\gamma$) angular correlations (LF61), using a polarized deuteron beam is a powerful technique for determining spins and parities in light nuclei, since two separate correlations, corresponding to two beam polarization substates, are measured for each transition and in each case the residual nucleus is left in a strongly polarized state. This technique, together with model-independent parity assignments from T_{20} measurements at zero degrees, has been used to measure the spins and parities of the low-lying excited states in the nucleus ^{34}P . The resulting J^π assignments for these states are well reproduced by a shell model calculation using Wildenthal's usd interaction (Wi82). The effect of the finite particle detector size and the less than completely polarized beam on the measured correlations has been discussed and the results have been incorporated into the final analysis.

ACKNOWLEDGEMENTS

It is difficult to acknowledge all the people who have contributed to making my stay at McMaster a profitable one, however I would like to mention the following;

John Kuehner, my supervisor, for sharing his invaluable experience in all aspects of this work, thus making my task much easier.

The other members of my committee, Drs. R.G. Summers-Gill and G.L. Keech for offering advice and constructive criticism at different stages of this work.

Members of the research group, A.A. Pilt, C.L. Woods, M. Vetterli, N. Davis and C. Bamber for graciously volunteering to help with the lengthy runs, and Dr. Graham Jones for his contributions during the initial stages of this project.

The accelerator operation staff; in particular John McKay for his assistance in appeasing the often temperamental polarized ion source and, Bob McNaught and Hector Blanchard for their much needed expertise in quickly debugging the VAX data acquisition system.

Members of the lab and students of the 'cattlebarn' for sharing their enthusiasm for research and providing stimulating discussions.

The National Sciences and Engineering Research Council for providing financial support in the form of grants and scholarships.

My family for always having shown an interest in my diverse pursuits.

Lastly my husband Ken, without whose love and support this last year would have been much more difficult.

TABLE OF CONTENTS

<u>CHAPTER</u>	<u>Page</u>
INTRODUCTION	4
1. THEORETICAL BASIS FOR EXPERIMENTAL METHODS	4
1.1 Preliminary Definitions	
1.1.1 The Density Matrix and Statistical Tensors	4
1.1.2 Analyzing Powers and Cross-Section	7
1.2 T_{20} for the (\vec{d}, α) Reaction at 0°	8
1.2.1 Introduction	
1.2.2 Analyzing Powers	10
1.3 Angular Correlation Theory	14
1.3.1 The Simple γ -ray Correlation	15
1.3.2 Method II Angular Correlations	17
1.3.3 Method II Correlations with an Unobserved Transition	23
1.3.4 Effect of Polarization and Detector Solid Angle	26
2. THE NUCLEUS ^{34}P	33
2.1 Existing Measurements in ^{34}P	33
2.2 Energy Level Measurements	36
2.2.1 Experimental Set-Up	36
2.2.2 Analysis and Results	41
2.3 Summary	44

(continued)

TABLE OF CONTENTS (continued)

3. T_{20} MEASUREMENTS NEAR 0°	47
3.1 Polarized Beam	47
3.2 Experimental Set-Up	53
3.3 Analysis and Results	54
4. ANGULAR CORRELATION EXPERIMENT	59
4.1 Branching Ratio Measurements	60
4.1.1 Experimental Set-Up	60
4.1.2 Analysis and Results	61
4.2 Method II Angular Correlation Measurements	68
4.2.1 Experimental Set-Up	68
4.2.2 Electronics	74
4.2.3 Coincidence Experiment Analysis	76
4.2.4 Peak-Fitting Procedure	79
4.2.5 Efficiency Correction	84
4.2.6 Results and Discussion	87
4.3 Summary	116
5. SHELL MODEL CALCULATIONS	119
5.1 Introduction	119
5.2 Positive Parity States	125
5.3 Negative Parity States	131
CONCLUSION	136
APPENDIX	140
REFERENCES	149

LIST OF TABLES

<u>TABLES</u>	<u>Page</u>
1.1 - Vector and tensor polarizations for $s=1$ particles.	13
1.2 - Cumulative probability for T_{20} of an unnatural parity state as a function of the deviations Δ from the limits.	13
2.1 - Summary of measured excitation energies in ^{34}P from various studies.	35
4.1 - Gamma-ray branching ratios.	67
4.2 - Resolution measurements for the NaI detectors.	73
4.3 - Peak-fitting parameters corresponding to the regions displayed in Fig. 4.7	81
4.4 - NaI detector relative efficiencies and electronic efficiency correction.	86
4.5 - NaI detector attenuation coefficients.	92
4.6 - Mixing ratios for the transitions $1.61 \rightarrow 0.43$ MeV and 0.43 MeV \rightarrow g.s.	110
4.7 - Summary of spin and parity assignments in ^{34}P .	117
5.1 - Measured and calculated mixing ratios for transitions in ^{34}P .	130

LIST OF FIGURES

<u>FIGURE</u>	<u>Page</u>
1.1 - Diagram showing the notation for a gamma-ray decay following a nuclear reaction.	16
1.2 - Chart of spin assignment ambiguities for method II correlations.	22
1.3 - Diagram showing the notation for a two gamma-ray cascade.	24
2.1 - ΔE spectrum at $\theta_{lab} = 45^\circ$.	38
2.2 - Position spectra at $\theta_{lab} = 45^\circ$.	40
3.1 - Polarized ion source schematic.	49
3.2 - Schematic of the beam transport system.	52
3.3 - Position spectra at $\theta_{lab} = 4^\circ$.	55
3.4 - T_{20} measurements.	57
4.1 - Germanium gamma-ray detector spectrum.	63
4.2 - Germanium detector efficiency curve.	64
4.3 - ^{34}P gamma-ray decay scheme.	66
4.4 - Target chamber schematic.	70
4.5 - Electronics block diagram.	75
4.6 - Gamma-ray projection for the 1.61 MeV level.	78
4.7 - Sample gamma-ray peak shape.	82
4.8 - ^{26}Al angular correlations.	88

(continued)

LIST OF FIGURES (continued)

4.9 -	Method II alpha particle spectra.	90
4.10 -	^{32}P angular correlations.	95
4.11 -	Graph of $\Gamma(E1)$ versus $\Gamma(M2)$ for the 0.43 MeV \rightarrow g.s. transition.	98
4.12 -	Angular correlation for the 0.43 MeV \rightarrow g.s. transition.	100
4.13 -	Angular correlations for the 1.61 MeV \rightarrow g.s. transition.	103
4.14 -	Angular correlations for the 1.61 \rightarrow 0.43 MeV transition.	107
4.15 -	Angular correlation for the transition [1.61 \rightarrow] 0.43 \rightarrow g.s.	108
4.16 -	Angular correlation for the transition 2.23 MeV \rightarrow g.s.	112
4.17 -	Gamma-ray projection for the 4.74 MeV level.	113
4.18 -	Angular correlation for the 4.74 \rightarrow 0.43 MeV transition.	115
5.1 -	Measured and calculated energy level diagrams for ^{34}P .	127

INTRODUCTION

Measured spins and parities of nuclear bound states have provided a good testing ground for different nuclear models which ultimately reflect our understanding of the nuclear force and its manifestation within the nucleus. Methods for determining spins and parities of nuclear levels often involve gamma-ray angular correlation; for example β - γ , γ - γ and particle- γ . These methods provide strong arguments on which to base spin and parity assignments in nuclei since they involve the well-understood electromagnetic interaction which characterizes the gamma-ray decay.

The reaction preceding gamma-ray emission leaves the nucleus in an oriented excited state which is described by the density matrix. Generally, the elements of the density matrix will depend on the reaction mechanism forming the initial state and the constraints placed on detection of the initial decay. In Litherland and Ferguson method II particle-gamma correlations (LF61), the particle is detected in aligned geometry and the density matrix can be completely determined in terms of a few population parameters. With a polarized beam this method becomes even more powerful for

two reasons: (1) for a 0^+ target nucleus, the orientation of the initial state can be determined uniquely from a beam of known polarization and; (2) for the (d,α) reaction two separate correlations can be measured for each transition thereby increasing the likelihood of making a unique spin assignment. A bonus in using the (d,α) reaction for the angular correlation measurements is that spin-parity assignments are available, a priori, from tensor analyzing power measurements, T_{20} , at zero degrees. These measurements then decrease by half the range of spin-parity values for which the correlation data must be fit. These two methods combined could prove a potentially powerful tool for making spin and parity assignments in odd-odd nuclei.

With the acquisition of highly enriched targets of the isotope ^{36}S , a study of the odd-odd nucleus ^{34}P was undertaken using the techniques described above. Very little was known about the nucleus since its location in the neutron rich part of the table of isotopes made it inaccessible via most particle transfer reactions.

The organization of the thesis is outlined below. Chapter one comprises the theoretical expressions which form the basis for the experimental techniques used in this work; the well-known technique of spin-parity assignments using T_{20} measurements at 0° is reviewed briefly while method II angular correlation using a polarized beam is discussed more extensively. The last section of the chapter deals with the

corrections introduced to take account of the inevitable deviation of the experimental set-up from ideal alignment conditions. A survey of the nucleus ^{34}P is presented in chapter two followed by the results of the scattering experiment to measure the energy levels. The beginning of chapter three consists of a brief description of the polarized ion source which was an essential part of most of the experiments performed in this study. The tensor analyzing power measurements at 0° are presented in the remainder of the chapter. Details of the method II angular correlation experiment, analysis of the data and the resulting spin and parity assignments are presented in chapter four. Chapter five discusses the shell model calculations performed for both positive and negative parity states in order to compare with our experimentally measured spins and parities. This is followed by a summary of the results and conclusions. For the sake of completeness, an explicit derivation of the angular correlation function, discussed briefly in chapter one, is included as an appendix.

CHAPTER 1

THEORETICAL BASIS FOR EXPERIMENTAL METHODS

The first section of this chapter consists of definitions for quantities used in polarization and angular correlation theory. These are used in the next section to briefly present the arguments behind the spin-parity selection rules of the (d, α) reaction at 0° . The last section deals with angular correlations. The expression for the correlation function for a particle reaction followed by the emission of a single gamma-ray is presented. The expression for method II angular correlations is discussed as an extension of the simple correlation. Finally a method is presented for estimating the effects on the angular correlation of less than completely polarized beam and detection of the outgoing particles off the beam axis.

1.1 PRELIMINARY DEFINITIONS

1.1.1 The Density Matrix and Statistical Tensors

When considering an ensemble of particles it is

useful to introduce the density matrix as the wavefunction of the ensemble. The wavefunction of one of the particles in the ensemble, $|\psi\rangle$, can be written as a linear combination of the basis states $|x_\mu\rangle$,

$$|\psi\rangle = \sum_{\mu} a_{\mu} |x_{\mu}\rangle .$$

Since we're concerned with polarization the basis states chosen are the eigenfunctions of the z-axis projection of the orbital angular momentum. The density matrix is defined by,

$$\rho_{\mu\nu}^S \equiv \langle a_{\mu} a_{\nu}^* \rangle_{ave} \equiv \langle x_{\nu} | \rho | x_{\mu} \rangle \quad (1.1)$$

where the product of the amplitudes a_{μ} is averaged over all the particles in the ensemble. This definition is useful since the expectation value of any operator A over the ensemble is simply the trace of its product with the density matrix;

$$\begin{aligned} \langle A \rangle_{ens} &= \left[\sum_{\mu\nu} \langle \psi | \mu \rangle \langle \mu | A | \nu \rangle \langle \nu | \psi \rangle \right]_{ave} \\ &= \sum_{\mu\nu} \langle \mu | A | \nu \rangle \rho_{\mu\nu} \end{aligned}$$

The statistical tensors, t_{kq} , can be used, also, to describe the ensemble and these are related to the density matrix for spin s particles by,

$$\begin{aligned}
 t_{kq} &= \hat{s} \sum_{\mu\nu} (-)^{s-\nu} \langle s\mu, s\nu | kq \rangle \rho_{\mu\nu} \\
 &\equiv \text{Tr}(\tau_{kq}^S \rho) \quad , \quad (1.2)
 \end{aligned}$$

where $\hat{s} = \sqrt{2s+1}$ and $-k \leq q \leq k$.

Although physical observables are more easily expressed in the density matrix formalism, statistical tensors are used since they transform more simply under a rotation of the coordinate system. Adhering to the Madison convention, adopted for polarization work (BH70), the coordinate system is defined with the z-axis along the direction of motion of the particle and the y-axis normal to the reaction plane.

Some important properties in each formalism are listed below;

1) for an unpolarized ensemble of particles,

$$\rho_{\mu\nu} = (2s+1)^{-1} \delta_{\mu\nu} \quad \text{or} \quad t_{kq} = 0 \quad \text{for } k \neq 0 \quad (1.3)$$

2) for an ensemble aligned along the z-axis,

$$\rho_{\mu\nu} = \rho_{-\mu-\nu} = \rho_{\mu} \delta_{\mu\nu} \quad \text{or} \quad t_{kq} = 0 \quad \text{for } k \text{ odd and } q \neq 0 \quad (1.4)$$

3) for an ensemble polarized along the z-axis,

$$\rho_{\mu\nu} = \rho_{\mu} \delta_{\mu\nu} \quad \text{or} \quad t_{kq} = 0 \quad \text{for } q \neq 0 \quad (1.5)$$

1.1.2 Analyzing Powers and Cross-Section

Using the density matrix formalism quantum mechanics tells us that for an operator, T , effecting a transition from a state A to B , the density matrix of the final state is related to that of the initial state by,

$$\langle m | \rho_B^{\text{out}} | n \rangle = \sum_{\mu\nu} \langle m | T | \mu \rangle \langle \mu | \rho_A^{\text{in}} | \nu \rangle \langle n | T | \nu \rangle^*$$

$$\text{or, } \rho_{mn}^{\text{out}} = \sum_{\mu\nu} F_m^\mu \rho_{\mu\nu}^{\text{in}} F_n^{\nu*} \quad (1.6)$$

The quantities F_m^μ are the reaction amplitudes where only the dependence on the spin quantum numbers is shown here. The scattering cross-section for an incident polarized beam where the outgoing polarization is not measured is,

$$\left(\frac{d\sigma}{d\Omega}\right)_{\text{pol}} = \left(\frac{d\sigma}{d\Omega}\right)_o (2s+1) \text{Tr}(\rho \epsilon^*) \quad (1.7)$$

where ϵ is the efficiency matrix normalized to unit trace and depends on the detector position and geometry. The subscript 'o' refers to the differential cross-section for unpolarized beam.

The analogous expression using statistical tensors is,

$$\left(\frac{d\sigma}{d\Omega}\right)_{\text{pol}} = \left(\frac{d\sigma}{d\Omega}\right)_o \sum_{kq} T_{kq}^* t_{kq}^{\text{in}} \quad (1.8)$$

The tensors T_{kq} are the analyzing powers of the scattering reaction and are related to the reaction amplitudes in (6)

by,

$$T_{kq} = \left(\frac{d\sigma}{d\Omega} \right)_0^{-1} \sum_{\mu\nu m} (\tau_{kq}^{S=1}) F_m^\mu F_m^{\nu*} . \quad (1.9)$$

The τ_{kq} are the tensor operators which transform the density matrix to the statistical tensors, see equation (2). These are tabulated for up to spin two particles in Simonius' paper on polarization (Si74).

1.2 T₂₀ FOR THE (\vec{d}, α) REACTION AT 0°

1.2.1 Introduction

The (\vec{d}, α) reaction at 0° on an even-even target nucleus has been well established as a model-independent technique for making spin-parity assignments. The arguments behind the basis for the technique, lucidly presented in D. Petty's thesis (Pe76), are briefly recapitulated here. Because the target and outgoing alpha particle have zero spin, the Clebsch-Gordan coefficients for the angular momentum coupling simplify considerably and the reaction amplitudes for populating a state with J^π in the residual nucleus contain terms of the form,

$$(l_1 \lambda_1 s_1 \sigma_1 | \vec{J} \vec{m}) (l_2 \lambda_2 J m | \vec{J} \vec{m}) ,$$

where l_i and λ_i are the orbital angular momentum and its

projection on the beam axis for the entrance ($i=1$) and exit ($i=2$) channels, and s_1 and σ_1 are the spin and magnetic quantum numbers of the deuteron. With the incoming and outgoing particles along the beam axis, $\lambda_1 = \lambda_2 = 0$ which implies, $m = \sigma_1 = m$. That is, the magnetic substate populated in the residual nucleus is determined by the beam polarization.

For $m=0$ polarized deuterons, the above product can be written as,

$$(l_1 \ 0 \ 1 \ 0 \ | \ \bar{J} \ 0)(l_2 \ 0 \ J \ 0 \ | \ \bar{J} \ 0)$$

which is non-zero for $l_1 + 1 + \bar{J}$ and $l_2 + J + \bar{J}$ even only. Conservation of parity implies $\pi = (-)^{l_1 - l_2}$ for the parity of the residual nucleus. Together these conditions lead to the selection rule that natural parity states, $\pi = (-)^J$, have a zero cross-section with $m=0$ polarized beam. These arguments depend solely on established principles of conservation of angular momentum and parity and therefore yield a model-independent method for making spin-parity assignments.

The following section presents these arguments using formal expressions for the reaction amplitudes. The tensor analyzing power T_{20} is introduced as a useful quantity for expressing the reaction yields for $m=0$ and $m=1$ polarized beam. Lastly, two important points are dealt with: (1) the level of certainty with which a natural parity can be assigned to a level whose $m=0$ yield is zero within

experimental uncertainty, as a function of the number of bombarding energy measurements and; (2) the effect of detecting the alpha particles away from 0° .

1.2.2 Analyzing Power for (\bar{d}, α) at 0°

For an axially polarized beam with the polarization axis along the beam axis and the outgoing particles detected at 0° , equation (8) for the cross-section reduces to

$$\left(\frac{d\sigma}{d\Omega}\right)_{\text{pol}} = \left(\frac{d\sigma}{d\Omega}\right)_0 (1 + \hat{t}_{20} T_{20})$$

where \hat{t}_{20} refers to the tensor polarization of the beam. The statistical tensors \hat{t}_{kq} as a function of fractional beam polarization, P , for spin one particles are tabulated in Table 1.1. Using these values one can show that the tensor analyzing power T_{20} becomes,

$$T_{20} = \frac{\sqrt{2}}{P} \left(\frac{\sigma_{1-\sigma_0}}{2\sigma_{1+\sigma_0}} \right) \quad (1.10).$$

where σ_m denotes the yield with $m=0$ or 1 polarized beam. Therefore, at 0° , T_{20} is essentially a measure of the difference in the reaction yield using $m=0$ and $m=1$ deuterons.

Using (9) T_{20} can be written in terms of the reaction amplitudes. With conservation of angular momentum, at 0° many of the reaction amplitudes vanish,

$$F_m^\mu = 0 \quad \text{for } m \neq \mu \quad (1.11)$$

and the analyzing power becomes,

$$T_{20}(0^\circ) = \left(\frac{1}{\sqrt{2}}\right) \cdot \frac{|F_{-1}^{-1}|^2 - 2|F_0^0|^2 + |F_1^1|^2}{|F_{-1}^{-1}|^2 + |F_0^0|^2 + |F_1^1|^2} \quad (1.12)$$

The condition imposed by parity conservation on the reaction amplitudes for populating a state J^π of definite spin and parity is,

$$F_{-m}^{-\mu} = \pi (-)^{\mu+m+1+J} F_m^\mu \quad (1.13)$$

and leads to the following model-independent selection rules for the (d, α) reaction on an even-even nucleus:

(1) for a state $J^\pi = 0^+$, $\left(\frac{d\sigma}{d\Omega}\right)_0 = 0$.

(2) for a state $J^\pi = 0^-$,

$$T_{20} = -1/2.$$

(3) for natural parity states, $\pi = (-)^J$,

$$T_{20} = 1/2.$$

(4) for unnatural parity states, $\pi = (-)^{J+1}$,

$$-1/2 < T_{20} < 1/2.$$

In order to ascertain within a prescribed level of confidence that a value of T_{20} at the extremums $1/2$ or $-1/2$ does not correspond to an unnatural parity state, one can

evaluate the probability distribution for measuring T_{20} across the whole range of values. This question was addressed by D. Petty (Pe76). He assumed a statistical model for the nuclear reaction where the scattering amplitudes, averaged over energy, are described by a constant direct term plus a fluctuating compound term. The effect of these random fluctuations over bombarding energy is to give rise to a probability distribution for T_{20} which is symmetric about $T_{20}=1/2(1/\sqrt{2})$. The width of the distribution decreases with increasing number of measurements at different bombarding energies. Table 1.2, reproduced from his thesis, shows the probability, for unnatural parity state, of obtaining an average value of T_{20} within a deviation, Δ , from either extremum ($T_{20}=1/\sqrt{2}$ or $T_{20}=-\sqrt{2}$) as a function of the number of measurements at different bombarding energies, N . Therefore with measurements at three energies, made with an accuracy $\Delta < .10$, the spin-parity is determined with a 99.9% level of confidence.

The other point which needs to be addressed is the effect of measuring T_{20} away from 0° . The condition on the reaction amplitudes in (11) must now be relaxed and the expression for T_{20} from (9) will now include terms with $\mu \neq m$. The calculations performed by Petty using a compound statistical model to describe the reaction mechanism showed an increasing attenuation of T_{20} with increasing detection angle. The magnitude of the attenuation depended on the center of

Table 1.1 Vector and tensor polarizations for $s=1$ particles as a function of the fractional beam polarization, $P = 1-1/Q$, where Q is the quench ratio (see sect. 3.1)

	$m=1$	$m=0$	$m=-1$
t_{10}	$\sqrt{3/2} P$	0	$-\sqrt{3/2} P$
t_{20}	$1/\sqrt{2} P$	$-\sqrt{2} P$	$1/\sqrt{2} P$

Table 1.2 Cumulative probability of an unnatural parity state for various deviations, Δ , from the limits of T_{20} ($-\sqrt{2}$ or $1/\sqrt{2}$)^{b)}

Number of Energies N	Cumulative Probability ^{a)}			
	$\Delta=.05$	$\Delta=0.1$	$\Delta=0.2$	$\Delta=0.4$
1	2.5%	4.5%	9.5%	19%
2	0.1%	0.7%	2.7%	9.5%
3		0.1%	0.8%	5.4%
4			0.2%	3.0%
5			0.1%	1.6%
10				0.1%

a) Values not shown are less than 0.1%

b) Reproduced from (Pe76)

mass momentum in the entrance channel. For 10 MeV deuterons incident on a ^{36}S target, and the outgoing alphas detected at $\theta_{\text{lab}}=4^\circ$, T_{20} would be attenuated by about five percent.

1.3 ANGULAR CORRELATION THEORY

A complete treatment of the theory of angular correlations is available in the literature, (Fe65) and (RB67), and in the first part of this section the expression for a simple γ -ray correlation from a particle induced reaction is simply stated. The reader is referred to the appendix for a complete derivation of this expression. The notation of Rose and Brink (RB67) is employed since it is widely accepted in the field and the correlation data were analyzed using their formalism. Extrapolating from the simple γ -ray transition the expression for Litherland and Ferguson method II angular correlations (LF61) is presented in the second part. Starting with this expression the advantages in using a polarized beam for method II correlation measurements are highlighted. The power of this technique is illustrated by comparing the restrictions on spin assignments possible for correlation measurements with one and two beam polarizations. In the last section, the effects of a not completely polarized beam and detection of the outgoing particles slightly off axis are discussed and

their magnitudes are estimated.

1.3.1 The Simple γ -Ray Correlation

The simplest γ -ray correlation occurs when the angular distribution of the γ -ray decay of the residual nucleus populated in a nuclear reaction is measured relative to the beam direction (z-axis). This simple case is depicted in Figure 1.1.

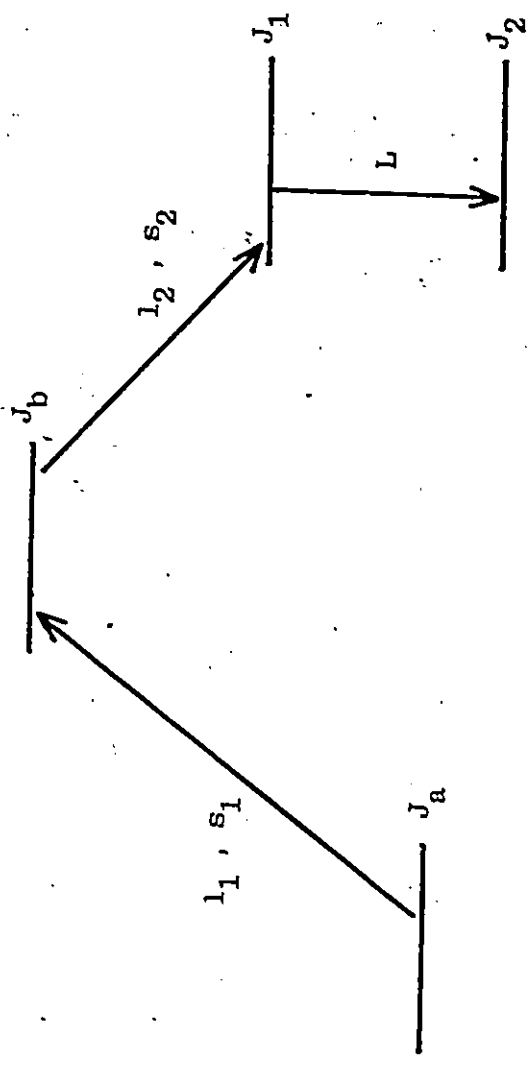
In an analogous manner to the expression in equation (7) for the cross-section, the angular distribution yield is expressed as a product of the statistical tensor of the reaction products, ρ_{kq} , and the efficiency tensor, ϵ_{kq}^* , for detecting these products. By using the properties of statistical tensors for coupled angular momenta and evaluating the efficiency tensor of the γ -ray detector, which contains the explicit angular dependence, one obtains the following expression for the correlation function,

$$W(\theta) = W_0 \sum_{k \text{ even}} B_k(J_1) R_k(LLJ_1J_2) Q_k P_k(\cos\theta). \quad (1.14)$$

The normalization W_0 is chosen such that the $k=0$ coefficient of $P_k(\cos\theta)$ in the sum is unity. The derivation of (14) assumed that the emitted particles from the nuclear reaction with unpolarized beam were undetected and that the state in the residual nucleus had definite parity. These two conditions lead to alignment of the residual nucleus and

Figure 1.1

Diagram showing the spin and angular momentum notation for a pure multipole gamma-ray decay following a nuclear reaction.



2

thus to the contribution of only even k terms in the sum. The coefficients $B_k(J_1)$, $k=2,4,\dots,2J_1$, are defined in terms of the statistical tensors and, for an aligned state are simply linear combinations of the population parameters. Generally, these coefficients are unknown parameters which must be varied when fitting the measured correlation. The R_k coefficients contain the angular momentum coupling algebra and are tabulated in (RB67) for different L , J_1 , and J_2 values. The attenuation coefficients Q_k describe the attenuation of the measured correlation due to the finite detector solid angle and depend on the particular gamma-ray detector geometry.

Measured correlations can be fit with this expression in an attempt to determine the initial spin J_1 . The solution may not be unique since the B_k 's or the population parameters, $P(m)$, are variable.

1.3.2 Method II Angular Correlations

The technique of Litherland and Ferguson (LF61) method II angular correlations limits the number of unknowns in the correlation function by detecting the emitted γ -ray in coincidence with the outgoing particle along the beam direction. With an unpolarized beam and by detecting the particles in an annular detector the cylindrical symmetry of the problem is preserved. Therefore the correlation

function derived in the previous section remains valid. The result of this highly aligned geometry is that the orbital angular momentum of the outgoing particle has zero projection on the quantization axis. Thus, by conservation of angular momentum, population is limited to those substates in J_1 with

$$|m| < J_a + s_1 + s_2 \quad (1.15)$$

where s_1 and s_2 denote the spins of the incident and emitted particles respectively, see Figure 1.1. Consequently the most advantageous reactions involve low spin projectile and ejectile particles on an even-even target nucleus. In particular, for the (d, α) reaction the constraint on the substates populated is $|m| < 1$. Using, also, the restriction on the density matrix for an aligned ensemble, equation (4), only one parameter is necessary to specify the orientation of the state J_1 ; that is

$$\alpha \equiv \frac{P(m=\pm 1)}{P(m=0)}$$

Another unknown often present in γ -ray correlations; which has so far been excluded from our discussion since pure multipole radiation was assumed, is the multipole mixing ratio, δ . The amplitudes of two competing multipolarities L and $L'=L+1$ will add coherently and one can show that the correlation function becomes,

$$W(\theta) = W_0 \sum_{k \text{ even}} B_k(J_1) R_k(J_1 J_2) Q_k P_k(\cos\theta) \quad (1.16)$$

$$\text{where } R_k(J_1 J_2) \equiv \{ R_k(LLJ_1 J_2) + 2\delta R_k(LL'J_1 J_2) + \delta^2 R_k(L'L'J_1 J_2) \} (1+\delta^2)^{-1}$$

$$\text{and } \delta \equiv \frac{\langle J_1 | L' | J_2 \rangle / (2L'+1)^{1/2}}{\langle J_1 | L | J_2 \rangle / (2L+1)^{1/2}}$$

This definition of the mixing ratio and the matrix elements are those of Rose and Brink which are derived in a phase consistent manner from the electromagnetic operators. The mixing ratio contains the nuclear structure information and is an additional parameter in fitting the measured correlation. Therefore, in general a (d,α) method II angular correlation would have three unknowns, α, J₁, and δ. Unique identification of the spin J₁ within this parameter space, although more probable than for a singles angular distribution measurement, is still not attainable for many measured correlations. A study of the systematics of making spin assignments from measured method II angular correlations was done by P. Twin (Tw73).

In light of the above arguments, the advantages of using a polarized beam in method II angular correlations become evident. Assuming a completely polarized beam, by conservation of angular momentum the only substate of the residual nucleus level J₁ populated is the same as that of

the beam ¹⁾. The previously unknown quantity α is eliminated and only two unknowns remain. Furthermore, since two separate correlations can be measured, one with $m=0$ and one with $m=1$ polarized beam, for every transition $J_1 \rightarrow J_2$, there is twice the experimental data and one less parameter with which to arrive at possible spin assignments for the initial state.

The advantages of using a polarized beam for method II angular correlations was investigated by G. Jones et al. (JG75) at McMaster. Their study consisted of an extensive computer search to identify the values of spin and mixing ratio for which inherent ambiguities in the correlation function could be removed by using both $m=0$ and $m=1$ correlation data. The correlation for a transition $J_1 \rightarrow J_2$ with mixing ratio δ_{12} can be described by the Legendre polynomial coefficients $a_k^{J_1 J_2 m}(\delta_{12})$, where m denotes the beam polarization and $k=0, 2, 4$, since only dipole and

1) With the beam polarization axis along the beam direction which is also the quantization axis, the state in the residual nucleus will have cylindrical symmetry. However, since only one substate is populated the alignment condition, $P(m)=P(-m)$, which led to the restriction of even k in equation (14) is no longer valid. It can be shown, however that the restriction of even k holds for a correlation satisfying the following properties: (1) the initial and final states, J_1 and J_2 , have definite parity and; (2) the correlation measurements have reflection symmetry in the reaction plane (i.e. the circular polarization of the γ -ray is not measured). Both requirements are satisfied in method II angular correlation measurements with polarized beam, and the expression in (14) remains an accurate description of the correlation function.

quadrupole radiation were considered. The regions of ambiguity were determined by comparing the Legendre coefficients for this transition with those for transitions from all other possible initial spin values, $J_2 - 2 < J_i < J_2 + 2$, and over the whole range of mixing ratio values, δ_{i2} .

The quantity Q^2 used to obtain a measure of the difference between the correlations was calculated by taking the square of the difference in the Legendre coefficients,

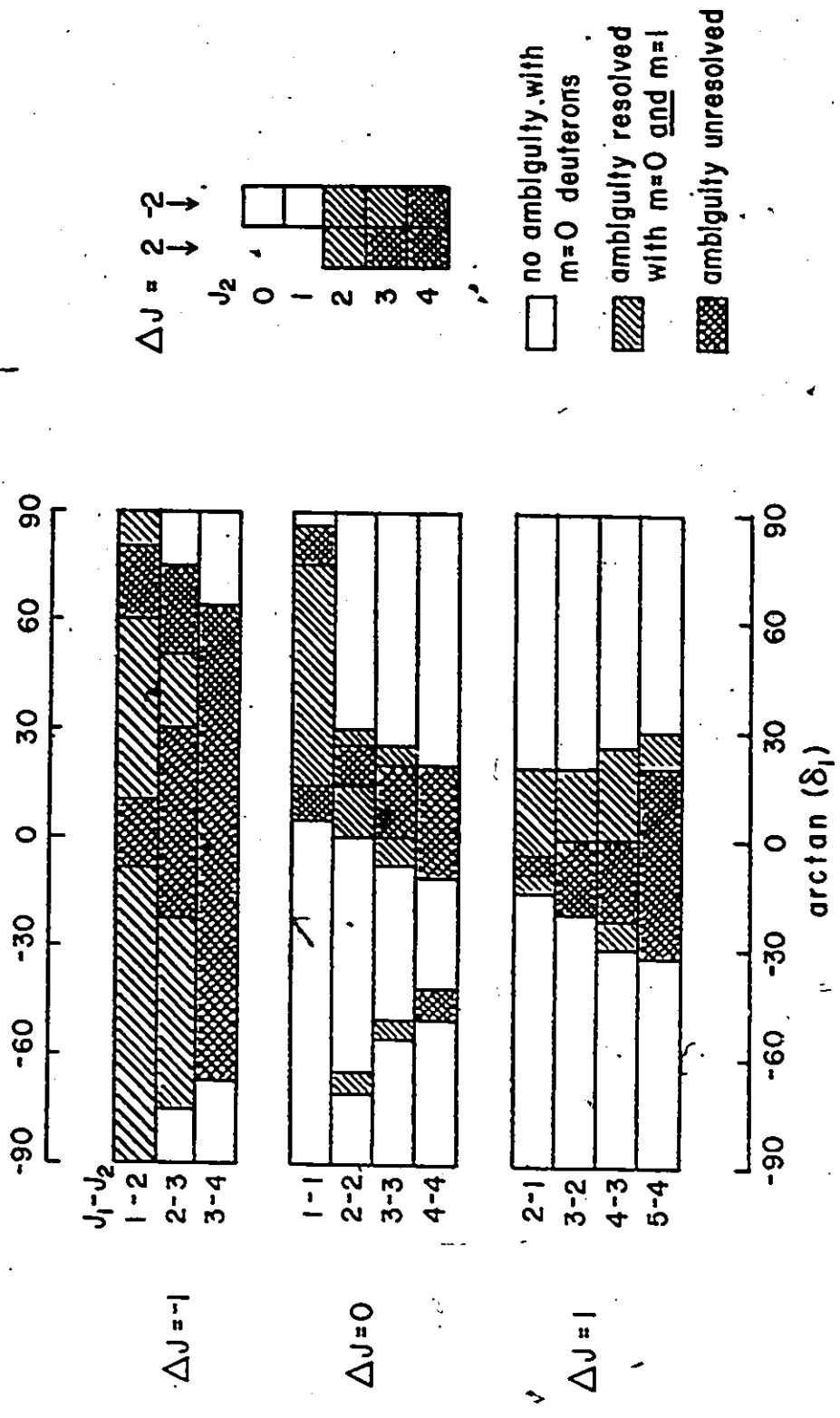
$$Q_m^2(\delta_{12}, \delta_{i2}) = \sum_{k=2,4} [a_k^{J_1 J_2}(\delta_{12}) - a_k^{J_1 J_2}(\delta_{i2})]^2,$$

where the subscript m has been suppressed from the Legendre coefficients. Contour plots of Q^2 as a function of δ_{12} and δ_{i2} were plotted for both $m=0$ and $m=1$ deuterons. The value of Q^2 corresponding to the 99.9% confidence level used to reject spin hypotheses in experimental correlation data will depend on the uncertainties in the data and the shape of the correlation function. The average value obtained for angular correlations with five data points and 1000 counts at the peak angle was 120×10^{-4} . A value of Q^2 below this level indicated unresolvable correlations thereby giving rise to an ambiguity for the transition $J_1 \rightarrow J_2$ at the particular value of the mixing ratio δ_{12} .

The results of this study have been summarized in Figure 1.2 for all possible $J_1 \rightarrow J_2$ transitions with $J_2 < 4$. The large regions with unidirectional hatching indicate the

Figure 1.2

Chart illustrating the regions of mixing ratio δ_1 , for transitions $J_1 \rightarrow J_2$, where ambiguities in spin assignments occur for method II (\vec{d}, α) angular correlations with different beam polarizations substates.



advantage of having both correlations since these correspond to values of δ_{12} for which an ambiguity existed with just the $m=0$ correlation but was resolved with the inclusion of the $m=1$ correlation. The regions with cross hatching correspond to mixing ratio values δ_{12} for which the ambiguity is unresolved even when both correlations are considered. It is worth noting that the regions over which ambiguities are resolved is larger for transitions where the initial spin is small. This is not unexpected since the $m=0$ and $m=1$ correlations will be most different for low spin values and will tend toward a similar shape for large spin values.

1.3.3 Method II Correlations With an Unobserved γ -Ray Transition

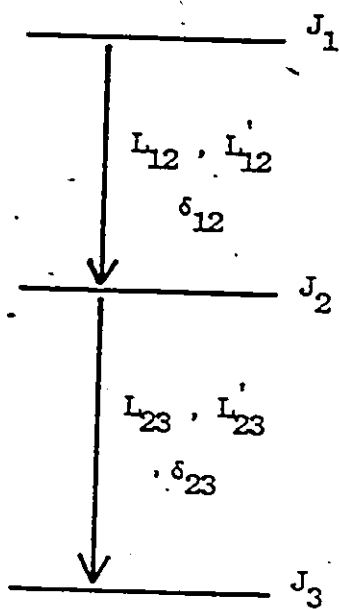
In the previous section the discussion of method II angular correlations was restricted to the particular case of a γ -ray emitted from the level in the residual nucleus populated by the outgoing coincident particle. In a particle-gamma coincidence experiment one can also measure the correlation for any γ -rays in a cascade originating from the decay of this initial state. This situation is depicted in Figure 1.3 for a two γ -ray cascade. L_{23} and L'_{23} are the multipolarities of the observed gamma ray and L_{12} , L'_{12} are those for the unobserved one.

Figure 1.3

Spin, multipolarity and mixing ratio notation for
a two gamma-ray cascade.

12

125



The angular correlation function for the L_{23} , L'_{23} γ -ray can be derived in a similar manner to that already shown for the single γ -ray transition. Using the notation of Rose and Brink introduced earlier, the correlation function has the following form;

$$W(\theta) = W_0 \sum_{k \text{ even}} B_k(J_1) U_k(J_1 J_2) R_k(J_2 J_3) Q_k P_k(\cos\theta) \quad (1.17)$$

Comparison with the expression for the correlation function in (16) leads to the interpretation of the product $B_k U_k$ as describing the orientation of the state J_2 . Therefore the coefficient $U_k(J_1 J_2)$ transforms the orientation of the initial state J_1 to that of the intermediate state J_2 via the unobserved transition L_{12} , L'_{12} ; it is defined by,

$$U_k(J_1 J_2) = \{ U_k(L_{12} J_1 J_2) + (\delta_{12})^2 U_k(L'_{12} J_1 J_2) \} [1 + (\delta_{12})^2]^{-1},$$

$$\text{where } U_k(L_{12} J_1 J_2) = (-)^k \frac{W(J_1 J_2 J_1 J_2; L_{12}^k)}{W(J_1 J_2 J_1 J_2; L_{12}^0)}$$

The W 's are Racah coefficients and δ_{12} is the mixing ratio for the unobserved transition. The U_k coefficients are tabulated in (RB67). Since the first γ -ray is not observed there is no term for the interference between the multipolarities L_{12} and L'_{12} . The additional information derived from the correlation of a subsequent cascade transition can be useful in making a unique spin assignment for J_1 or J_2 .

1.3.4 Effect of Polarization and Detector Solid Angle

In practice the constraints placed on the magnetic substate population in the discussion of method II ($\vec{d}, \alpha Y$) angular correlations of the last section, equation (15), must be relaxed. The reasons for this are two-fold. Firstly, the beam is not usually completely polarized and the unpolarized component will give rise to the population of other substates. The relative magnitude of the population of these other substates will depend on the beam polarization as well as the reaction amplitudes. Secondly, the effect of detecting the outgoing particles in an annular detector around 180° will result in a non-zero projection of the orbital angular momentum on the quantization axis. Depending on the value of the angular momentum populating the excited state, substates other than the beam substate can be populated.

We first examine the effect of less than completely polarized beam. As previously discussed (see equation 6) the expression for the density matrix of the outgoing residual nucleus is,

$$\rho_{mn}^{\text{out}} = \sum_{\mu\nu} F_m^\mu \rho_{\mu\nu}^{\text{in}} F_n^{\nu*} \quad (1.18)$$

As shown in (4), for an aligned ensemble this expression simplifies considerably when the beam polarization axis is along the beam direction and the outgoing particles are

detected along the beam direction in a detector with cylindrical symmetry. Thus, we write

$$\rho_m^{\text{out}} = \sum_{\mu} |F_m^{\mu}|^2 \rho_{\mu}^{\text{in}}$$

The cross-section for detecting the outgoing particles, assuming a point detector, is proportional to the trace of the outgoing density matrix (see equation 7),

$$\begin{aligned} \sigma_{\text{pol}}(\theta) &= \sigma_0 \text{Tr}(\rho^{\text{out}}) \\ &= \sigma_0 \sum_{\mu m} |F_m^{\mu}|^2 \rho_{\mu}^{\text{in}} \end{aligned}$$

Using the property of the reaction amplitudes at 0° , equation (11), and the property for a transition between states of good parity, equation (13), allows the expression for the cross section to be written as,

$$\sigma_{\text{pol}}(\theta) = \sigma_0 [\rho_0^{\text{in}} \beta_0^0 + (\rho_1^{\text{in}} + \rho_{-1}^{\text{in}}) \beta_1^1] \quad (1.19)$$

where the notation, $\beta_j^i \equiv |F_j^i|^2$, is introduced for simplicity. The first product in the bracket contributes to the population of the $m=0$ substate in the residual nucleus while the latter two products denote the population of the $m=1$ and -1 substates, respectively. Thus, for a beam of $m_d=0$ polarized deuterons the ratio of the population parameters is,

$$\alpha_{pol}^0 \equiv \frac{P(m=\pm 1)}{P(m=0)} = \frac{\rho_{\pm 1} \beta_1^1}{\rho_0 \beta_0^0} \quad (1.20)$$

where the superscript '0' on α signifies $m_d=0$ deuterons. The superscript 'in' on ρ has been dropped for brevity and from this point on ρ will always refer to the beam. A similar expression can be written for the substate population ratio $P(m=0)/P(m=1)$ for an $m_d=1$ polarized deuteron beam. The unknown quantity necessary for evaluating the population parameters is the ratio of the reaction amplitudes β_1^1/β_0^0 . A value for this ratio can be obtained from the measured ratio, R , of the cross-section for $m=0$ and $m=1$ deuterons. Using (19) one obtains,

$$R \equiv \frac{\sigma_0}{\sigma_1} = \frac{\rho_0(m_d=0)\beta_0^0 + [\rho_1(m_d=0) + \rho_{-1}(m_d=0)]\beta_1^1}{\rho_0(m_d=1)\beta_0^0 + [\rho_1(m_d=1) + \rho_{-1}(m_d=1)]\beta_1^1} \quad (1.21)$$

The subscripts '0' and '1' on σ replace the 'pol' in (19) and denote the reaction yield with $m_d=0$ or 1 respectively. Assuming the unpolarized component of the beam is composed of equal amounts of the three substates then, for a known beam polarization and with the alignment condition (4), all the density matrix parameters for the beam are known. Therefore by measuring R with a beam of known polarization, the ratio β_1^1/β_0^0 is determined and the population parameters for the angular correlation are uniquely determined.

The above calculation did not include any effect

from detecting the outgoing particles at a finite angle off the quantization axis. In their original paper on method II angular correlations (LF61), Litherland and Ferguson investigated the effect of a finite solid angle detector by expressing the population parameters, or the statistical tensors $B_k(J_1)$ in (16), in terms of the appropriate statistical tensors for the different reaction components and the efficiency tensor for the annular particle detector. By expanding the efficiency tensor in the limit of small angles they obtained a correction to the population parameter of the substates $m_d \pm |\lambda|$, where λ is an integer, proportional to,

$$\frac{P(m_d \pm |\lambda|)}{P(m_d)} = \xi^{2|\lambda|} \quad (1.22)$$

ξ is the maximum half-angle, in radians, subtended by the particle detector.

In order to estimate the combined effect of the beam polarization and the finite detector solid angle on the population parameters we expand the expression for the cross-section in (18) without the restriction of $\theta=0^\circ$ on the reaction amplitudes. The result is,

$$\sigma_{\text{pol}} = \sigma_0 \left\{ [\rho_0 \beta_0^0 + (\rho_1 + \rho_{-1}) \beta_0^1] + [\rho_1 \beta_1^1 + \rho_0 \beta_1^0 + \rho_{-1} \beta_1^{-1}] + [\rho_{-1} \beta_1^1 + \rho_0 \beta_1^0 + \rho_1 \beta_1^{-1}] \right\} \quad (1.23)$$

where the property of the reaction amplitudes for states of definite parity has been used and substates with $|m| > 2$ have been neglected for simplicity. Using the [] brackets, the terms have been grouped according to the substate populated in the residual nucleus; the order is $m=0, 1,$ and -1 . In the limit of small detector angles the reaction amplitude term β_1^{-1} will be small compared to β_1^1 and β_1^0 and the ratio for the population parameters of a state populated with an $m_d=0$ beam will be,

$$\frac{P(m=1)}{P(m=0)} = \frac{\rho_1 \beta_1^1}{\rho_0 \beta_0^0 + (\rho_1 + \rho_{-1}) \beta_0^1} + \frac{\rho_0 \beta_1^0}{\rho_0 \beta_0^0 + (\rho_1 + \rho_{-1}) \beta_0^1} \quad (1.24)$$

$$\equiv \alpha_{\text{pol}}^0 + \alpha_{\text{f.a.}}^0 \quad (1.25)$$

A similar expression holds for the ratio $P(m=-1)/P(m=0)$.

The population parameters for the correlation with $m_d=1$ deuterons can be expressed in the same manner,

$$\frac{P(m=0)}{P(m=1)} = \frac{\rho_0 \beta_0^0}{\rho_0 \beta_1^0 + \rho_1 \beta_1^1} + \frac{(\rho_1 + \rho_{-1}) \beta_0^1}{\rho_0 \beta_1^0 + \rho_1 \beta_1^1} \quad (1.26)$$

$$\equiv \alpha_{\text{pol}}^1 + \alpha_{\text{f.a.}}^1 \quad (1.27)$$

Also, with $m_d=1$ deuterons there will be a small population of the $m=2$ substate from finite angle (f.a.) effects and of the $m=-1$ from the unpolarized component of the beam. For the analysis, the magnitude of $P(m=2)$ was taken as half

$P(m=0)$ since the $m=0$ substate has a contribution from both polarization and finite angle. These values were allowed to vary by 10% of the largest population parameter in arriving at the best fit to the data.

The approximation in equations (25) and (27) can be understood by comparing the expression for α_{pol}^0 with that of equation (20) where no finite angle effect was included. It is seen that the separation in (25) into a polarization and finite angle term is valid as long as $\rho_0\beta_0^0$ is the dominant term in the denominator of equation (24), and similarly for the term $\rho_1\beta_1^1$ in (26). These conditions are satisfied if the state in the residual nucleus has a non-vanishing cross-section for both $m_d=0$ and $m_d=1$ deuteron beam, that is $T_{20} \neq 1/\sqrt{2}$ or $-\sqrt{2}$. Therefore, for a natural parity state, where $\sigma_0=0$ at 0° , or a 0^- state, where $\sigma_1=0$ at 0° , the approximation made in such a separation is not valid. For these cases population of the predominant substate can be taken to be almost 100 percent.

The expressions for the population parameters, (24) and (26), contain the four unknown reaction amplitude terms β_0^0 , β_1^0 , β_0^1 , and β_1^1 . Since only the relative magnitude of these quantities is of interest, taking the ratio with respect to β_0^0 reduces the number of unknowns to three. To solve for these and thus determine the $P(m)$ parameters uniquely, one requires three equations. The first is obtained as before from the ratio of the cross-sections for

$m=0$ and $m=1$ deuterons. This time, however σ_{pol} is that of equation (23) with the β_1^{-1} terms neglected. The ratio is easily obtained from the measured particle yields and this results in an equation with the three unknowns. The other two equations are obtained from the expressions for $\alpha_{\text{f.a.}}^0$ and $\alpha_{\text{f.a.}}^1$ in (24) and (26), respectively. With the estimate for the finite angle effect determined by Litherland and Ferguson, (22), numerical values can be assigned to the $\alpha_{\text{f.a.}}$'s. Our detector maximum half-angle was $\xi=11^\circ$ or 0.2 radians, thus yielding a finite angle correction on the order of four percent. Because this value is an order of magnitude estimate the larger value 10% was used for the correction factors. With these three equations a solution to the three unknown ratios β_1^j/β_0^0 was determined and these values were substituted in equations (24) and (26) to obtain the population parameters.

In conclusion one finds that for a known beam polarization and with a measurement of the ratio of the cross-sections, a few simplifying assumptions allow one to determine the effect on the population parameters from the polarization and the detector solid angle. In particular the statistical tensors $B_k(J_1)$ in the correlation function of equation (16) can be completely determined once the population parameters are known. Thus the earlier statements on the advantages of using a polarized beam with method II still hold.

CHAPTER 2: THE NUCLEUS ^{34}P

The first section of this chapter consists of a brief survey of what was known about ^{34}P prior to undertaking this study. Before measuring tensor analyzing powers and angular correlations in ^{34}P , a (d, α) scattering experiment was carried out in an effort to identify states at higher excitation energy. A description of this experiment and the results obtained are presented in section two. A summary of these results and a discussion of angular distribution measurements are presented in the last section.

2.1 EXISTING MEASUREMENTS IN ^{34}P

The paucity of data for the nucleus ^{34}P is a direct consequence of its situation in the neutron-rich region, where it is accessible from very few stable isotopes via single or multi-particle transfer reactions. Goosman et al. (GD73) used the heavy-ion reaction $^{18}\text{O}(^{18}\text{O}, \text{pn})^{34}\text{P}$ to measure the half-life of ^{34}P ($t_{1/2} = 12.45 \pm 0.10$ sec) by detecting the β -particles in coincidence with known γ -rays in the ^{34}S

daughter. The allowed character of the β transition to states of spin 0^+ and 2^+ in ^{34}S , evidenced by the respective $\log(ft)$ values 5.16 ± 0.02 and 4.93 ± 0.07 , implied a spin of 1^+ for the ground state of ^{34}P .

Several experiments have been carried out recently in which the excitation energies for the level scheme of ^{34}P were determined. The results of these different experiments are summarized in Table-2.1. The first one by Ajzenberg-Selove et al. (AF77) used the charge exchange reaction ($t, ^3\text{He}$) on a target of ^{34}S enriched to 85.6%. Their values for the excitation energy are listed in the first column of the table. Based on these values for the lower excited state energies, Nathan and Alburger (NA77), again using the heavy ion reaction ^{18}O on ^{18}O and detecting β - γ coincidence events, were able to study the β -decay of ^{34}Si and also determine the excitation energy of the two lowest states in ^{34}P to a greater precision. Their calculated $\log(ft)$ values for the decay to the 0.429 MeV and 1.608 MeV levels were >5.2 and 3.35 ± 0.18 , respectively. The allowed character of the branch to the 1.608 MeV level strongly suggests a spin 1^+ since the only non- 1^+ level to which ^{34}Si ($J^\pi = 0^+$) could decay is the analog 0^+ , T=3 level which is predicted to be at around 9 MeV excitation energy.¹⁾ This assignment

1) Calculation of the excitation energy of the analog state included the quantum mechanical correction to the Coulomb energy shift.

Table 2.1 Excitation energies in ^{34}P .
Units are in MeV and the solid line denotes a level seen whose excitation energy was not measured.

$(t, ^3\text{He})^a$	$(\beta-\gamma)^b$	$(d, \alpha)^c$	$(^7\text{Li}, ^7\text{Be})^d$	present work
0.423(10)	0.4291(2)	0.429(7)	—	0.430(4)
1.605(10)	1.6076(5)	1.616(10)	—	—
2.225(10)		2.236(10)	—	2.232(10)
2.309(10)		2.302(20)	—	2.307(7)
		2.372(20)		
		2.628(12)		
				2.683(7)
				[3.086(15)] ^{e)}
		3.201(16)		
[3.345]				[3.291(23)]
				3.482(8)
				[3.546(12)]
				4.306(7)
			4.470(70)	4.438(13)
				4.744(9)
			7.440(70)	

a) from reference (AF77)

b) from reference (NA77)

c) from reference (BZ78)

d) from reference (DF85)

e) the square brackets indicate a tentative assignment

however is dependent on the assumption of a negligible ground state branch which could not be measured in the experiment. One can show that, although the ground state branch would have to be much larger than that to the 1.608 MeV level in order to increase the $\log(ft)$ value beyond the empirical range for an allowed transition, the possibility of this occurrence cannot be discounted and the assignment of 1^+ remains uncertain.

The other two experiments used the same highly enriched ^{36}S isotope which was used in our experiments. The natural abundance of ^{36}S is 0.014% and therefore is very costly to produce in high enrichments. Some of this highly enriched isotope became available recently as a result of a program by Russian scientists to study the feasibility of laser isotope separation (Ma82). The results obtained by Babenko et al. (BZ78) using the reaction $^{36}\text{S}(d, \alpha)^{34}\text{P}$ are included in the third column of Table 2.1. The fourth column comprises the results from the $^{34}\text{S}(^7\text{Li}, ^7\text{Be})^{34}\text{P}$ experiment performed by Drumm et al. (DF85) as part of a larger study of neutron-rich nuclei.

2.2 ENERGY LEVEL MEASUREMENTS

2.2.1 Experimental Set-Up

The measurement of excitation energies was carried

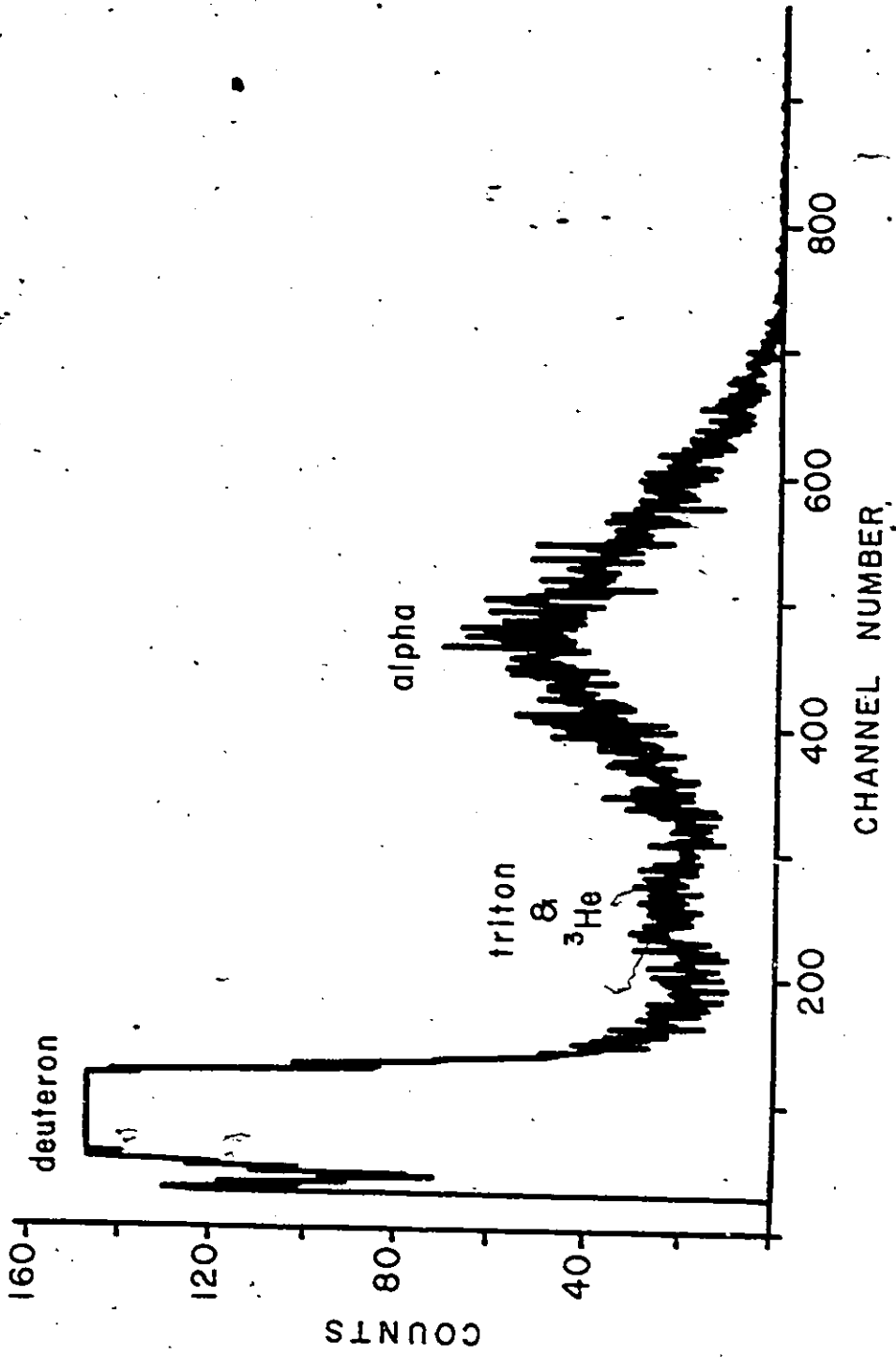
out using the reaction $^{36}\text{S}(d,\alpha)^{34}\text{P}$. The target enrichment was 81.1(0.2)% ^{36}S and 18.9(0.2)% ^{34}S . The target was prepared by S.Raman at Oak Ridge employing a technique developed by P.Maier-Komor (Ma82) in which a silver foil, in this case of 200 $\mu\text{g}/\text{cm}^2$ thickness, is completely sulfided, forming Ag_2S . Silver is used because of the high affinity of silver to sulfur, thereby ensuring efficient conversion of the isotope to target material. According to Raman et al. (RR84), who have used targets made from the same isotope material, the target also contains trace amounts of B, Na, Al, Si and K.

The outgoing alpha particles were momentum-analyzed with an Enge split-pole spectrograph and detected in a focal-plane position-sensitive delay-line detector. The detector was a gas-proportional counter divided into two sections; the front section containing the delay line and the back section consisting of a high-voltage anode wire (MR75). The position information was derived from the delay-line signals and the energy loss (ΔE) of the particle was obtained from the back-counter signal. A typical ΔE spectrum is shown in Figure 2.1 where the regions corresponding to different particles have been labelled. A two-dimensional plot of ΔE versus position yielded a clean separation of the tritons and ^3He particles from the alpha particles. The position spectra displayed in Figure 2.2 were obtained by setting a boundary around the alphas in the

Figure 2.1

ΔE spectrum for the reaction $^{36}\text{S}(d,\alpha)^{34}\text{P}$ at $\theta_{\text{lab}}=45^\circ$, measured with the delay line detector positioned at the focal plane of the Enge spectrograph.

ΔE SPECTRUM

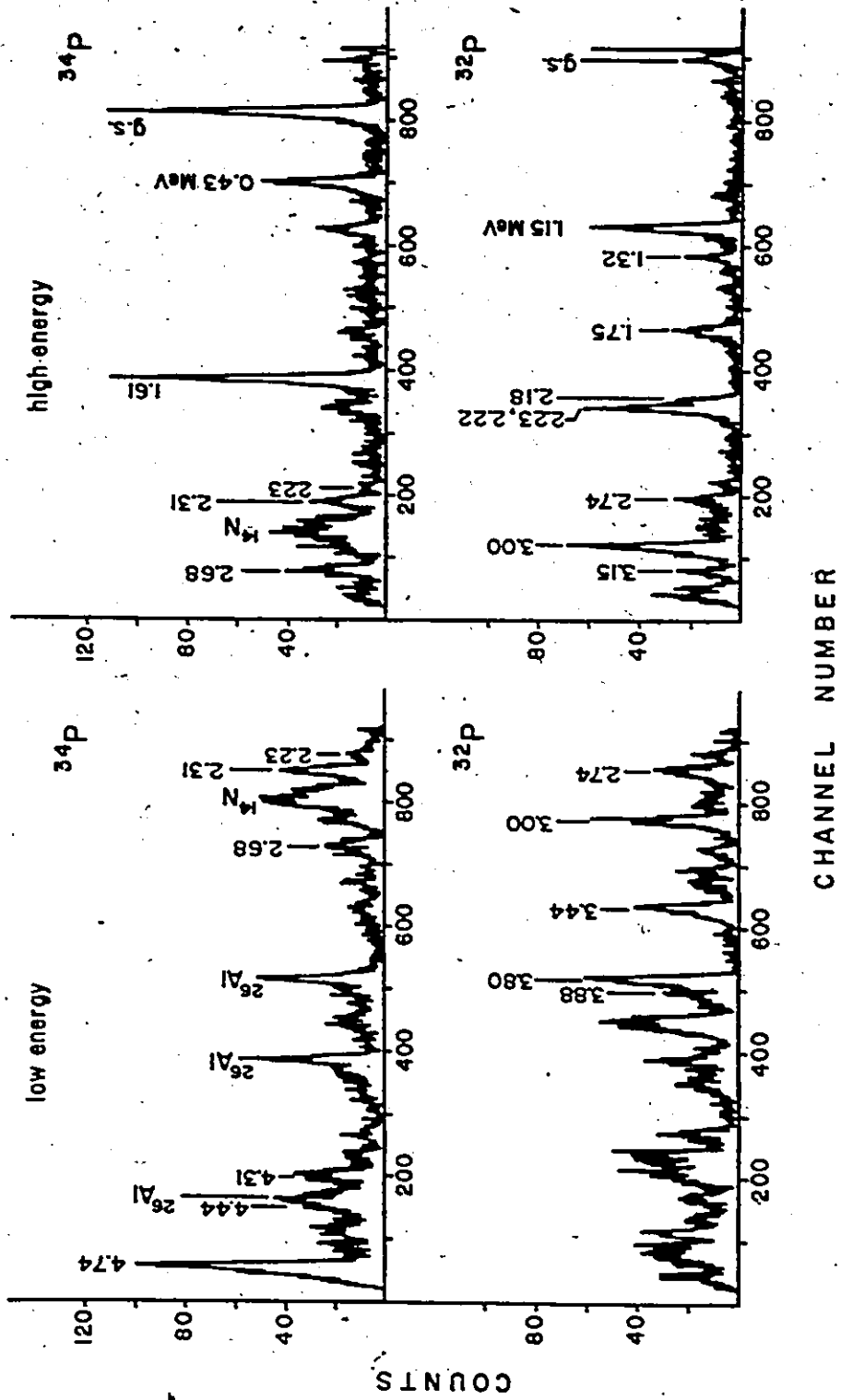


two-dimensional spectrum. The resolution of the alpha particle position spectrum was limited mostly by the target thickness.

The experiment was performed at three deuteron bombarding energies, 6, 10, and 16 MeV, to ensure that every level could be observed at least once. The spectra collected at 16 MeV had a large background continuum associated with alphas from the scattering of deuterons on silver. The Q-value for this reaction is much larger than that for the same reaction on sulfur. Therefore the energy range of detected alpha particles corresponds to the population of states at higher excitation energy in paladium than in phosphorus. Because the density of states in the heavier nucleus is quite large, even at 1 MeV, the spectrum of emitted alpha particles is essentially a continuum. This background is completely absent at 10 MeV bombarding energy because the emerging alpha particles are below the Coulomb barrier for paladium. At this lower energy spectra were collected at different angles to allow for proper identification of ^{34}P states which at some angles were hidden by contaminant states. At each angle spectra were collected in two bites to include states up to 5 MeV excitation. Owing to the large quantity of ^{34}S in the target, spectra were collected with a target of enriched ^{34}S to facilitate identification of peaks originating from this isotope in the ^{36}S spectra.

Figure 2.2

Position spectra measured at $\theta_{lab}=45^\circ$ for the (d, α) reaction on targets of ^{36}S and ^{34}S . Peaks associated with ^{32}P states, arising from the ^{34}S content in the ^{36}S target, can be identified in the top spectra.



The position spectra displayed in Figure 2.2 comprise the full range of excitation energy measured with both $^{34,36}\text{S}$ targets. A direct correspondence is easily observed between the ^{32}P levels in the lower spectrum and peaks in the ^{36}S spectrum. One notable difference between the two targets, other than the different enrichment of sulfur isotopes, is the presence of ^{26}Al and ^{14}N levels in the ^{36}S spectrum. These peaks are associated with the target contaminants ^{28}Si and ^{16}O , respectively; the silicon is believed to have originated from pump oil when using this target in an earlier experiment.

2.2.2 Analysis and Results

The overall intensity of the data was low and peak centroids were obtained using a weighted sum over the peak width. For well-defined strongly-fed peaks the precision in determining the centroid was 0.3 channels. The centroid of peaks in unresolved doublets was estimated to a precision of one to two channels depending on the statistics. Excitation energy assignments were based on a calibration of channel number with alpha particle energy, determined for each angle and magnetic field using known ^{32}P states. The Enge spectrograph calibration is a fourth order polynomial for ρ , the radius of curvature, as a function of D , the distance along the focal plane. However, the difference, at worst (i.e. when the chosen calibration points are concentrated

entirely at one end of the spectrum), between this fourth order and a linear calibration is about 0.1% across the length of the counter. In general, for well distributed calibration points, the difference is less and can be considered negligible in comparison with the uncertainty in the centroid. Thus, for simplicity, a linear calibration was assumed for $\rho(D)$. The delay line counter can also be calibrated for D in terms of channel number. Since ρ is proportional to $\sqrt{E_\alpha}$, a linear calibration between $\sqrt{E_\alpha}$ and channel number was used to obtain excitation energies.

The calibration points used for the high-energy bite were the ^{32}P levels 1.150, 1.754, and 3.004 MeV. At angles where either of the first two levels were weakly populated the ^{34}P ground state and/or the 1.608 MeV level were used instead. These points spanned a wide range providing a good calibration over the entire spectrum. Because of the high density of states at higher excitation energy in ^{32}P (EX78), it was more difficult to get a good calibration for the low-energy bite. The ^{32}P states used for calibrating this bite, 3.004, 3.443, 3.445, and 4.203 MeV, covered only half the full spectrum range. The uncertainty in the excitation energy at each angle was determined by combining the errors arising from the centroid position and the calibration. A weighted average of the excitation energies was calculated and the results are included in the last column of Table 2.1. The uncertainty

in each value is the weighted standard deviation and thus reflects both the scatter in the values about the mean as well as their uncertainties. The strongly-fed levels which were consistently observed at all angles have been assigned the following energies: 0.430(4), 2.231(10), 2.307(7), 2.683(7), 3.482(8), 4.306(7), 4.438(13), and 4.744(9) MeV. The ground state and 1.608 MeV level are excluded from this list since they were used as calibration points. The states at 3.086(15),² 3.291(23), and 3.546(12) MeV were weakly populated and observed clearly at only one or two of five angles for which measurements were taken.

Our values are in complete agreement with previously established values below 2.31 MeV excitation energy. Above this energy Ajzenberg-Selove et al. have indicated the possible existence of a state at 3.345(20) MeV.¹⁾ This level in our spectra would have coincided with the 3.797 MeV level in ^{32}P . Therefore a weak population of this level would have been unobservable. There were also three states identified by Babenko et al. at 2.372, 2.628, and 3.201 MeV which were not observed in our experiment. In the case of the first two levels, the spectrum background at those excitation energies was quite uniform except for one angle where the ^{14}N ground state peak was present. Therefore no

1) This assignment is tentative since experimental difficulties prevented the measurement of this level at more than one angle.

evidence was found for the presence of these two states. The possibility of a weakly-fed state at 3.201(16) MeV cannot be dismissed entirely since the spectra backgrounds were noisier at this excitation energy. Barring any errors in Babenko's measurements or misprints in the translation of their paper, and since the experiments were performed at different deuteron bombarding energies (Babenko used 3.2 MeV), the existence of these differences in observed excitation energies must be due to changes in the excitation function for the (d, α) reaction populating these final states in ^{34}P .

2.3 SUMMARY

Based on spectra collected at several deuteron bombarding energies and scattering angles six new levels in ^{34}P were identified (see Table 2.1). The resolution of the alpha particle peaks in these spectra was limited by the thickness of the target which was predominantly silver. The silver in the target was also the cause of the high background for spectra taken with 16 MeV deuterons. It would have been desirable to measure angular distributions at this higher energy in order to obtain L-transfer values, however such a measurement was impractical because of the background from the silver.

An additional experiment was undertaken in an effort to obtain some restriction on the spin assignments in ^{34}P . Angular distributions were measured for the $(t, {}^3\text{He})$ reaction on a target of Sb_2S_3 enriched in ^{34}S . This study was motivated by the extensive work of Ajzenberg-Selove et al. (AB85), in which $(t, {}^3\text{He})$ angular distribution measurements were used to determine spins and parities in fp-shell nuclei. Two factors important in the success of their study were: (1) A high triton bombarding energy in order to ensure a dominant direct reaction component and; (2) good statistics for the forward angle measurements since the angular position of the maximum was critical in fitting the data to different L-transfers. In our experiment, complications arose due to the presence of hydrogen in the target which has a very large cross-section for scattering tritons. The maximum angular range for the reaction ${}^1\text{H}(t, {}^3\text{He})\text{n}$ is 18° in the laboratory frame and the kinetic energy of the ${}^3\text{He}$ particles is double-valued. With the widely different kinematic shifts for the two reactions, the ${}^3\text{He}$ particles from the scattering on hydrogen were defocussed on the counter resulting in large backgrounds across most of the spectrum for $\theta_{\text{lab}} < 20^\circ$. Therefore the quality of the data did not permit L-transfer assignments to any of the states in ^{34}P .

Apart from the measured energy levels the only spectroscopic information available for ^{34}P is the 1^+ spin

of the ground state. This leaves a lot of uncharted territory to be explored using the technique of method II angular correlations with polarized deuterons.

CHAPTER 3: T_{20} MEASUREMENTS NEAR 0°

This chapter is divided into three sections. The first section includes a brief description of the polarized ion source, the workhorse for all the experiments described herein, and a definition of the tensor moments associated with the polarized beam. The set-up for the T_{20} experiment is outlined in section two. The analysis of the data and the resulting spin-parity assignments in ^{34}P are presented in the last section.

3.1 POLARIZED BEAM

The polarized ion source used in measurements of both analyzing power and angular correlation was a Lamb-shift type similar to the one first developed at Los Alamos. The design and operation of the source has been described in detail in J. McKay's thesis (Mc76). A brief description is presented here since an understanding of its operation is imperative to the eventual interpretation of the measurements in this and the following chapter.

A schematic of the source is shown in Figure 3.1. It consists of four principal components; the source head, the cesium vapour canal, the spin filter cavity and the argon charge exchange canal. The source head is a high current duoplasmatron source producing positive ions which are extracted and accelerated to 500 eV. At this energy the D^+ ions enter the cesium canal and, through collisions with the cesium, charge exchange to form neutral metastable deuterium atoms in the 2s atomic state. This process is only 30% efficient and the remaining portion of the beam at the exit of the canal consists largely of neutral $D(1s)$ atoms and a small amount of D^+ and D^- ions.

The next stage is the spin filter cavity which comprises an axial magnetic field, a transverse DC electric field and a longitudinal RF electric field. At resonance these fields generate a multilevel interaction which results in the selection of one of the three beam substates $m = -1, 0, 1$. The particular substate selected depends on the magnetic field value. Quenching of the beam occurs when any of the three fields are offset from their resonance value. Of the three possible methods for quenching, a B-field quench is used most often for measuring beam polarization. The quench ratio is defined as $Q = I_t/I_b$, where I_t is the total beam current on resonance and I_b is the current off resonance. Assuming the quenched beam is composed of completely unpolarized beam, the polarization is obtained

Figure 3.1

Polarized ion source schematic showing the main components of the source. Reproduced from (Mc76).

from the quench ratio by the following relation,

$$P = 1 - 170$$

The vector and tensor polarizations defined in terms of P were introduced in chapter one and are listed in Table 1.1.

The transverse E field in the spin filter cavity also serves to deflect the charged species out of the beam. At the entrance to the argon region the neutral beam consists of groundstate, $D(1s)$, and metastable, $D(2s)$, atoms. The charge exchange process preferentially selects the metastable atoms, thus resulting in a polarized D^- beam. An axial magnetic field of 60 Gauss is used to define the polarization axis and select the principal beam substate. Although a lower magnetic field would be desirable for good beam emittance, a higher field is necessary to maximize the nuclear polarization for $m=0$ beam.¹⁾ Since the important quantity for polarization experiments is $P^2 I_t$, a compromise is reached at $B=60$ Gauss where the $m=0$ beam polarization is 98 percent of that obtained from the quench ratio (Oh70).

The negatively charged axially polarized beam out of the source is accelerated to 60 keV for injection to the tandem Van de Graaff accelerator. Before injection the beam

1) The total magnetic quantum number for the eigenstate with $m=0$ and an electronic magnetic quantum number $m_e=1/2$ is $m_t=1/2$. Another eigenstate with $m_t=1/2$ is possible with $m=1$ and $m_e=-1/2$. At low magnetic fields these two states mix thereby reducing the nuclear polarization for $m=0$ beam.

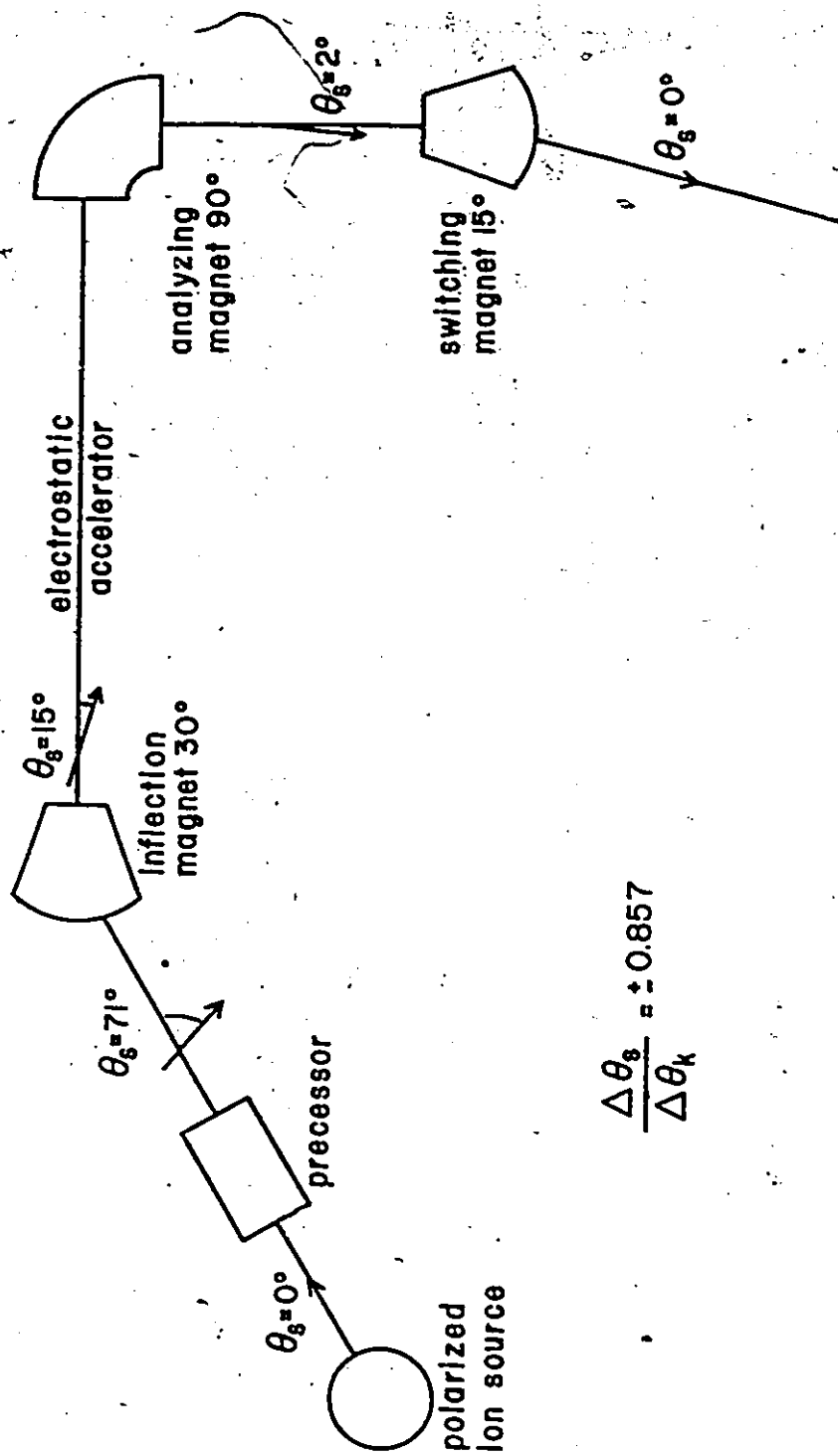
polarization axis is oriented in the precessor. The precessor is a Wien filter whose magnetic field precesses the spin axis while the perpendicular electric field balances the magnetic force on the charged particles. The amount of precession is determined by taking into account the magnetic fields along the beam trajectory from the source to the target. A schematic of the beam transport system is displayed in Figure 3.2. The electrostatic fields in the accelerator do not affect the spin axis orientation and all the important magnetic fields are normal to a horizontal plane. Thus, the precession is confined to the horizontal plane. The magnitude of the nuclear spin precession relative to the beam direction through a magnet is given by the ratio of the Larmor frequency to the cyclotron frequency. This ratio reduces to $\pm g_s = \pm 0.857$ for a positively or negatively charged deuteron, where g_s is the nuclear g-factor. Therefore the spin of a positive ion will precess in the same direction as the beam while that of a negative ion will precess in the opposite direction. The orientation of the polarization axis for transmission down the 15° beam line is indicated in Figure 3.2. A similar set of values can be calculated for the -42° beam line where the spectrograph is located.

Alignment of the polarization axis was verified for the source by measuring the polarization from yield measurements for a reaction with a known analyzing power at

Figure 3.2

Schematic of the beam transport system for the 15° beam line following the McMaster tandem accelerator. The projection is in the horizontal plane and the arrow indicates the direction of the spin axis relative to the beam direction.

Beam Transport System



$$\frac{\Delta \theta_s}{\Delta \theta_k} = \pm 0.857$$

different precessor field settings (Mc76). P varied sinusoidally with the magnetic field and was insensitive, at the level of a few percent, to slight misalignments of the spin axis. During our experiment, the polarization obtained from the quench ratio was verified with the value determined from the tensor analyzing power of a known natural parity state in ^{32}P . The values were consistent with each other within experimental uncertainty and differed by 1.5 percent.

3.2 EXPERIMENTAL SET-UP

The experiment was performed using a polarized deuteron beam incident on the same ^{36}S target used in the scattering experiment described in chapter three. The scattered alpha particles were momentum analyzed with the Enge split-pole spectrograph at $4^\circ \pm 1^\circ$. The unscattered portion of the beam was collected on a suppressed faraday cup and the integrated current from the cup was used to normalize between runs. The cup consisted of a piece of tantalum with a copper edge to minimize scattering into the entrance aperture of the spectrograph. The alpha particles were detected with a focal-plane resistive-wire detector. This gas-proportional detector is similar to the one described in chapter two except that the position signal is derived from a resistive wire (Wi76). Although the position

resolution of this detector isn't as good as that of the delay-line detector, the alpha particles are separated more cleanly in the ΔE spectrum since this latter signal is derived from the front counter.

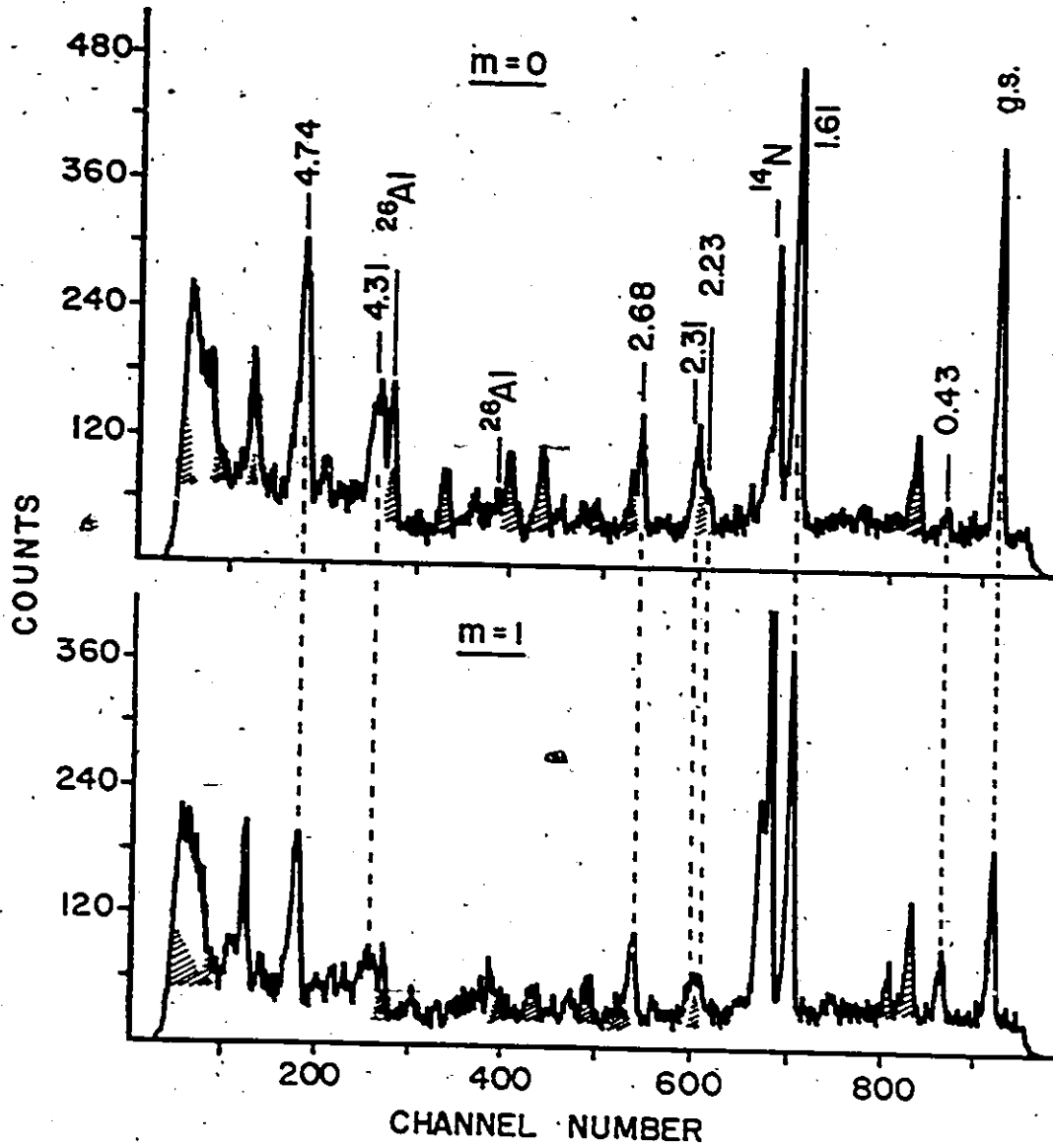
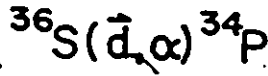
Data were collected at four deuteron bombarding energies, 8.5, 9.0, 9.5, and 10.0 MeV, for both ^{36}S and ^{34}S targets. The spectra collected with the ^{34}S target were of short duration since they were used only to identify the ^{32}P levels in spectra taken with the ^{36}S target. The beam sub-state was switched between $m=0$ and $m=1$ every four hours in an effort to eliminate difficulties with target thickness normalization. The quench ratio was monitored at regular intervals and the polarization ranged between 69% and 74% over the duration of the experiment, with an average target current of 60 nA.

3.3 ANALYSIS AND RESULTS

Sample spectra collected with an $m=0$ and $m=1$, 9 MeV, polarized beam incident on the target of ^{36}S are displayed in Figure 3.3. These spectra are projections taken with the software gate on the alpha particle peak in the ΔE spectrum. The dominant $^{32,34}\text{P}$ peaks are labelled as well as the states in ^{26}Al and ^{14}N identified previously as reaction products from target contaminants. It was not possible to subtract

Figure 3.3

$^{36}\text{S}(\vec{d},\alpha)^{34}\text{P}$ position spectra at $\theta_{\text{lab}}=4^\circ$, with $m=0$ and $m=1$ tensor polarized deuterons. The shaded regions correspond to ^{32}P states.



away the ^{32}P levels from these spectra since the peak width in the spectra collected with the ^{34}S target was slightly narrower.

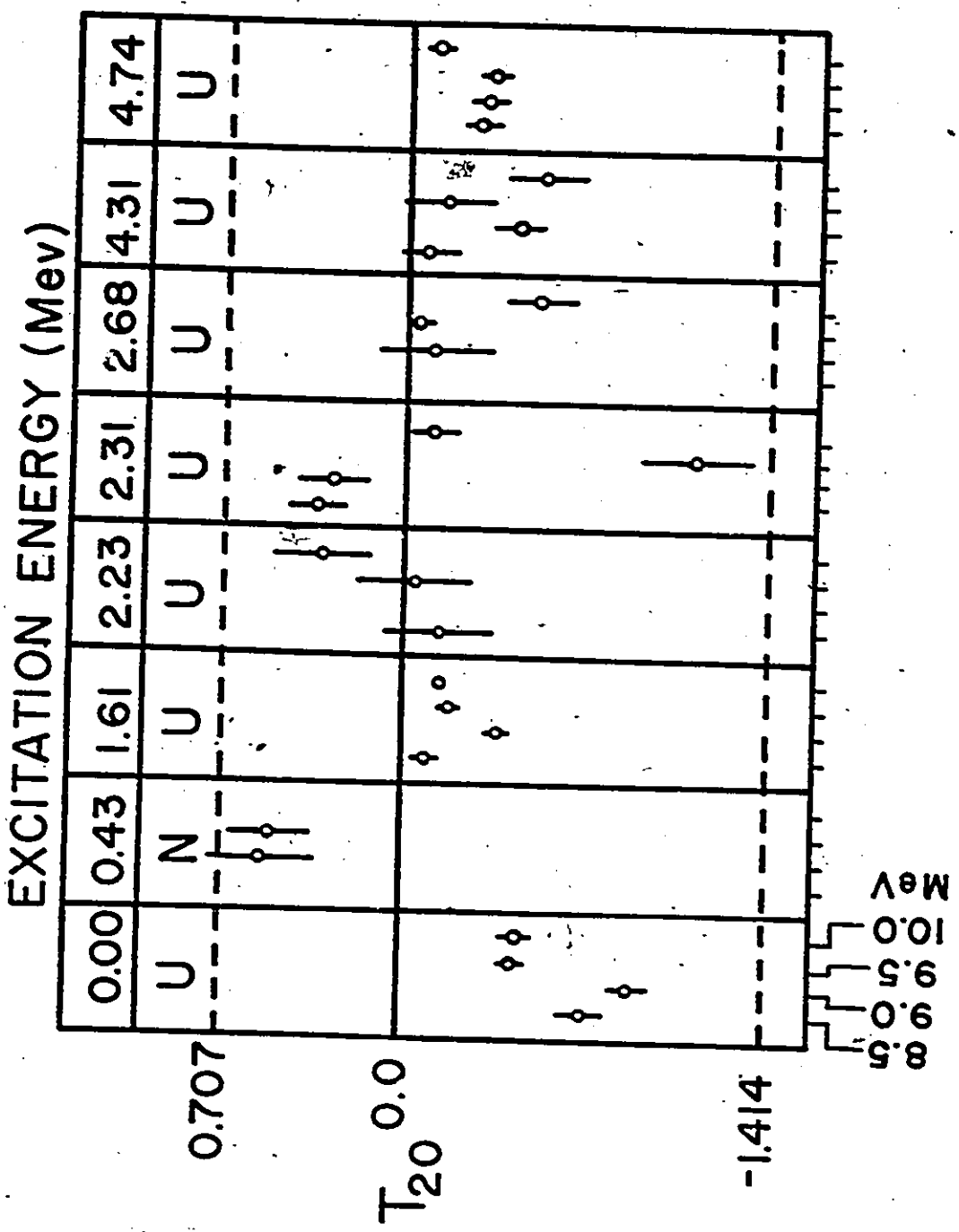
In regions of the spectrum where peaks were well resolved the peak intensity was measured by summing the area above a background. In cases where several ^{32}P and ^{34}P peaks were unresolved that region of the spectrum was fitted, by χ^2 minimization, to a sum of skewed Gaussians using the code PFIT (Bo84). The program first fitted sample peaks by varying the centroid, height, width and skew for each peak independently. Afterwards, the width and skew were fixed at an average of the sample peak values and the rest of spectrum was fitted, allowing only the centroid and height to vary. The particle spectrum calibration, derived from the strongly fed levels, was a second order polynomial of energy as a function of channel number. With this calibration it was possible to verify the centroid values of the peaks by comparing them with the known excitation energies. Also, the intensities for the ^{32}P levels obtained from the fitted spectra were verified with the normalized intensities from the ^{34}S target spectra.

As discussed previously in chapter one, the tensor analyzing power T_{20} can be evaluated in terms of the yields obtained with $m=0$ and $m=1$ polarized beam;

$$T_{20} = \frac{\sqrt{2} (\sigma_1 - \sigma_0)}{P (\sigma_0 + 2\sigma_1)}$$

Figure 3.4

T_{20} tensor analyzing powers for states in $^{34}\text{P}, \pi$ measured at $\theta_{\text{lab}}=4^\circ$ and four deuteron bombarding energies 8.5, 9.0, 9.5, and 10.0 MeV. The labels N and U signify natural, $\pi=(-)^J$, and unnatural, $\pi=(-)^{J+1}$, parity, respectively.



T_{20} values for the levels in ^{34}P are shown in Figure 3.4. The uncertainty in the values includes the error in the yield measurements and an 8% uncertainty in the polarization.

The assignment of natural or unnatural parity is indicated at the top of the figure for each level. The assignment of unnatural parity to the ground state is consistent with the already established spin of 1^+ . With only two T_{20} values for the 0.43 MeV level, the assignment of natural parity can only be made to 97% certainty. The measurements for all remaining states clearly indicate unnatural parity. Of the excited states previously identified in ^{34}P the ones at 3.29, 3.48, and 3.55 MeV were not observed in this study and the 3.09 and 4.44 MeV levels were not populated with sufficient intensity to allow a reliable determination of T_{20} .

CHAPTER 4: ANGULAR CORRELATION EXPERIMENT

This chapter deals with the procedure for measuring method II angular correlations and the analysis of the data obtained for ^{34}P . Ideally detection of the particle and gamma-ray should be made with the most efficient and best resolution detectors. In method II, however, the aligned geometry necessary for the particle-gamma coincidence measurements constrains the solid angle subtended by the particle detector. Thus, in order to obtain coincidence data with good statistics, we had to trade resolution for efficiency in the γ -ray detector; the more efficient NaI detectors were used instead of the high-resolution Ge detectors. With the poorer resolution of the NaI (≈ 80 keV @ 1332.5 keV), a priori knowledge of the decay scheme was necessary. Therefore an initial experiment was performed using a single high-resolution Ge detector to measure the decay scheme and branching ratios in ^{34}P . The details of this experiment as well as the data are presented in section one. In section two the experimental set-up for method II angular correlations is described followed by the procedure for analyzing the data and a discussion of the results for

^{34}P . The final section summarizes the spin and parity assignments made in ^{34}P using the results of the T_{20} measurements presented in chapter three and the results of the correlation experiment discussed in this chapter.

4.1 BRANCHING RATIO MEASUREMENTS

4.1.1 Experimental Set-Up

This experiment was carried out by bombarding an enriched ^{36}S target, described previously in chapter two, with a beam of 8 MeV deuterons. The gamma-rays were detected in a 26% efficient¹⁾ high-purity germanium detector. The singles γ -ray spectra contained γ -ray lines from the residual nuclei associated with the single nucleon transfer reactions $^{36}\text{S}(d,n)^{37}\text{Cl}$, $^{36}\text{S}(d,p)^{37}\text{S}$ and $^{34}\text{S}(d,n)^{35}\text{Cl}$. Transitions in ^{34}P populated by the (d,α) reaction were too weak to be observed. In order to preferentially select γ -rays from the (d,α) channel, the γ -rays were detected in coincidence with the alpha particles. The annular particle detector employed in the method II experiment and shown schematically in Figure 4.4 was used for this coincidence measurement. For this experiment, however, because there were no constraints on the geometry,

¹⁾The efficiency quoted is relative to a 3 inch diameter x 3 inch long NaI detector.

detector was placed close to the target to maximize the solid angle and significantly increase the particle-gamma coincidence count-rate.

The gamma-ray detector was positioned at $\theta=125^\circ$ where most of the angular correlation effects are eliminated, thereby allowing the decay branching ratios from the different levels to be determined; at this angle the Legendre polynomial, $P_2(\cos\theta)$, goes to zero and although $P_4(\cos\theta)$ is not zero the a_4 coefficient is usually small, and the P_{45} term can be neglected. The detector was placed at a backward angle to minimize exposure of the Ge detector to neutrons which were predominantly forward-peaked.

The neutron flux limited the target current to a maximum 2 nA. In an effort to decrease the occurrence of pile-up in the Ge detector, a 3.5 mm thick lead absorber, followed by thin layers of cadmium and copper for absorption of the higher energy Pb and Cd X-rays respectively, were placed in front of the detector. The effect of this absorber was to attenuate, by a factor of greater than two, the intensity of γ -rays below 300 keV. Thus, the singles count-rate was significantly attenuated without losing much intensity for the γ -ray decays of interest.

4.1.2 Analysis and Results

The data were collected using standard slow and fast coincidence circuitry the details of which are presented in

section two of this chapter. Data were event-recorded to magnetic tape for later analysis. The analysis was carried out in the same manner as for the method II experiment outlined in the following section. True γ -ray projections were extracted for different particle windows in an attempt to simplify identification of different γ -ray lines. The projection from the window set on the 1.61 MeV level is displayed in Figure 4.1. Gamma-ray intensities were obtained by subtracting a linear background and summing the peak area. The background was determined using the intensity on both sides of the peak.

Based on the measured geometry of the particle detector a Doppler shift of 6 keV per MeV gamma-ray energy was calculated. Also, the Doppler broadening due to the large solid angle subtended by this same detector was estimated between 3 - 2 keV for excitation energies between 0.5 - 4 MeV in the residual nucleus. In order to include the shift in the energy calibration, the measured γ -ray energies from the β - γ coincidence work of Nathan and Alburger (NA77) were used. These energies were measured to a precision of 2 keV.

The relative efficiency curve for the Ge detector was obtained using a source of ^{152}Eu which has a range of strong γ -rays up to 1500 keV whose relative intensities are well known and tabulated in the Table of Isotopes. Above this energy the efficiency curve for a semiconductor

Figure 4.1

Gamma-ray spectrum obtained with the high-resolution Ge detector in fast coincidence with alpha particles populating the 1.61 MeV level in ^{34}P .

γ-ray Spectrum

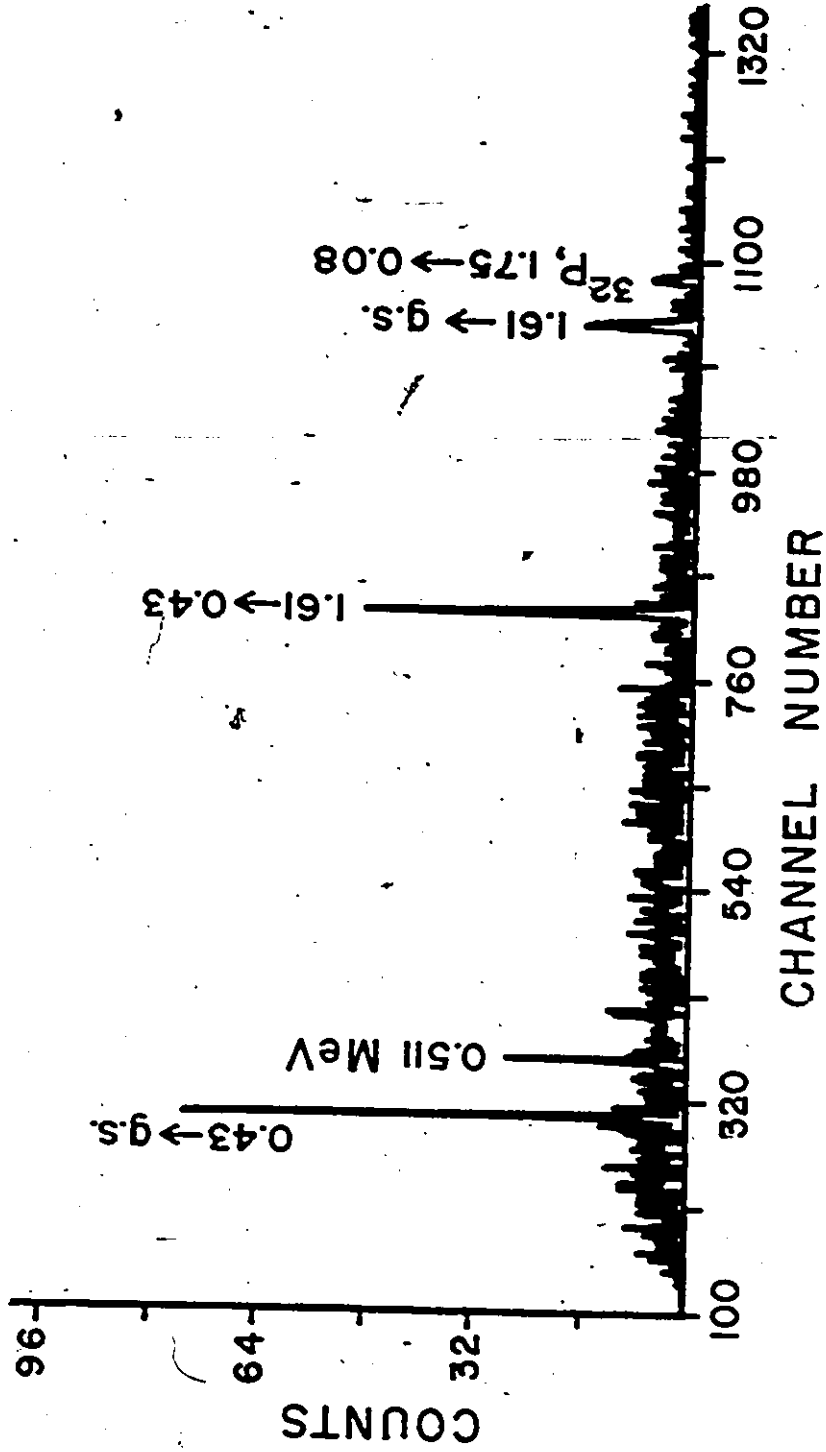
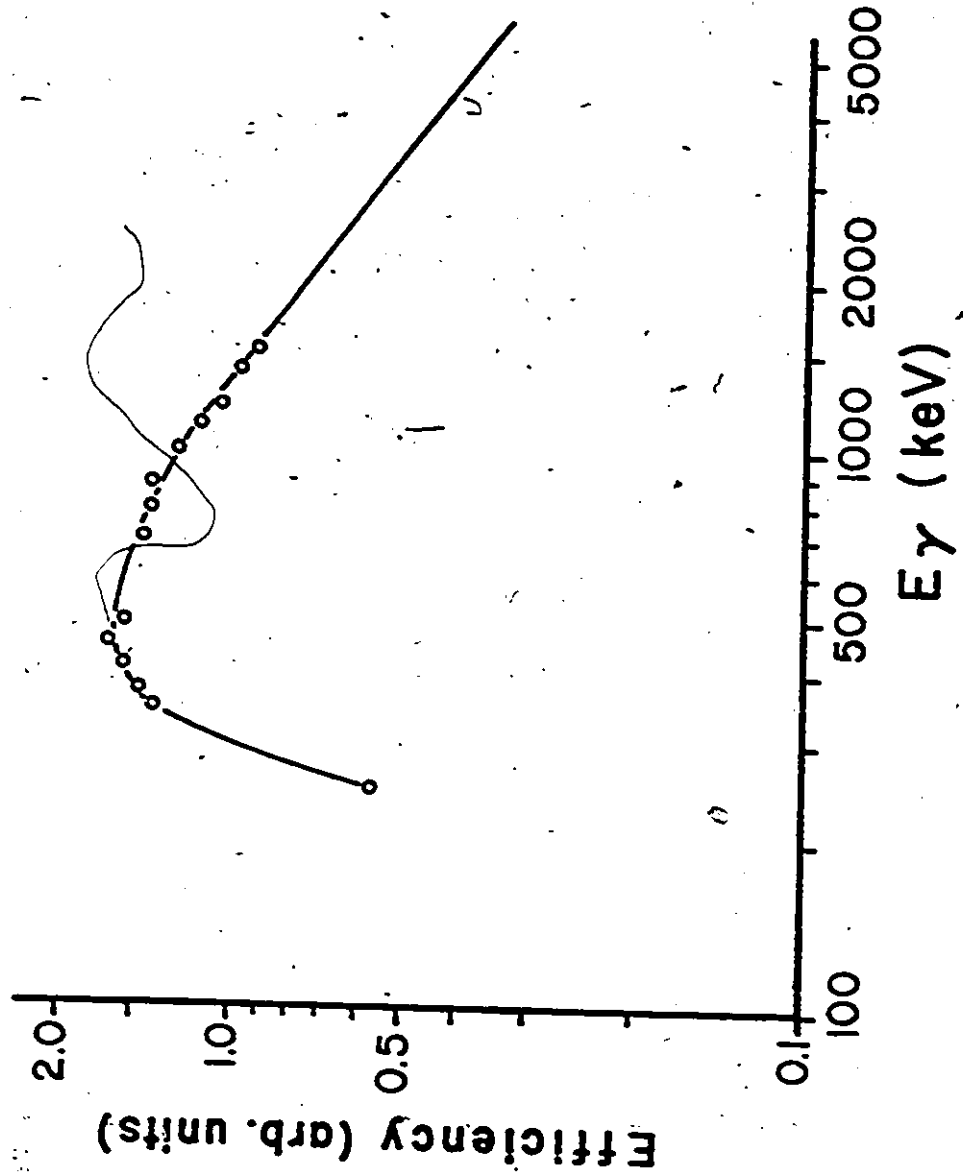


Figure 4.2

Efficiency curve for the 26% germanium detector used for gamma-ray intensity measurements. The statistical uncertainties in the data points lie within the circles shown. The attenuation below 500 keV is due to the 3.5 mm lead absorber in front of the detector.

Ge detector efficiency curve



detector is linear when plotted on a log-log graph. The source intensity measurements were made with the identical source-detector geometry used in the experiment. The measured efficiency curve is shown in Figure 4.2.

The level scheme shown in Figure 4.3 summarizes all observed decays in ^{34}P . The transitions indicated with a dashed line are those for which some uncertainty as to their existence and intensity remains. In particular the transition 2.23 \rightarrow g.s. could not be ascertained as it coincided with the γ -ray from the decay 2.74 \rightarrow .51 in ^{32}P and also with the first escape peak for the transition 2.74 \rightarrow g.s. in that same nucleus. The decay 2.31 \rightarrow 0.43 MeV was not observed in coincidence with alpha particles populating that level but was weakly observed in the decay of higher excited states. The other dashed transitions had low intensity and the subsequent decays were not always identifiable amongst the many transitions in ^{32}P .

The branching ratios for the decay of the 1.61 and 2.68 MeV levels are listed in the third column of Table 4.1. Although the intensities for the decay of the 2.68 MeV level to the state at 2.31 MeV and the ground state had large uncertainties these values were used in obtaining the branching ratios listed in the table. Above this excitation energy branching ratios were not calculated since the existence of possible decays could not be ascertained amidst the large number of ^{32}P decays. The branching ratio for the

Figure 4.3

^{34}P level diagram showing the observed transitions and measured branching ratios. The dashed lines indicate weak or uncertain transitions.

34 P

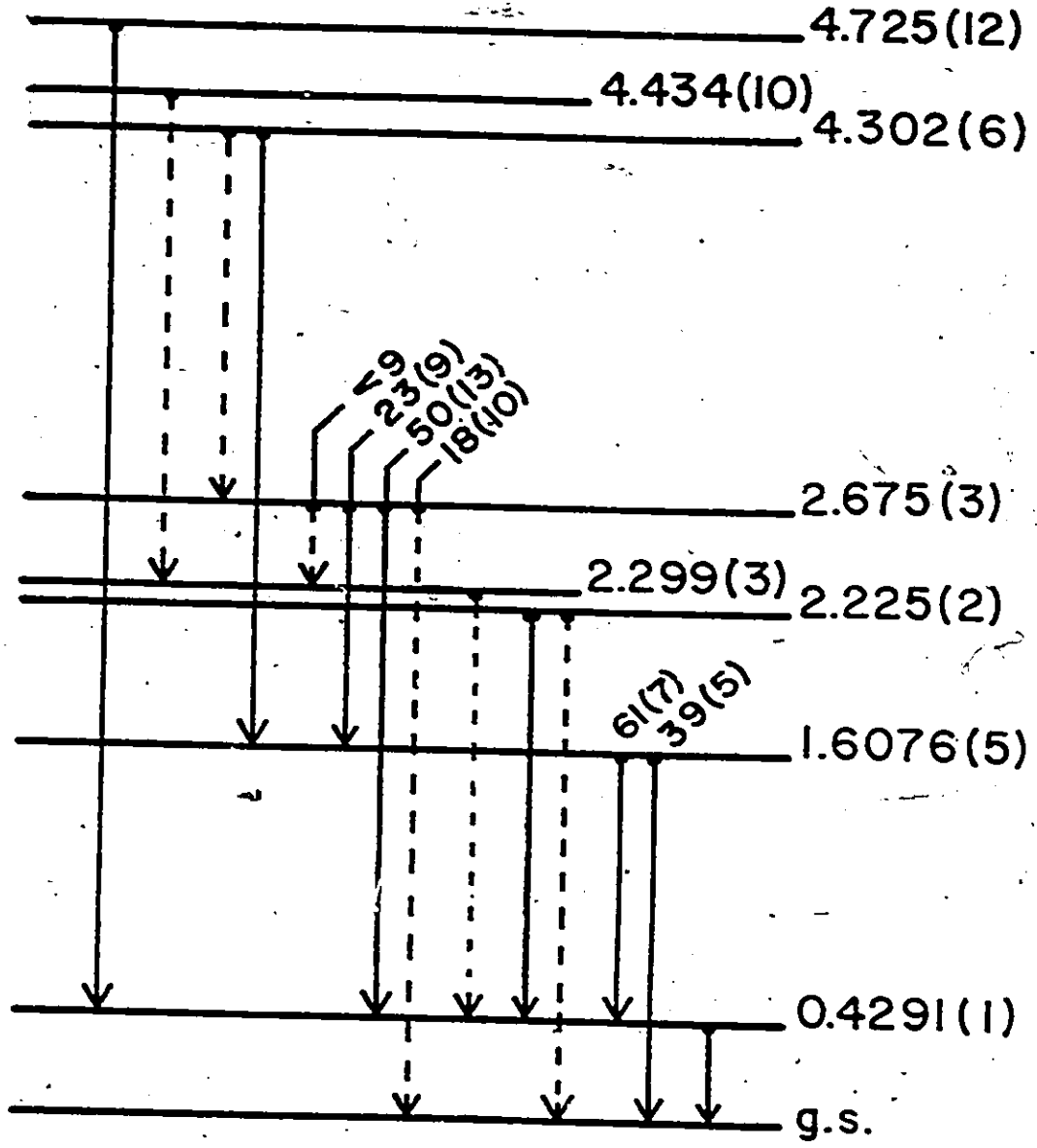


Table 4.1 Gamma-ray branching ratios

nucleus	$E_i \rightarrow E_f$	branching ratio (%)	
		present work	earlier work
^{32}P	1.15 \rightarrow 0.51	47 ± 9	$49.7 \pm 1.7^{\text{a}}$
	\rightarrow 0.08	53 ± 11	42.8 ± 1.3
	\rightarrow g.s.	--	7.5 ± 1.7
^{34}P	1.61 \rightarrow 0.43	61 ± 7	$64 \pm 3^{\text{b}}$
	\rightarrow g.s.	39 ± 5	36 ± 5
	2.68 \rightarrow 2.31	< 9	
	\rightarrow 1.61	23 ± 9	
	\rightarrow 0.43	50 ± 13	
	\rightarrow g.s.	18 ± 10	

a) ^{32}P 1.15 MeV values from $^{29}\text{Si}(\alpha, p\gamma)$ experiment, (EV78).

b) ^{34}P 1.61 MeV values from β - γ coincidence work, (NA77).

decay of the level at 1.15 MeV in ^{32}P is included also, for purposes of comparison with known values listed in the last column of the table. Our results are in agreement with the known values and the branching ratio for the 2.68 MeV level in ^{34}P , hitherto unknown, has been measured.

4.2. METHOD II ANGULAR CORRELATION MEASUREMENTS

4.2.1 Experimental Set-Up

The method II ($\bar{d}, \alpha\gamma$) angular correlation experiment populating the residual nucleus ^{34}P was performed using an 8 MeV polarized deuteron beam incident on a target of enriched ^{36}S . Details of the target, the polarized beam and alignment of the polarization axis along the beam direction have already been discussed in chapters two and three. The polarization was monitored at regular intervals by measuring the quench ratio.

Several factors had to be considered in deciding on a deuteron beam energy of 8 MeV. The Coulomb barrier for alpha particles emerging from the residual nucleus with up to 5 MeV excitation energy required a beam energy in excess of 7.5 MeV. Another factor also favouring a higher deuteron beam energy was the change in separation between inelastic deuterons and alpha particles in the particle detector total energy signal. The separation between the high energy edge

of the inelastic deuterons and the alpha particle peaks increased with increasing beam energy. Unfortunately, with the higher beam energy the neutron flux increased, thus giving rise to a higher background gamma radiation level. Consideration of these factors as well as the yield to different excited states in ^{34}P , led to the selection of 8 MeV for the deuteron beam energy.

A schematic of the target chamber assembly and detector configuration is shown in Figure 4.4. The alpha particles were detected in a 60 μm annular surface-barrier detector positioned at 180° through which the beam was allowed to pass; although detection at 0° would have been preferable because of the larger cross-section, it was precluded owing to the large cross-section for elastically scattered deuterons. The detector had an active area of 300 mm^2 and spanned an angular range of $168^\circ < \theta < 175^\circ$ from the target. The backside and inner hole of the detector were shielded with a tantalum aperture and collimator, respectively. After passing through the target the unscattered portion of the beam was allowed to travel down the beam line to a faraday cup.

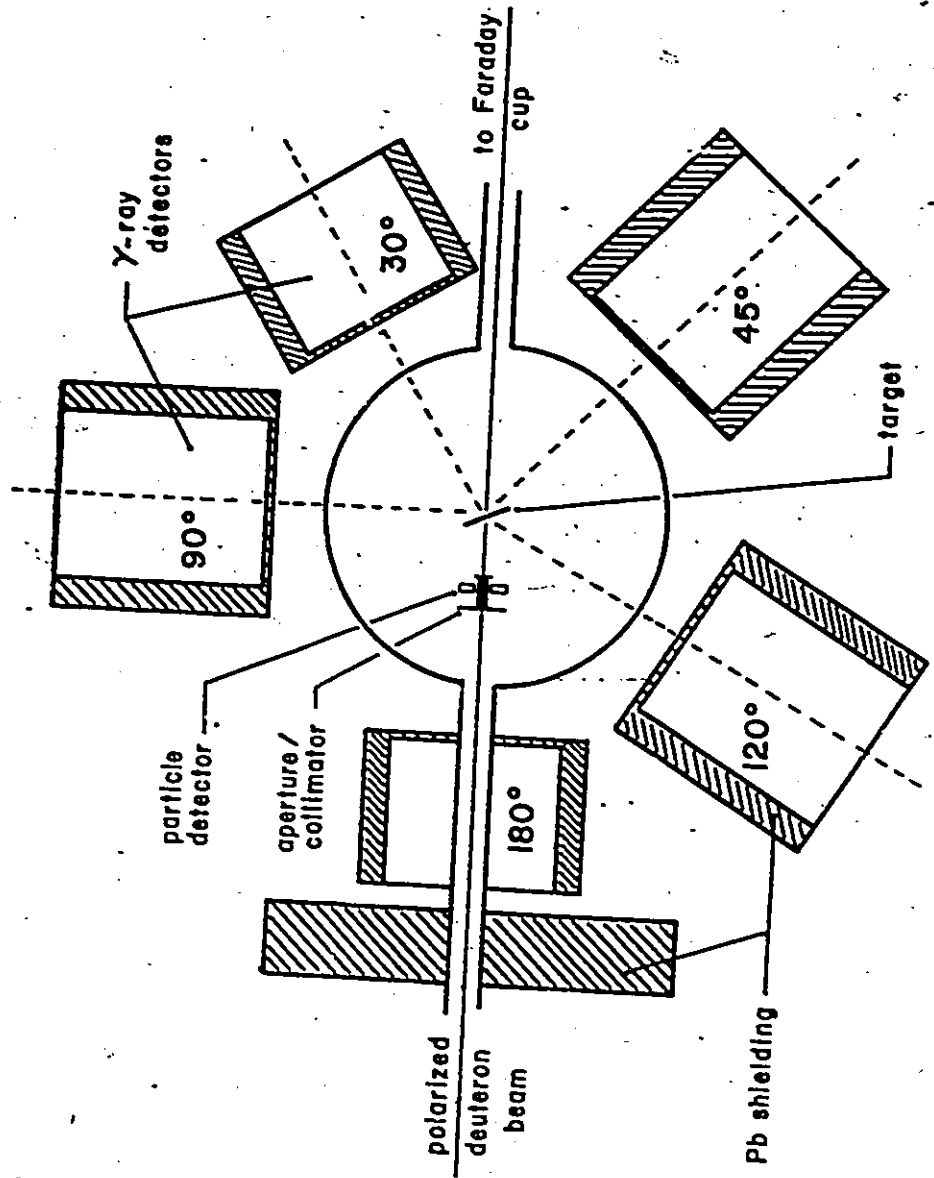
Special care was taken to ensure that the beam axis and the target chamber symmetry axis were collinear. The symmetry axis was naturally taken to be the optical axis of the beamline which could be referenced from the pedestal at the end of the beamline. The target chamber height was

Figure 4.4

Target chamber schematic for method II (d, α)
angular correlation measurements.

20

Target Chamber Schematic



adjusted by sighting from that reference point through to the 2 mm diameter tantalum collimator. A 4 mm diameter aperture positioned 1 meter upstream from the target was also aligned with this axis. At the start of the experiment beam tuning was achieved by minimizing the current on both the upstream aperture and the target chamber aperture-collimator while simultaneously maximizing the current on the faraday cup. After tuning the beam, the upstream aperture was removed for the remainder of the experiment to help minimize beam scattering and thus, background radiation. The portion of beam pipe immediately downstream from the target chamber was lined on the inside with a thin sheet of tantalum.

Due to the low cross-section for the (d,α) reaction, the coincident gamma-rays were detected at different angles, simultaneously, using five large NaI(Tl) detectors. Four of the detectors were solid cylindrical crystals with a photomultiplier tube (PMT) on the back face of the cylinder. These were placed at $\theta = 30^\circ, -45^\circ, -120^\circ$ and 90° with respect to the beam direction. Three of the four had dimensions 12.5 cm dia. X 15 cm long and the other was shorter with dimensions 12.5 cm dia. X 10 cm long. The fifth detector, at 180° , had the same dimensions as the smaller crystal with the differences of a 2.5 cm bore along the cylinder axis, through which the beam pipe fit, and two cuts on opposite sides of the crystal for mounting the photo-

multiplier tubes in order to collect all the light from the crystal.

The response of each detector was optimized by finding the PMT bias voltage which resulted in a minimum FWHM for the ^{60}Co lines at 1173.5 keV and 1332.3 keV. The resolution of the 180° detector was optimized by also matching the gains of the two PMTs. The detector resolutions are listed in Table 4.2 for source and in-beam conditions. The poorer resolution under source conditions for the 180° crystal is largely attributable to the poor quality of the crystal and not the split geometry for the light collection. In all cases the in-beam resolution was about 20 percent worse than that measured with a source. This was undoubtedly a consequence of the high singles count rate in each detector. Even with a beam current of 15 nA on target and a 3.5 mm lead absorber in front of the detectors to attenuate the count rate from low energy γ -rays, the singles count rate was recorded at 30 Kcounts/sec. Such a large count rate generated a sizeable current through the resistor chain of the PMT and resulted in a gradual gainshift. The already poor resolution of the 180° detector under source conditions was compounded by uncorrelated gainshifts from its two PMTs rendering the gamma-ray data from this detector virtually unusable.

Table 4.2 NaI detector Resolution

detector	θ	FWHM (keV)	
		source ^{a)}	in beam ^{b)}
1	30°	95.2 ± 0.3	114 ± 4
2	-45°	83.4 ± 0.3	101 ± 4
3	-120°	84.1 ± 0.4	102 ± 5
4	90°	91.8 ± 0.3	100 ± 4
5	180°	193.0 ± 0.7	---

a) 1274 keV line in ^{22}Na .

b) 1180 keV line in ^{34}P .

4.2.2 Electronics

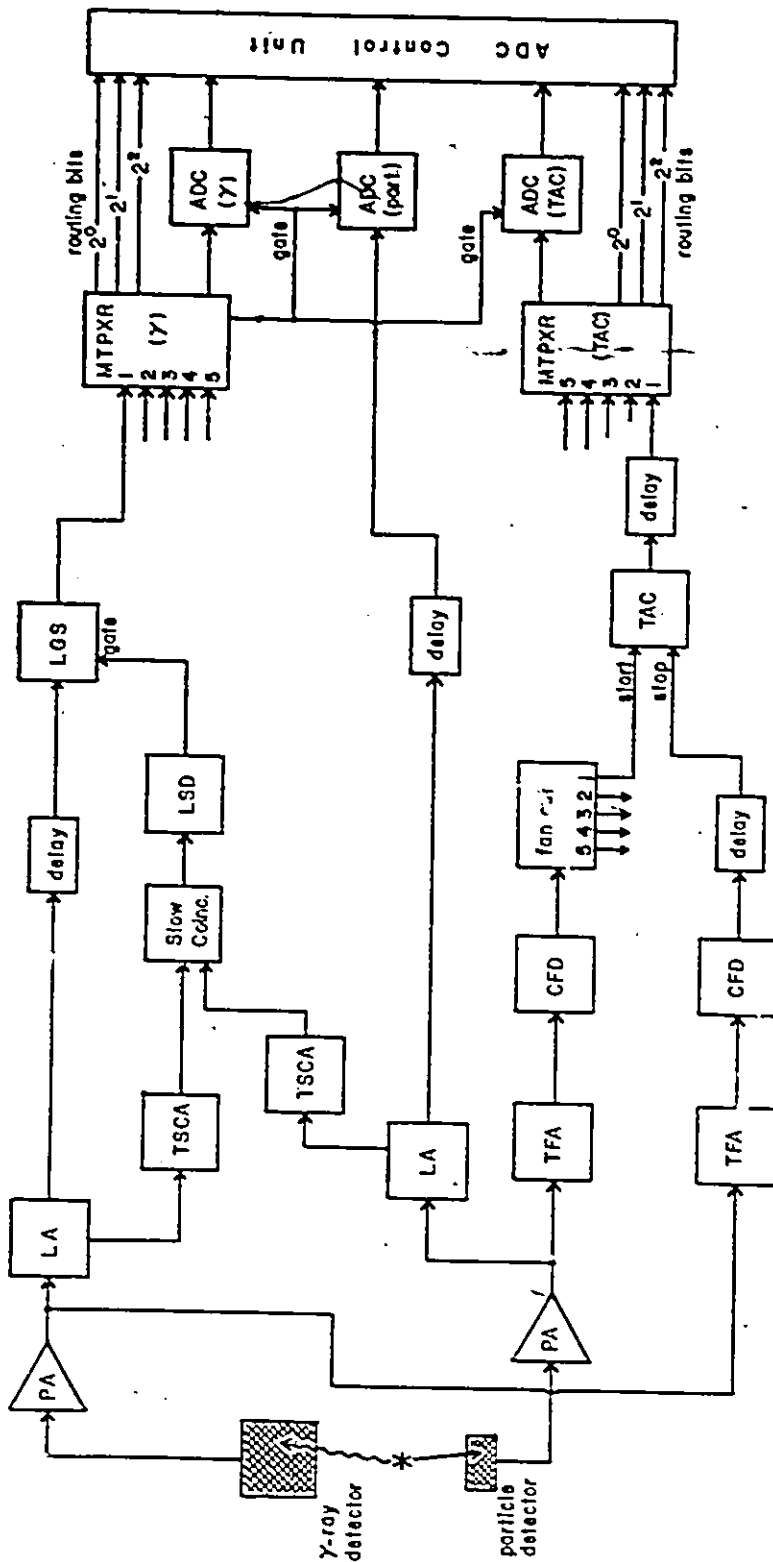
The linear energy signals from each of the five gamma-ray detectors in conjunction with that from the particle detector were used to trigger both slow and fast coincidence electronics. A schematic of the electronics for one detector is included in Figure 4.5. Similar electronics were used for the other four detectors, with the exception of the 180° detector for which the linear signals from the two PMTs were summed together initially and then used to trigger the coincidence electronics.

The electronics consisted of two parts: (1) the slow-timing part, where discriminator levels were set to exclude the low energy inelastic deuteron events and low energy γ -ray events; (2) the fast-timing part, where discriminator levels were set low to ensure good fast-timing pick-off for both the particle and γ -ray signals. The slow-timing coincidence signal generated by logic signals from the output of the timing single channel analyzers (TSCAs) for the particle and γ -ray signals was used to gate the singles γ -ray signal in the linear gate and stretcher (LGS). Gating the linear γ -ray signal at this point greatly reduced pileup at the input to the multiplexer. The fast-timing coincidence signal was derived from a time-to-amplitude converter (TAC) whose start input was triggered by the output of the timing-filter amplifier (TFA) and constant-fraction discriminator (CFD) for the particle

Figure 4.5

Block diagram of the slow and fast coincidence electronics for one gamma-ray detector. The abbreviations for the different modules are the following:

- ADC - Analogue to Digital Converter
- CFD - Constant Fraction Discriminator
- LA - Linear Amplifier
- LGS - Linear Gate and Stretcher
- LSD - Logic Shaper and Delay
- MTPXR - Multiplexer
- PA - Preamplifier
- TAC - Time to Amplitude Converter
- TEA - Timing Filter Amplifier
- TSCA - Timing Single Channel Analyzer



Electronics Block Diagram

signal, and whose stop input was triggered by a similar combination of TFA and CFD for the γ -ray signal. An external delay of 400 nsec was added to the stop electronics to ensure good definition of the true coincidence peak in the TAC spectrum with a full-scale setting of 800 nsec. The TAC output signal, delayed to arrive in time with the linear particle and γ -ray signals, was connected into the TAC multiplexer. The three analogue-to-digital converters (ADCs), set to 1K conversion gain and gated by the output gate signal from the γ -ray multiplexer, recorded the particle, gamma-ray and TAC signals, respectively. The routing bits from the γ -ray and TAC multiplexers were read synchronously with the ADC content by the ADC control unit and stored in the high bits of the 16-bit data word.

On-line data acquisition was performed using a VAX 11/750 and the EVAL data-handling routines. The data were event-recorded on magnetic tape for later off-line analysis. Every two hours, the beam polarization was recorded and the electronics monitored to guard against possible module failure. Data acquisition lasted 6 days, alternating every data tape between $m=1$ and $m=0$ deuteron beam substate. This corresponded to a cycling time of approximately 6 hours.

4.2.3 Coincidence Experiment Analysis

Event-recorded data were sorted off-line with

windows set on the alpha peaks of interest in the particle spectrum. An energy calibration based on the known low energy states in ^{32}P and ^{34}P was used to identify the alpha particle peaks. Sample spectra collected with $m=0$ and $m=1$ deuterons are shown in Figure 4.9. The resolution of 60 keV was limited mostly by the differential energy loss of the back-scattered alpha particles in the target. In comparison the effect of the finite solid-angle subtended by the particle detector from the target was negligible.

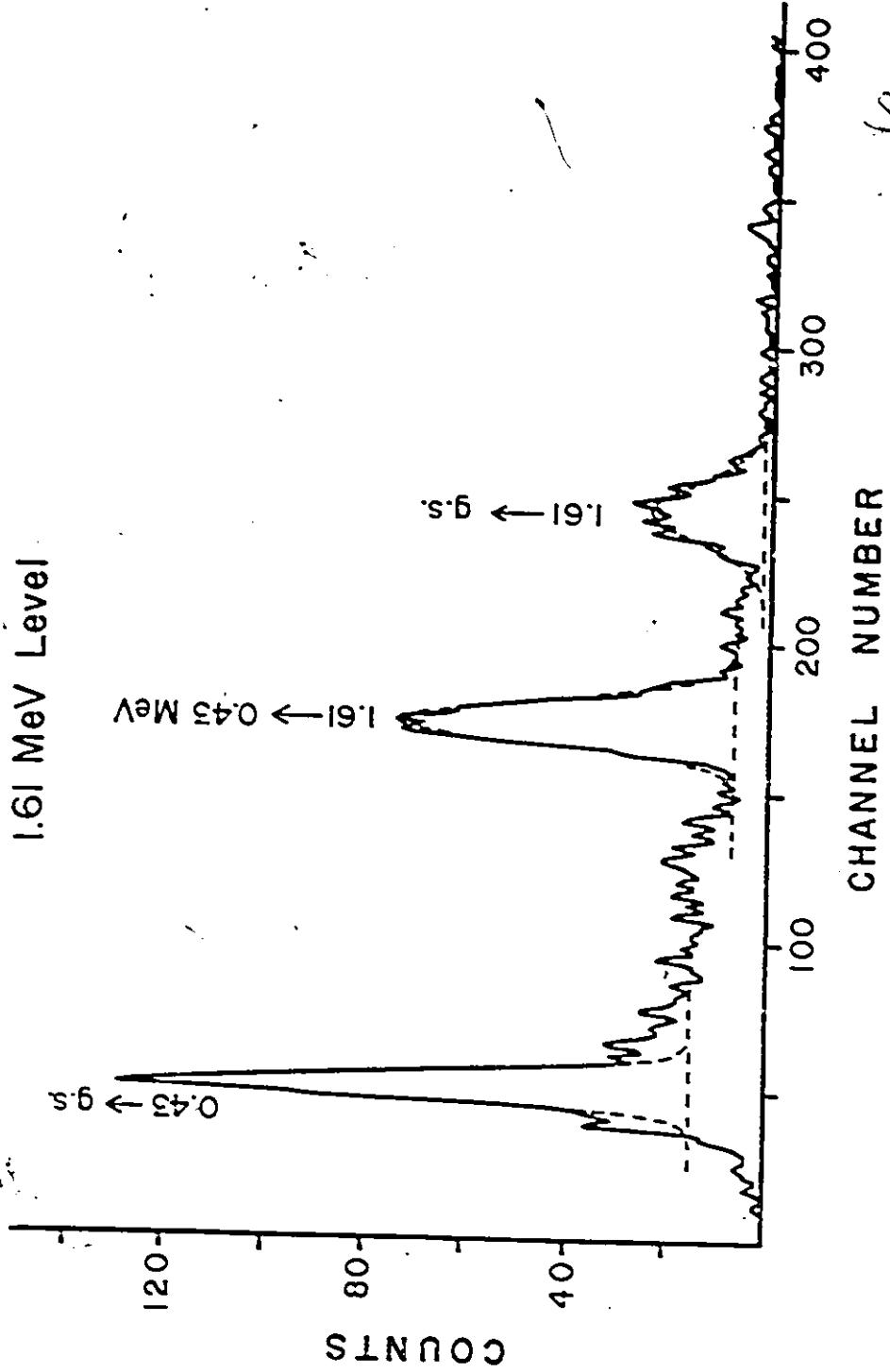
A projection of the TAC spectrum was generated for each particle window and gamma-ray detector. The random coincidence events under the TAC true coincidence peak were excluded by subtracting from the TAC peak γ -ray projection, a γ -ray projection from the random background above and below the peak. A sample subtracted γ -ray spectrum is shown in Figure 4.6 for the particle window on the 1.61 MeV level. All data were sorted from tape in this manner and similar spectra were obtained for the other detectors.

The data, sorted off-line from tape, were corrected for gain shifts. Lacking a strong gamma-ray line of sufficiently high energy to accurately monitor the gain shift over short time-intervals, an average gain correction for each data tape was calculated using the decay of the strongly fed 1.61 MeV level in ^{34}P . The centroids of the gamma ray lines at 430, 1180, and 1610 keV were used to estimate the zero offset and gain shift. This gain

Figure 4.6

Gamma-ray spectrum at $\theta=60^\circ$, in coincidence with alpha particles populating the 1.61 MeV level. The dashed line shows the background level determined from the spectrum background below the peak, and the best-fit Gaussian obtained for each peak separately (see section 4.2.2). The cut-off at low energy is from a discriminator level and the shoulder above the 0.43 MeV Y-ray is due to remnants of the 0.511 MeV Y-ray from random coincidence events.

γ-ray Projection For The 1.61 MeV Level



correction has been incorporated in the γ -ray projection shown in Figure 4.6, which corresponds to the combined $m=0$ data from 9 data tapes recorded over the six-day period.

4.2.4 Peak-Fitting Procedure

Gamma-ray intensities were extracted from the projected spectra for the photopeak and, where possible, for the escape peaks. The functional form for the photopeak shape suggested by Heath (He66) in his paper on the analysis of γ -ray spectra measured with NaI detectors, was a modified Gaussian of the form,

$$y(x) = H \exp\left[-\frac{(x-x_0)^2}{2\sigma^2} \right] \left[1 + \alpha_1(x-x_0)^4 + \alpha_2(x-x_0)^{12} \right]$$

where the parameters α_1 and α_2 were determined empirically. He found the logarithm of these parameters decreased linearly with the logarithm of γ -ray energy above 500 keV. Our values for α_1 and α_2 were obtained by fitting spectra collected with standard gamma-ray sources using the same source-detector geometry as that used during the experiment. The statistics for these spectra were in all cases better than one percent. The best-fit values for these parameters at the γ -ray energies 511, 1274, and 2614.5 keV were all, within error, equal to zero. Thus a simple Gaussian curve

could be used to describe the photopeak response of our NaI detectors.

The photopeak intensity was extracted by first subtracting a background level determined by averaging the spectrum background, above the peak, over several channels. Then, a chi-square minimization algorithm, CURFIT (Be69), using a Gaussian shape with variable peak position, height and width was used to fit the peak and determine the area. Although this least-squares fitting procedure was simple to implement, one had to be careful about defining the fitting region for the peak. Owing to the higher background on the low-energy side of the peak from small-angle Compton scattering in the absorber, the area of the best fit peak was sensitive to the position of the lower bound of the fitting region. Figure 4.7 shows a sample line shape for the 511 keV γ -ray obtained with one of the NaI detectors. The markers labelled A to D correspond to different lower bounds for the fitting region and the marker labelled U refers to the upper bound. The parameters of the best fit Gaussian over these different regions are listed in Table 4.3. The best reduced chi-square occurs for the lower bound C and the resulting fit is shown as the dashed line in Figure 4.7. With the lower bound set lower than this, the Gaussian width and consequently the area is overestimated. To ensure consistent results when fitting spectra the lower bound of the fitting region was always set at half the full

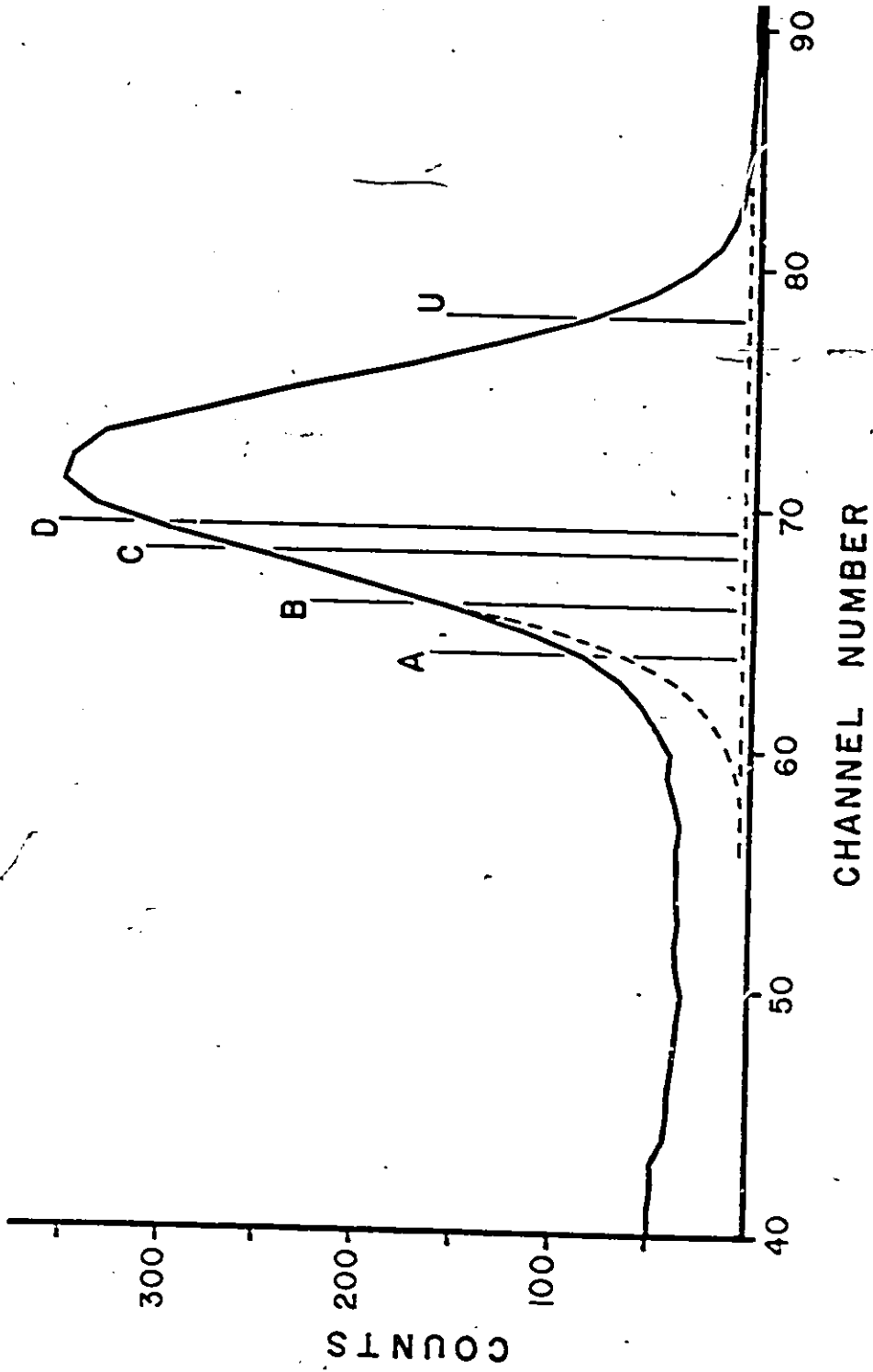
Table 4.3 Peak-fit parameters for the regions displayed in Figure 4.7

Region	X_v	FWHM	Area $\times 10^3$
A - U	21.0	$9.70 \pm .03$	$304.6 \pm .6$
B - U	6.4	$9.42 \pm .03$	$299.4 \pm .6$
C - U	2.2	$9.21 \pm .05$	$294.3 \pm .6$
D - U	3.1	$9.18 \pm .08$	$293.3 \pm .6$

Figure 4.7

The solid line is the measured line shape for the 511 keV gamma-ray. The markers A to D correspond to different lower bounds of the fitting region, while U is the upper bound. The dashed curve is the fit obtained with the lower bound C. Note that since all the detectors have similar geometry and the same thickness absorber, to a first approximation the error made in excluding some of the photopeak by using a straight Gaussian is the same fraction of the peak at every angle. Since the overall normalization of the angular correlation is unimportant, this error does not affect the correlation results.

SAMPLE PEAK SHAPE



peak height.

The non-linear least-squares fitting algorithm mentioned above is valid provided the fitting function accurately describes the data and the data obey Gaussian statistics. In the limit of a large number of events the Poisson statistics of a counting experiment behave like Gaussian statistics. However, when the number of counts is low, as in the case of our projected γ -ray spectra, the approximation is not valid and use of a least-squares algorithm to fit the data is dubious. It can be shown that the area under the Gaussian curve estimated using the method of least-squares is less than the 'true' area by an amount approximately equal to chi-square for the fit (Be69). One method for reducing chi-square is to smooth the data by averaging over adjacent channels. This smoothing has the effect of leaving the area of the peak unchanged while modifying the peak height and width to produce a smoother curve with a χ^2 lower by an order of magnitude. Thus, the precision gained in estimating the peak area is balanced by a loss of precision in the peak width.

The number of channels used for averaging was typically half the peak width. The dashed curves shown with the gamma-ray spectrum in Figure 4.6 correspond to the least-squares fit for the smoothed data. The data are well reproduced for all three ~~gamma-ray~~ lines. This procedure, used to fit all the data, provided a consistent and reliable

method for extracting peak intensities.

4.2.5 Efficiency Correction

The correction for efficiency was performed in two steps because one of the detectors was significantly smaller than the others. Had they all been the same size and positioned at the same distance from the target, the relative detector efficiency would have been obtained simply by measuring the detector yields for a known correlation; the difference in detector efficiency then being only a result of the different efficiency of the electronics for each detector. However, with two detectors physically different, their efficiency correction relative to the other detectors depended on the γ -ray energy. The energy dependence was determined by measuring source intensities at different energies using the same source-detector configuration as in the experiment. These measurements are tabulated in Table 4.4. The detector efficiency correction for other gamma-ray energies was obtained by linearly extrapolating from these values (We63).

Detector #5 is the 180° detector and, due to poor resolution, was not used in the correlation analysis. The differences in efficiency between detectors #2, 3 and 4 were small and probably a result of slightly different target-detector distances. Detector #1 was the smaller detector and its efficiency relative to detector #4 varied with energy. These results corroborate those of Weitkamp (We63)

obtained from Monte Carlo calculations for the photopeak efficiency as a function of energy for different size NaI detectors.

The above measurements yield the energy dependence of the relative detector efficiency. The total relative efficiency correction must include the effect of the electronics and can be determined only by measuring the yield for a known particle-gamma correlation. The data collected during the experiment contained two such candidates from the reaction $^{28}\text{Si}(d,\alpha)^{26}\text{Al}$: (1) the pure dipole 1.06 \rightarrow 0.23 MeV, $1+ \rightarrow 0+$ transition; (2) the stretched E2 transition 0.42 \rightarrow 0.00 MeV, $3+ \rightarrow 5+$. With measured correlations for these transitions with both $m=0$ and $m=1$ deuteron beam sub-states, a unique efficiency correction factor was calculated for each of the four detectors. The population parameters required for the calculated correlation curves were obtained using the ratio of the cross-sections for the two beam sub-states as described in chapter one. The efficiency correction factors obtained are listed in the column labelled f_i in Table 4.4. The error listed includes both the statistical uncertainties in the measured correlation data and the error in the calculated correlation function arising from the uncertainty in the population parameters. The total efficiency correction for each detector is a product of an energy-dependent term and an electronics correction term. Therefore we can write, for the total efficiency,

Table 4.4 Relative detector efficiency^{a)}, ϵ_4/ϵ_i ,
and electronic efficiency correction, f_i ,
for different γ -ray energies (MeV)

i/E_γ	ϵ_4/ϵ_i			f_i
	.511	1.274	2.614	
1	0.96	1.18	1.37	0.88 ± 0.04
2	1.02	1.02	1.03	1.05 ± 0.04
3	1.02	1.02	1.03	1.00 ± 0.04
4	1.00	1.00	1.00	0.78 ± 0.04
5	2.37	2.35	2.00	----

a) uncertainty for efficiency is less than 1%

$$\epsilon_{\text{tot},i}(E) = \epsilon_i(E) \times f_i \quad i = 1, \dots, 4$$

where E denotes the energy dependence and i labels the detector.

The calculated correlation curves and the correlation data, corrected for total efficiency, for both transitions in ^{26}Al are shown in Figure 4.8. The larger than expected chi-square for an acceptable fit (i.e. $\chi^2_{\nu} = 1$) reflects the overestimation of the experimental precision. The uncertainties for the measured correlations are statistical errors only and do not include any uncertainty in determining the background level.

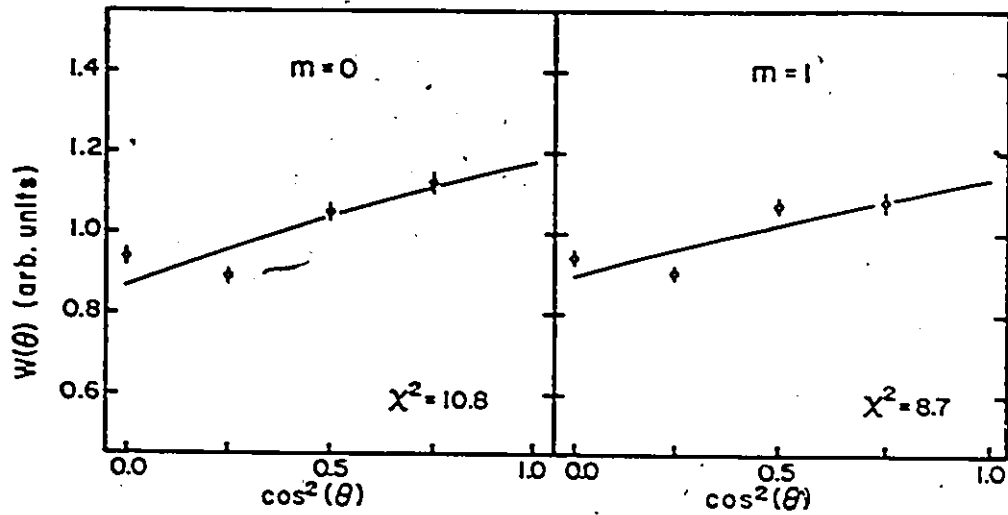
4.2.5 Results and Discussion

Coincidence particle spectra collected with an $m=0$ and $m=1$ deuteron beam are displayed in Figure 4.9. There was a noticeable difference between these spectra collected with a 200 nsec TAC timing window and those collected with a slow coincidence, 2 μsec , timing window. In particular the background at low energy caused by the large cross-section of inelastically scattered deuterons was attenuated considerably in the former spectra. Another difference, consistent with the lower true to random ratio for the 2 μsec coincidence spectra, was the stronger ground state alpha particle peak relative to the excited state peaks in those spectra. High energy alpha particle peaks were

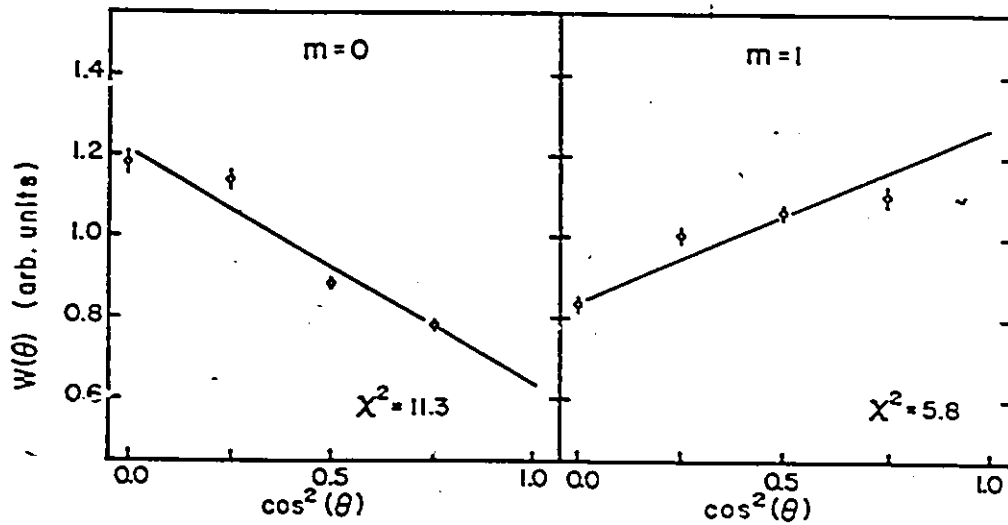
Figure 4.8

Efficiency-corrected angular correlations for two transitions in ^{26}Al . The solid lines are the best-fit correlations obtained by allowing the population parameters to vary within ten percent of the calculated value. The chi-square for each fit is included in the lower right-hand corner.

^{26}Al 0.42 \rightarrow 0.00 MeV ($3^+ \rightarrow 5^+$)



^{26}Al 1.06 \rightarrow 0.23 MeV ($1^+ \rightarrow 0^+$)



clearly identified with the different excited states of ^{32}P and ^{34}P . Due to the larger level density at higher excitation energy, particularly in ^{32}P , the levels were not resolved in the particle spectra.

Of the many other impurities known to be present in the target (Ra84), only ^{28}Si , ^{14}N and ^{10}B were observed in our experiment. The position of alpha particle peaks from the (d, α) reaction on these target contaminants is indicated in Figure 4.9. The background of high-energy alpha particles above the ground state energy peak of ^{32}P is thought to be associated with the reaction $^{10}\text{B}(d, \alpha)^8\text{Be}$; the Q-value for the reaction is 17.86 MeV and ^8Be decays into two alpha particles. The reaction cross-section to ^{26}Al was much larger than that for the phosphorus isotopes and, as discussed above, the observed transitions in this residual nucleus were extremely useful for obtaining relative detector efficiency corrections. The first excited state of ^{12}C , at 4.44 MeV excitation energy, was observed on the shoulder of the peak associated with the 1.15 MeV level in ^{32}P . Because this state has natural parity ($J^\pi=2^+$) it was much more intense in the $m=1$ than in the $m=0$ spectrum. The ground state and second excited state at 7.65 MeV are $J^\pi=0^+$ states and therefore were not populated with either beam substate. The 3^- state at 9.64 MeV excitation energy will be discussed in the context of the 4.74 MeV level of ^{34}P as the two levels were populated with alpha particles of approximately

Figure 4.9

Coincidence particle spectra from method II angular correlation measurements with 8 MeV, $m=0$ and $m=1$ deuterons. Excited states of ^{34}P , ^{32}P , ^{26}Al , and ^{12}C are plotted at the right in terms of the scattered alpha particle energy at $\theta_{\text{lab}}=170^\circ$. The arrows between dashed lines indicate the particle windows used for obtaining gamma-ray coincidence projections for the levels of interest in ^{32}P and ^{34}P .

Errata: The levels in ^{34}P labelled 2.21 and 2.23 MeV should be 2.23 and 2.31 MeV, respectively.

the same energy. Aside from the decays from these impurities all of the observed γ -ray transitions were identified with known ^{32}P decays (EV78) or expected ^{34}P transitions.

Gamma-ray intensities were extracted and corrected for total efficiency in the manner described in the previous section. The calculated correlation function, used for making spin and parity assignments by comparing with the data, was derived for the aligned geometry of method II in chapter one and its final form is repeated here;

$$W(\theta) = W_0 \sum_{k \text{ even}} B_k(J_1) Q_k \left[\frac{R_k(LL) + 2\delta R_k(LL') + \delta^2 R_k(L'L')}{1 + \delta^2} \right] \times P_k(\cos\theta). \quad (4.1)$$

The attenuation coefficients, Q_k , which correct for the attenuation of the measured correlation due to the finite size of the γ -ray detector are listed in Table 4.5 for different γ -ray energies. All the values except those at 4.31 MeV are based on the paper of Twin and Willmott (TW63). Their values were calculated, for different source to detector distances, from experimental measurements of the photopeak efficiency for a 5 in. diameter by 6 in. long NaI crystal. The same Q_k was used for all four detectors, including the shorter one at 30° . Although the detector photopeak efficiency, which is proportional to J_0 , is appreciably different for the smaller detector (see Table 4.4), the attenuation coefficient, which depends on the ratio

Table 4.5 NaI detector attenuation
coefficients

E_{γ} (MeV)	Q_2	Q_4
0.43	.93	.77
1.18	.94	.80
1.61	.94	.80
4.31 ^{a)}	.92	.76

a) includes both photopeak and first escape peak.

J_k/J_0 (see Appendix), changes by less than one percent for the relevant energies and the source to detector distance used in this experiment (MY68). The values of Q_k for 4.31 MeV were based on calculated values for the total gamma-ray spectrum (GR58) since the first escape peak intensity was included along with that of the photopeak in the analysis.

The population parameters which, aside from a Clebsch-Gordan coefficient, determine the statistical tensor coefficients, B_k , were evaluated using the equation and inequalities outlined in section 1.3.4. Because of the approximations inherent in obtaining the parameters this way, their values were allowed to vary within 10% of the calculated values for determining the best fit correlation.

For any given initial and final spin the R_k values are determined uniquely and the only remaining free parameters in the expression for $W(\theta)$ are the mixing ratio, in the case of mixed multipolarity transitions, and the overall normalization, W_0 . For each value of the mixing ratio a normalization factor W_0 , yielding the best agreement with the data, was obtained for the $m=0$ and $m=1$ correlations separately. The combined chi-square for both correlations was plotted on a χ^2 versus $\arctan(\delta)$ graph. Such plots were repeated for different values of the population parameters within the range mentioned above and all possible initial spin values in an attempt to uniquely identify the spin and parity of the levels. in ³⁴p.

The criterion defining an acceptable fit was based on the chi-square corresponding to a 99% confidence limit; that is, the range of mixing ratio values yielding a fit with a chi-square below that corresponding to the 99% confidence limit, bracketed the 'true' value of the mixing ratio for the transition with a probability of .99. The chi-square value defining this confidence limit is a function of the number of degrees of freedom for the fit, which in turn depends on whether one or both correlations are measured for the transition. This level is shown as a solid horizontal line in the χ^2 versus $\arctan(\delta)$ plots.

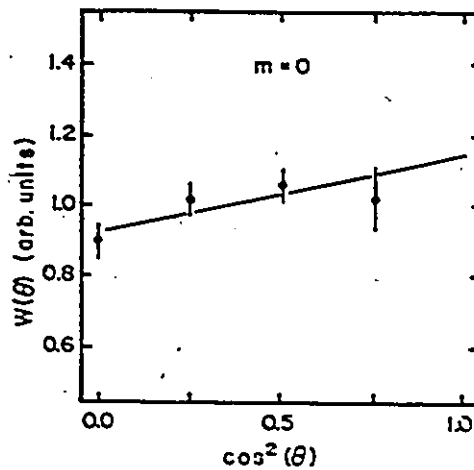
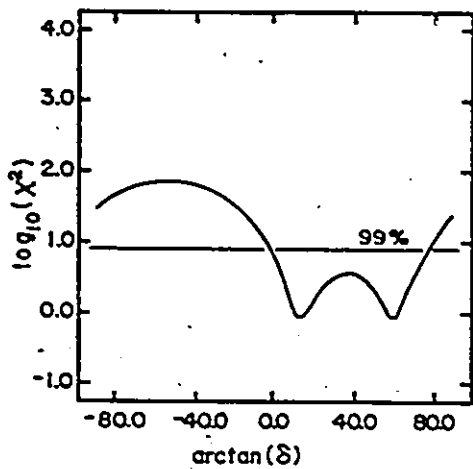
^{32}P levels

Before presenting the results for ^{34}P , we examine the correlations obtained for two transitions in ^{32}P between levels of known spin but unknown mixing ratio. Although the quality of the statistics was poor and data could be obtained only for the $m=0$ correlation, these transitions provide a further check on the total efficiency correction for two different γ -ray energies. The $\chi^2(\delta)$ curves and the correlation corresponding to the minimum chi-square for both transitions are shown in Figure 4.10. Although only one curve is shown here, $\chi^2(\delta)$ was calculated for different values of the population parameters. For both transitions, the lower particle yield for $m=1$ compared with $m=0$ deuterons indicated a strong population of the $m=0$ substate for the correlation

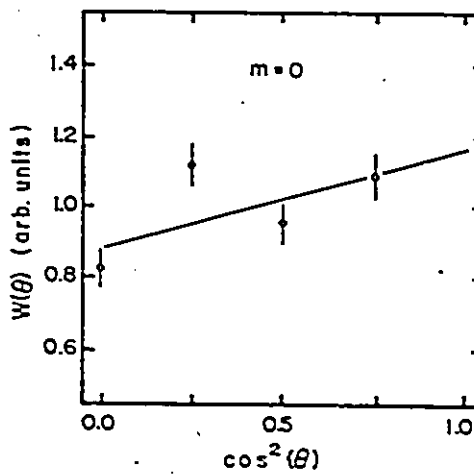
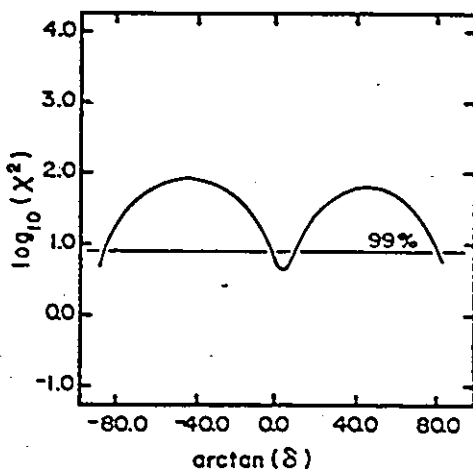
Figure 4.10

Chi-square versus mixing ratio plot for measured correlations for two known spin states in ^{32}P . The solid curves through the data correspond to the minimum chi-square. The $m=1$ deuteron correlations could not be extracted.

^{32}P 1.15 \rightarrow 0.08 MeV ($1^+ \rightarrow 2^+$)



^{32}P 2.74 \rightarrow 0.00 MeV ($1^+ \rightarrow 1^+$)



20

measured with $m=0$ deuterons. The values considered were $P(m=0) = .8 \pm .1$. The mixing ratio values corresponding to the minimum χ^2 for the different curves varied only slightly and the error quoted on δ includes this variation as well as a standard deviation error. For the first transition, 1.15 \rightarrow 0.08 MeV, $1^+ \rightarrow 2^+$, the E2/M1 mixing ratio values are $\delta = .23 + .30 / - .11$ and $\delta = 1.7 + .5 / - .7$. The correlation for the other transition, 2.74 \rightarrow 0.0 MeV, $1^+ \rightarrow 1^+$ yields an E2/M1 mixing ratio $1/\delta = 0.0 \pm 0.1$ or $w = 0.07 \pm .10$. These values for the mixing ratio are consistent with empirical values for transition rates in this mass region (En79).

^{34}P levels

The rest of this section is devoted to a discussion of the angular correlation results for decays in ^{34}P which were resolvable from other γ -ray transitions and which had better than 20% statistical uncertainty.

0.43 MeV level

The alpha particle peak corresponding to this excited state was well resolved in the particle spectrum (see Fig. 4.9) and no known contaminant peaks coincided with the window. The initial spin values which need to be considered in analyzing the angular correlation for the transition to the 1^+ ground state can be restricted to 1^- and 2^+ . These restrictions stem from the natural parity

assignment for this level and the recommended upper limits (RUL) from (En79), which are based on observed transition strengths in the mass region A=6-44. Further restrictions can be placed on the mixing ratio $\delta(M2/E1)$ for a $1^- \rightarrow 1^+$ transition. The restriction on the mean lifetime of the level, imposed by the coincidence resolving time of 50 nsec, leads to the inequality

$$\frac{\pi}{\Gamma(E1) + \Gamma(M2)} < 50 \text{ nsec}$$

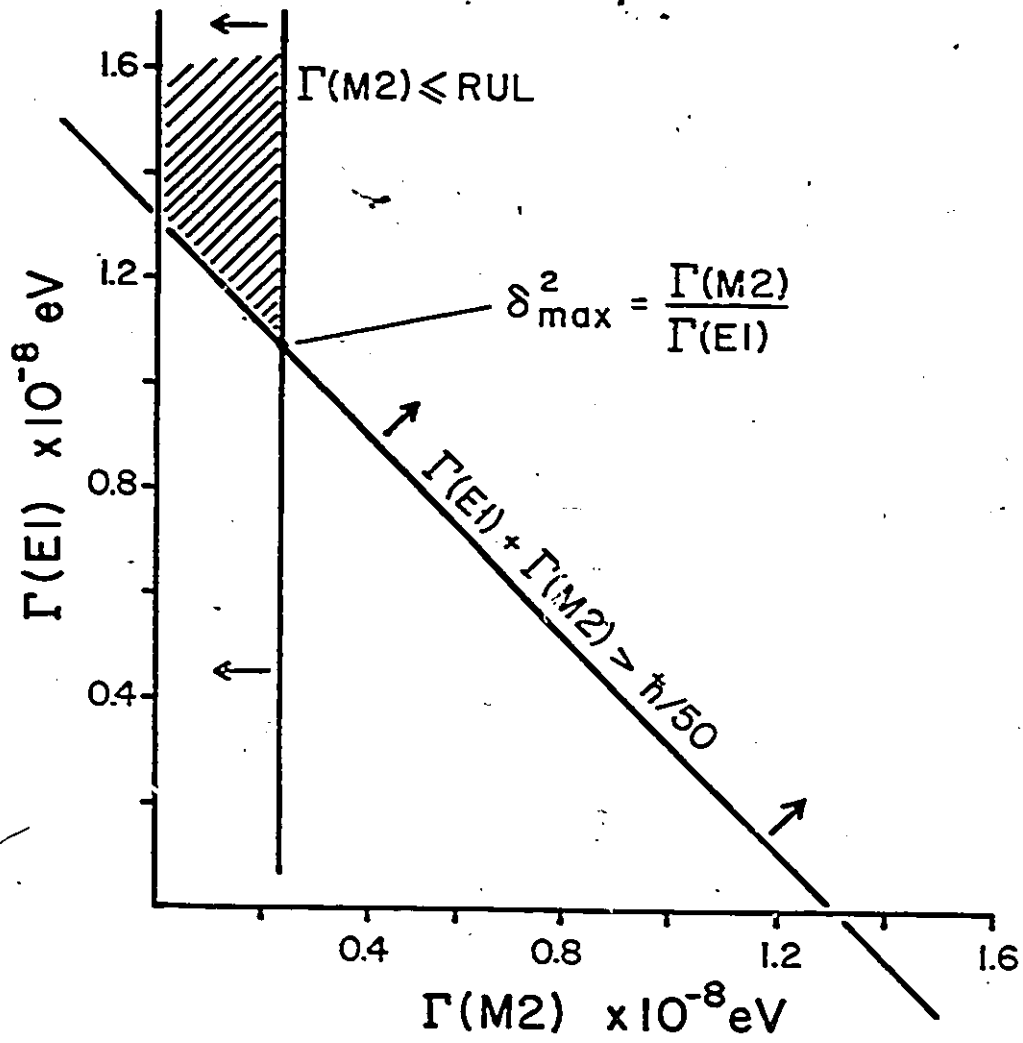
Using the RUL for M2 transitions yields the inequality $\Gamma(M2) < \text{RUL}$. These two relations are plotted in Figure 4.11 for different strengths $\Gamma(E1)$ and $\Gamma(M2)$. The cross-hatched region corresponds to allowed values for the strengths satisfying both the above conditions. Note that the RUL for $\Gamma(E1)$ is not shown since it lies well outside the range of the ordinate for the graph. The intersection of these two lines yields the maximum value of the mixing ratio and is given by the expression,

$$\delta^2 = \frac{\text{RUL}(M2)}{[(R/50) - \text{RUL}(M2)]}$$

Using the Weisskopf estimate (Γ_w) for the $\text{RUL}(M2)$, which is lower than the value of $3.0\Gamma_w$ recommended by Endt (En79) but still in agreement with large empirical values for M2 strengths in this mass region, the maximum admixture of M2 possible for this transition is 22%. This corresponds to a

Figure 4.11

Graph of the constraints on transition strengths $\Gamma(E1)$ and $\Gamma(M2)$ for an 0.43 MeV transition in an A=34 nucleus. The shaded region corresponds to allowed values, and the intersection point yields the maximum allowed mixing ratio.



mixing ratio of $\arctan(25^\circ)$.

Owing to the natural parity character of the initial state, only the $m=1$ correlation was measured and the substate population for the correlation was assumed to be almost entirely $m=1$ substate. The values of chi-square from the least-squares analysis are plotted, for each spin value, in Figure 4.12. The corresponding best-fit correlations are plotted with the measured data on the right hand side of the figure. The chi-square for the $J^\pi=1^-$ correlation is just within the 99% confidence level (C.L.) for $\arctan(\delta) = 25^\circ$ and is outside this C.L. for smaller values of delta. This limit on δ is extreme since it would entail the largest $r(M2)$ observed and a level mean life just within the coincidence resolving time. A more realistic value for δ is expected to be much smaller than this limit, thus producing a fit to the data outside the acceptable 99% C.L.. Therefore, on grounds that a 22% admixture of $M2$ is highly unlikely, the spin 1^- can be rejected and a unique spin $J^\pi=2^+$ can be assigned to the level at 0.43 MeV. The values of the $E2/M1$ mixing ratio corresponding to the minima in χ^2 are $\delta = 1/(-.01 \pm .08)$ or $\delta = -.52 \pm .10$, where again the error represents the range in delta for which $\chi^2 < \chi^2_{\min} + 1$.

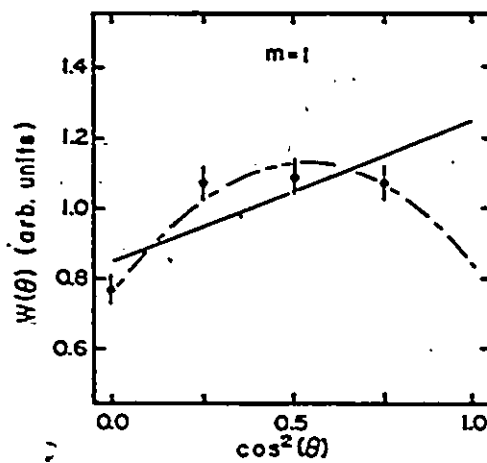
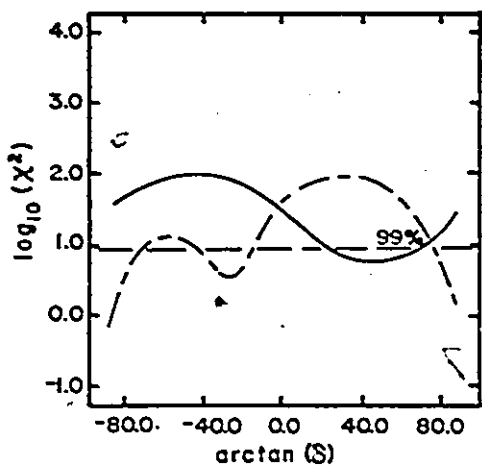
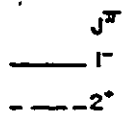
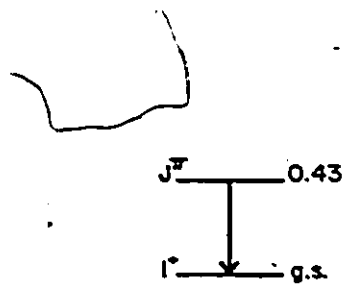
1.61 MeV level

The window set on the α -particle peak associated with this level is indicated in Figure 4.9. The presence of



Figure 4.12

$\chi^2(\delta)$ curves for different initial spin values J^π , for the transition 0.43 MeV \rightarrow g.s. (1^+). Only the $m=1$ correlation is included since the 0.43 MeV level has natural parity. The correlation curves drawn with the data correspond to the minimum chi-square for each spin value.



the 1.75 MeV, ^{32}P level in the high-energy portion of the window was of concern since its decay to the 0.08 MeV level yields a 1670 keV γ -ray which would have been unresolved from the 1610 keV γ -ray from the decay of the 1.61 MeV level to the ground state. The 1670 keV line had already been observed with the high resolution Ge detector (see Fig. 4.1). According to kinematic calculations, which allowed for the broad angular range of the particle detector, the alpha particles from the two levels were separated by approximately 100 keV. Therefore, by sorting with particle windows of different widths and comparing the yield of the 1610 keV γ -ray to that of the 1180 keV γ -ray, it was possible to determine the widest possible window which still excluded the ^{32}P level.

The tensor analyzing power measurements resulted in an unnatural parity assignment for this level. This result along with lifetime considerations for the observed decays to the 1^+ ground state and the 2^+ excited state allow for the restriction of possible spin values for the 1.61 MeV level to 1^+ , 2^- and 3^+ .

Before the correlation data is examined the problem of coincidence summing in the large NaI detectors needs to be addressed. This effect is important in the decay of the 1.61 MeV level since it involves a cascade of γ -rays. Assuming an isotropic angular distribution, the probability of detecting a single γ -ray in a detector is proportional to

the fraction of the total solid angle subtended by the detector. And, the probability of detecting two successive γ -rays in the same detector is proportional to the square of this ratio. In our experiment each NaI detector spanned 2.3% of the total solid angle. Taking into account the branching ratio, measured by Nathan and Alburger (NA77),

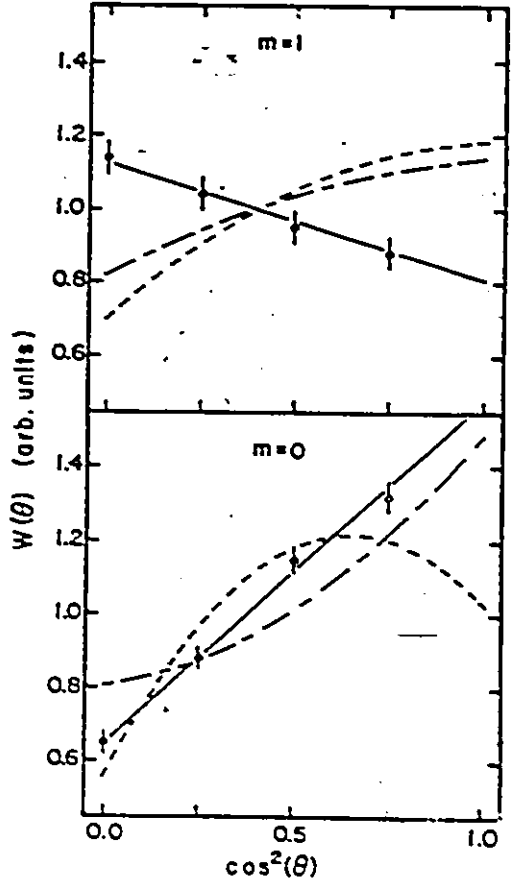
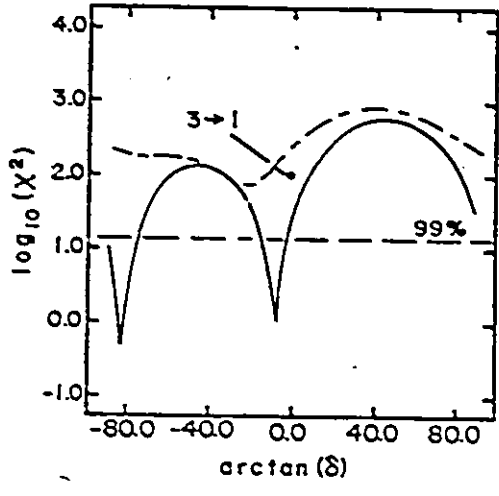
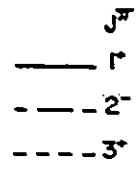
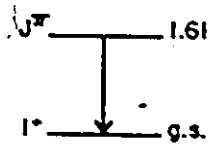
$$\frac{r(1.61 \rightarrow .43 \rightarrow g.s.)}{r(1.61 \rightarrow g.s.)} = 1.8 \pm 0.3,$$

the fraction of 1610 keV γ -rays measured which resulted from the sum of the cascade γ -rays was approximately 5%. As seen in Figures 4.14 and 4.15 the angular distributions of the two cascade γ -rays, 1180 and 430 keV, are nearly isotropic. Although the correlations for the 1610 keV line are not isotropic the correction is within the statistical uncertainty of the data and its effect can be safely neglected.

Both $m=0$ and $m=1$ correlations for the decay to the 1^+ ground state, displayed in Figure 4.13, exhibit a marked anisotropy. The curves drawn with the data correspond to the best-fit correlation for each initial spin value. The population parameters for the initial state, determined from the ratio of the cross-sections for $m=0$ and $m=1$ using the equations described in chapter one, were for $m=0$, $P(m=0)=.80$ and for $m=1$, $P(m=1)=.65$. Variations in these values by about 10% did not yield any appreciable difference in the minimum $\chi^2(\delta)$ for any initial spin value.

Figure 4.13

The left side of the figure is a plot of chi-square versus mixing ratio, for the combined $m=0$ and $m=1$ correlations, for different initial spin values. The curves plotted with the measured correlations, on the right side, correspond to the minimum χ^2 for each spin value.



The $\chi^2(\delta)$ curve for only one value of the population parameter is shown in Figure 4.13 for each spin value. As evidenced by the dotted-dashed line drawn through the data, the initial spin of 2^- does not successfully reproduce the data for either correlation. The dashed line corresponding to a pure E2, $3^+ \rightarrow 1^+$, transition yields an acceptable fit for the $m=0$ data but fails completely in fitting the $m=1$ correlation. Only the $1^+ \rightarrow 1^+$ transition succeeds in reproducing both observed correlations. Thus, the 1.61 MeV level can be assigned a spin 1^+ with a mixing ratio for the mixed E2/M1 transition to the ground state of $\delta = -0.13 \pm 0.06$ or $\delta = -1/(0.13 \pm 0.06)$.

The ratio of the Weisskopf single-particle estimate for the transition rate of a 1.61 MeV γ -ray in an A=34 nucleus is,

$$\frac{\Gamma_w(E2)}{\Gamma_w(M1)} = 6.7 \times 10^{-4}$$

According to recent compilations (En79) observed E2 strengths are in the range of $1 - 10 \times \Gamma_w(E2)$ and M1 observed strengths lie between $1 - 10^{-2} \times \Gamma_w(M1)$. Hence, the largest typical value expected for a mixing ratio for this transition is

$$10^3 \left[\frac{\Gamma_w(E2)}{\Gamma_w(M1)} \right] = 1.$$

Although the observed range $\delta = -1/(0.13 \pm 0.06)$ is higher

than the above ratio by an order of magnitude, it cannot be excluded since the ratio is for typical transition strengths and weaker M1 transitions, with a lifetime within 50 nsec, are possible.

It is worthwhile noting that the $m=1$, and not the $m=0$, correlation is important in differentiating between the initial spin values 1^+ and 3^+ .¹⁾ Also noteworthy is the isotropic distribution one obtains when the $m=0$ and the $m=1$ correlations are summed together. This is just the angular correlation expected from a spin $J_1=1$ state with equal population of all three magnetic substates.

Before going on to the next excited state in ^{34}P there are two other transitions whose correlations can be used to provide a check on the spin assignments for the first two excited states. The first is the decay $1.61 \rightarrow 0.43$ MeV, $1^+ \rightarrow 2^+$. The measured correlations and the best-fit curves, assuming the same population parameters as above for the 1.61 MeV level, are illustrated in Figure 4.14. The oscillatory behaviour of the $m=1$ correlation is unphysical; it is possibly a result of uncertainties in the background subtraction which have not been included in the plotted error bars. Nevertheless, a chi-square within the 99% confidence level is obtained with an E2/M1 mixing ratio in

1) This remark depends on the number of, and angle at which, the correlation points are measured. An additional measurement at 0° , with reasonable precision, would have allowed differentiation between $J=1$ and $J=3$ correlations.

the range $\delta = 0.96 \pm 0.64$.

The other transition which is useful in verifying the spin assignments is the cascade [1.61 \rightarrow] 0.43 \rightarrow g.s. where the square brackets signify that the first transition is unobserved. The correlation function for such a cascade is given by equation 1.17 presented in chapter one. Two points should be noted in comparing this correlation function with that of equation 4.1: (1) the statistical tensor coefficients are those for the population of the initial level in the cascade, even though the transition from this level is unobserved; (2) the mixing ratio for the unobserved transition, δ_{12} , is an additional parameter.

The $\chi^2(\delta)$ curves of the previous transition, 1.61 \rightarrow 0.43 MeV, shown in Figure 4.14 restricted the possible range of mixing ratio to $\delta_{12} = 0.96 \pm 0.64$. The correlation function was calculated for different δ_{12} values in this range and the resulting $\chi^2(\delta_{23})$ curves are included in Figure 4.15. The best-fit correlation curve corresponding to the minimum chi-square is drawn with the data on the right side of the figure. The ranges for the mixing ratio δ_{23} determined from the single transition correlation (see Figure 4.12) are indicated by the arrows above the horizontal axis in the $\chi^2(\delta_{23})$ plot. From this plot it can be seen that a chi-square below the 99% confidence limit was obtained for all curves overlapping with at least one of the delineated regions of δ_{23} . The restrictions on the combina-

Figure 4.14

$\chi^2(\delta)$ curve and measured correlations for the transition 1.61 \rightarrow 0.43 MeV, $1^+ \rightarrow 2^+$. The oscillations outside one standard deviation in the $m=1$ correlation reflect the overestimation of the experimental uncertainty from not considering any error in background subtraction.

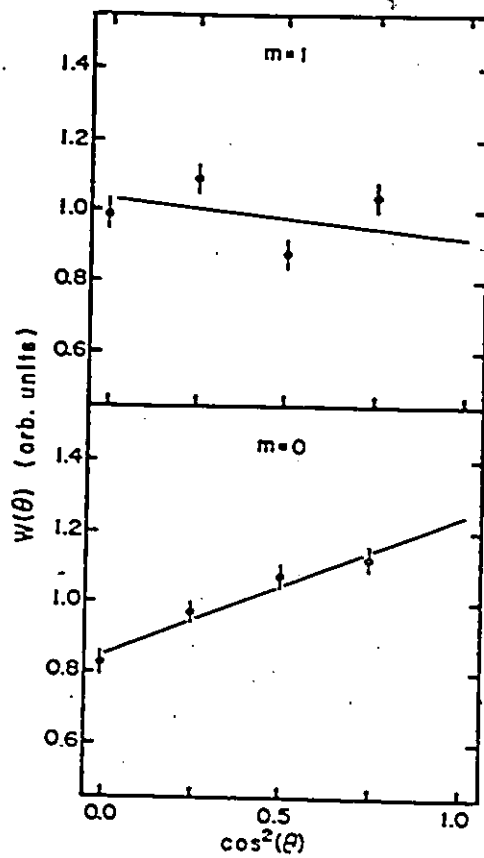
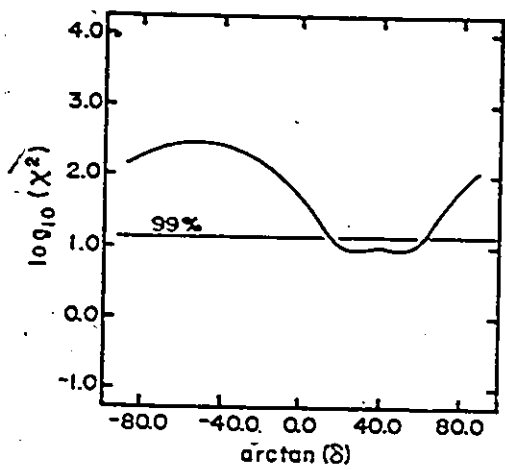
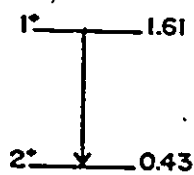
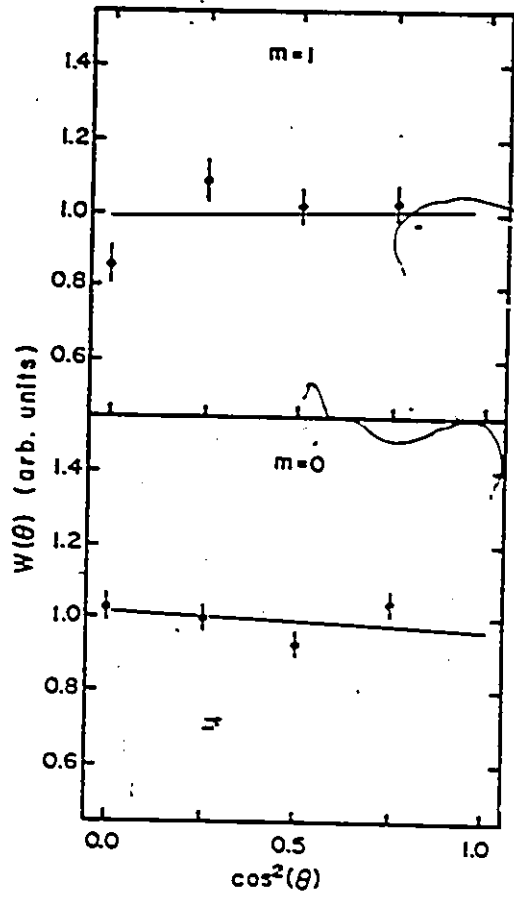
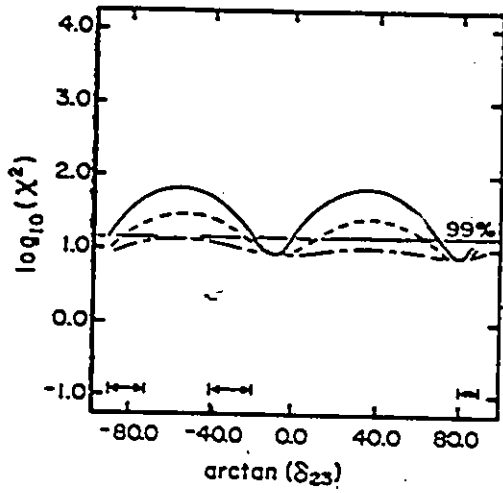
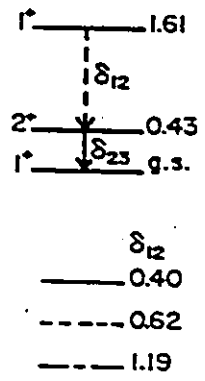


Figure 4.15

$\chi^2(\delta_{23})$ curve and measured angular correlations for the transition 0.43 MeV \rightarrow g.s. from the decay cascade of the 1.61 MeV level. The 1.61 \rightarrow 0.43 MeV transition is unobserved and $\chi^2(\delta_{23})$ is plotted for different values of the mixing ratio δ_{12} in the restricted range for this transition (see Fig. 4.14). The arrows above the abscissa in the $\chi^2(\delta_{23})$ plot indicate those regions of δ_{23} which resulted in an acceptable fit for the single transition (see Fig. 4.12).



tions of δ_{12} and δ_{23} values are listed in Table 4.6.

Therefore both cascades confirm the spin assignments for the 0.43 and 1.61 MeV levels. Furthermore, the latter correlation provides an added restriction on the mixing ratio for the 1.61 \rightarrow 0.43 MeV transition depending on the mixing ratio for the 0.43 \rightarrow g.s. transition.

2.23 MeV level

Although it had not been possible to resolve the 2.23 MeV ^{34}P level from the 2.74 MeV ^{32}P level in the particle spectrum for the Ge detector experiment, it was possible to do so in this experiment since the angular range of the detector was greatly reduced compared to the earlier experiment. Exclusion of the ^{32}P 2.74 MeV state from the 2.23 MeV particle window was achieved by setting the upper bound of the window progressively closer to the peak until the gamma-ray projection contained no sign of the 2.74 MeV \rightarrow g.s. decay. In this way, a clean projection for the 2.23 MeV \rightarrow g.s. decay was obtained without any interference from the 2.74 \rightarrow 0.51 MeV decay in ^{32}P . Other γ -rays also observed in this projection were associated with the transitions 2.23 \rightarrow 0.43 MeV and 2.31 \rightarrow 0.43 MeV, although their intensity was too low to allow reliable measurement.

The statistics for the transition 2.23 MeV \rightarrow g.s., as evidenced by the large error bars in the correlation of Figure 4.16, were not as good as for the lower energy

Table 4.6 Mixing ratio combinations for
 δ_{12} (1.61- \rightarrow .43) and δ_{23} (.43- \rightarrow g.s.)

δ_{12} (E2/M1)	δ_{23} (E2/M1)
$.93 \pm .26$	$-.52 \pm .10$
$.96 \pm .64$	$1/(-.01 \pm .08)$

particle windows. Data for the $m=1$ correlation were not extracted due to the poor NaI detector resolution which was a consequence of the higher singles count rate for $m=1$ compared with $m=0$ deuterons. The $\chi^2(\delta)$ curves for the fit of the calculated correlations with the $m=0$ data are shown in the figure for the different initial spin values, 1^+ and 2^- . Both clearly fail to agree with the data for any value of the mixing ratio. This is also clear from the best-fit correlations drawn with the data. The correlation for a pure E2 transition from a spin 3^+ state best reproduces the data although the resultant $\chi^2 = 12.2$ is not quite within the 99% confidence limit. It was possible to improve on this fit by allowing a small admixture of M3 strength ($|\delta(M3/E2)| < 0.15$), which is still within the recommended upper limits, $RUL(M3) = 10.0 \Gamma_w(M3)$, (En79). Despite this improved agreement, the occurrence of 15% admixture of M3 is highly unlikely and the spin 3^+ is included in parenthesis indicating the tentativeness of this value.

4.74 MeV level

The true γ -ray projection from the particle window set on the 4.74 MeV level in ^{34}P is shown in Figure 4.17. This spectrum is included here to show the identification of all the prominent observed γ -rays. The photo peak and first escape peak for the 4.74 \rightarrow 0.43 MeV transition are labelled in the figure. The sum of the two peak intensities was used

Figure 4.16

$\chi^2(\delta)$ plot and measured angular correlations for the transition 2.23 MeV \rightarrow g.s.. The poor NaI detector resolution for the $m=1$ data made it impossible to extract intensities for this transition.

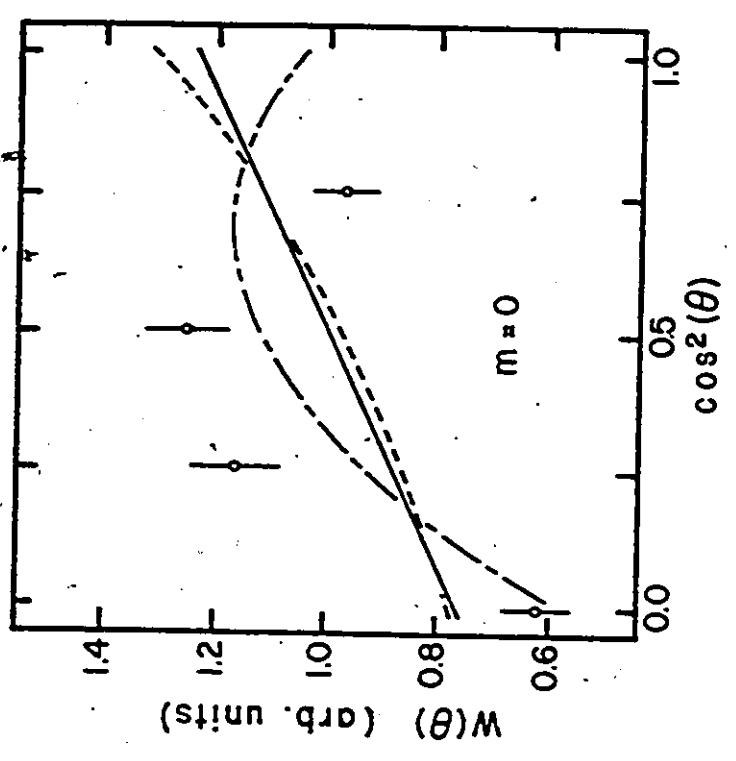
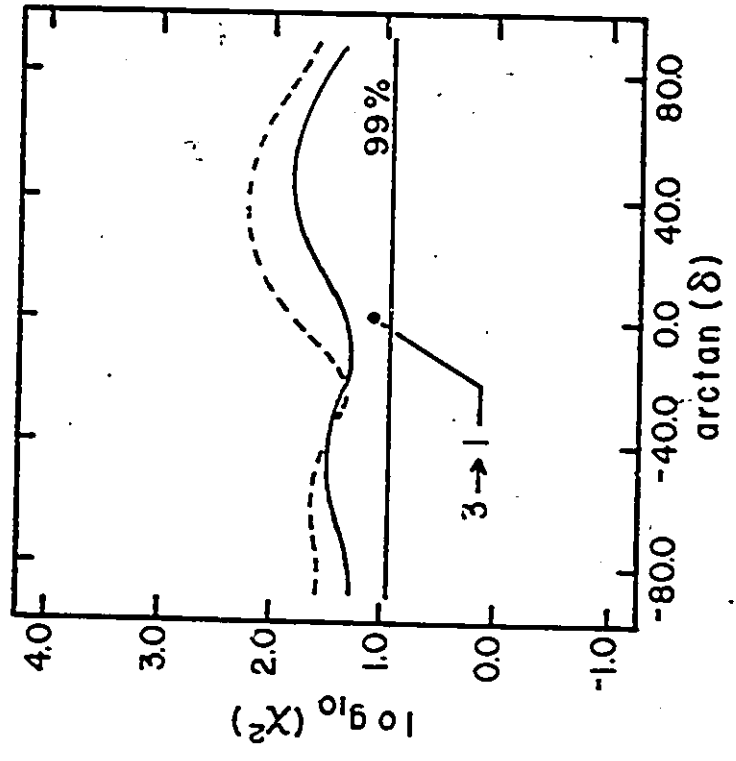
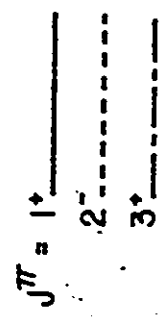
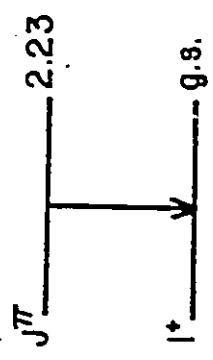
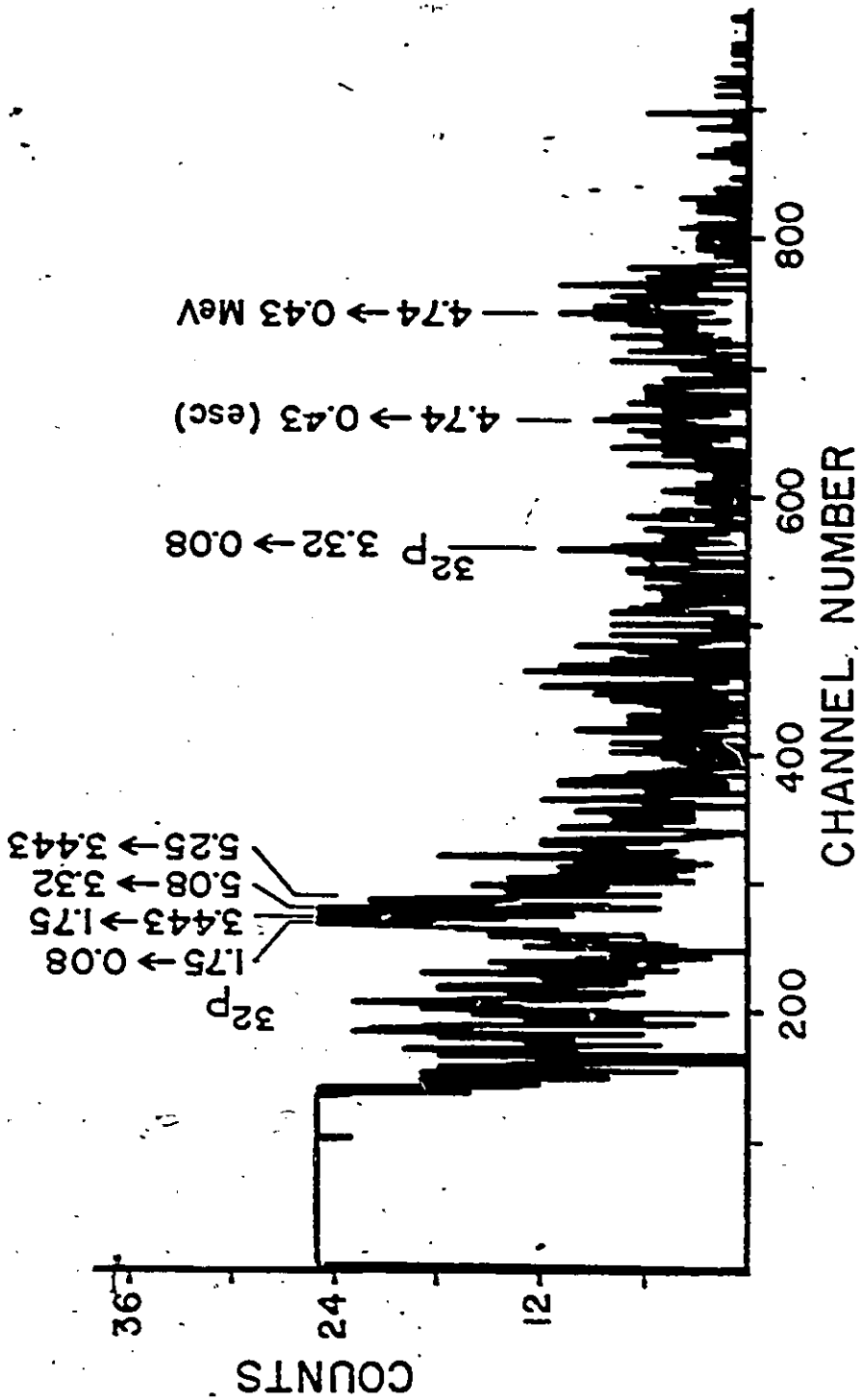


Figure 4.17

True coincidence gamma-ray projection from the alpha particle window for the 4.74 MeV level. The strong peaks in the spectrum are shown labelled. The first escape peak for the 4.31 MeV gamma-ray is slightly weaker than the photopeak while the second escape peak is not populated very strongly. This is consistent with other measured NaI efficiencies for high energy gamma-rays (BL64).

**γ-ray Projection For The
4.74 MeV Level**



for the angular correlations for this transition. Other strong γ -rays belong to transitions in ^{32}P and are labelled accordingly.

The only other excited state included in the particle window, which could have associated with its decay a γ -ray in the energy range 4.0 to 4.5 MeV, is the 9.63 MeV, 3^- level in ^{12}C . However this state is unstable against α -decay and the measured ratio of the radiation width to total decay width for this state is

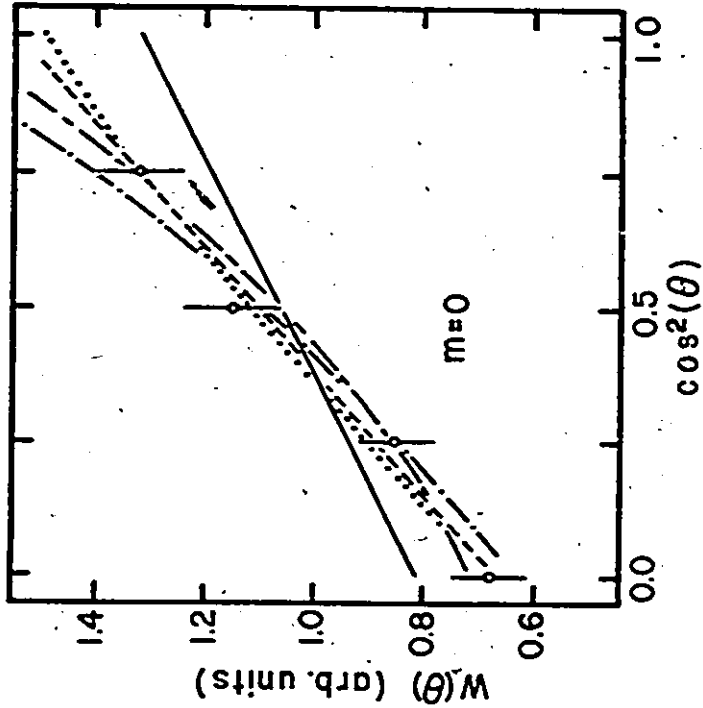
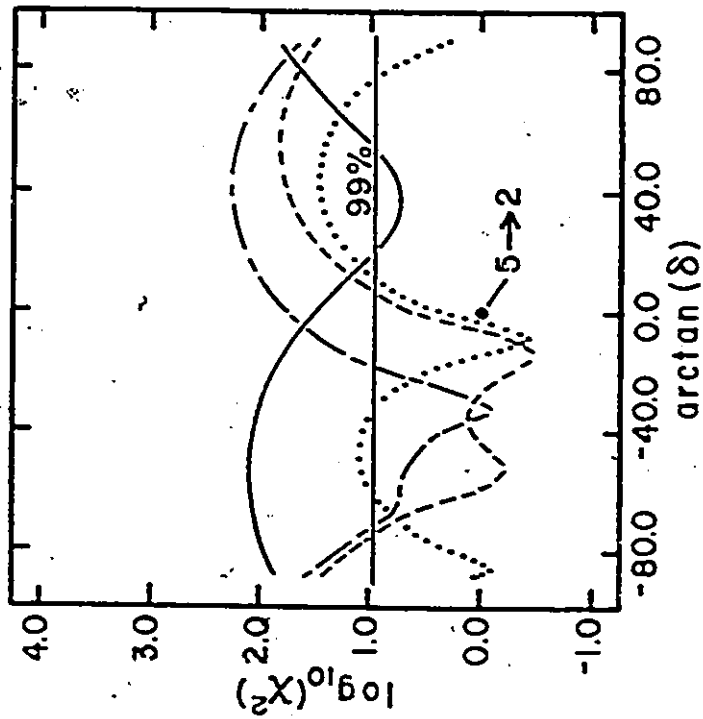
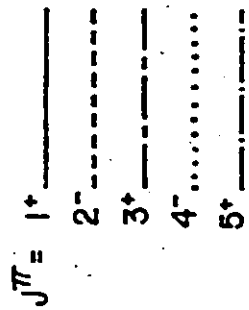
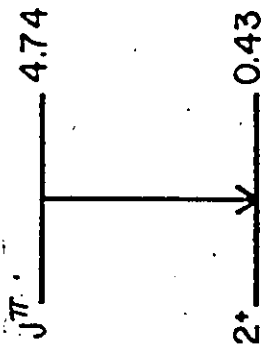
$$\frac{\Gamma_{\text{rad}}}{\Gamma} < 4.1 \times 10^{-7}$$

Assuming a cross-section to this level comparable to that for the first excited state in ^{12}C , the gamma decay strength should be negligible. Therefore the total intensity for the two broad humps in the γ -ray projection can be assigned entirely to the decay $4.74 \rightarrow 0.43$ MeV.

The spectrum displayed in Figure 4.17 is the projection obtained with $m=0$ deuterons. The poorer resolution of the $m=1$ projection made it impossible to extract intensities reliably. The best fit correlations for the transition to the 0.43 MeV (2^+) state, corresponding to the different allowed unnatural parity J^π values are shown in Figure 4.18. Eventhough the $J^\pi=1^+$ correlation does not reproduce the data as well as the other J^π values, it cannot be eliminated at the 99% confidence level. Therefore no

Figure 4.18

Calculated $\chi^2(\delta)$ curves for the $m=0$ correlation data for the transition $4.74 \rightarrow 0.43$ MeV. The curves plotted for each J^π value with the data correspond to the minimum chi-square.



restriction on the spin assignment is possible.

Other levels

Several factors contributed to our inability to extract angular correlation data for the decay of other levels in ^{34}P . Often the decay was too weak to allow for an accurate measurement of the peak intensity with background subtraction. This was the case for the decay of the 2.68 and the 4.31 MeV levels. In other cases the transition in ^{34}P conflicted with a transition in ^{32}P . An example of this was the decay 2.31 MeV \rightarrow g.s. in ^{34}P coinciding, within 80 keV, with both the decay 2.74 \rightarrow 0.51 MeV and the first escape peak from the decay 2.74 MeV \rightarrow g.s. in ^{32}P . For all of these levels, spin-parity assignments were made on the basis of the T_{20} analyzing power measurements and transition strength arguments for the observed decays from the high resolution germanium detector experiment.

4.3 SUMMARY

The spin and parity assignments for the levels in ^{34}P resulting from the analysis of the correlation data are summarized in Table 4.7. Also included in the table are the restrictions on spin assignments of other levels for which correlation data was not available. In those cases the decays observed with the high resolution germanium detector

Table 4.7 J^{π} assignments in ^{34}P

E^* (MeV)	J^{π}
0.00	1^+
0.43	2^+
1.61	1^+
2.23	(3^+)
2.31	$(1^+, 2^-, 3^+, 4^-)$
2.68	$(1^+, 2^-, 3^+)$
4.31	$(\bar{1}^+, 2^-, 3^+, 4^-)$
4.74	$(1^+, 2^-, 3^+, 4^-, 5^+)$

in conjunction with transition rate considerations led to the restrictions on the spin values.

In summary, the spins of the first two excited states, hitherto unknown, have been uniquely determined as 2^+ and 1^+ , respectively. The level at 2.23 MeV is most likely to have a spin of 3^+ , although the χ^2 for the fit to the measured correlation, assuming a negligible amount of M3 admixture, was slightly larger than the 99% confidence limit. The quality of the data, limited largely by the low count rate and the resolution of the NaI detectors, precluded the assignment of unique spin values for any of the other levels.

CHAPTER 5: SHELL MODEL CALCULATIONS

In this chapter, results of the shell model calculations are presented and compared with experimental results for ^{34}P . A brief outline of the relevant aspects of shell-model theory as well as a description of the shell-model code OXBASH used for the present calculations comprise the first section. Comparison of the calculation results with experimental values is done in two parts; section two deals with positive parity states while the negative parity states are dealt with in the third section.

5.1 INTRODUCTION

An understanding of the structure of the nucleus requires the solution of the many-body Schroedinger equation,

$$H\psi = E\psi \quad (5.1)$$

where the eigenvalue, E , corresponds to the excitation energy and the eigenstate, ψ , is the wavefunction associated with that energy level. Assuming a two-body nucleon-nucleon

interaction the Hamiltonian for A nucleons has the form

$$H = \sum_{i=1}^A T(i) + \sum_{1=i<j}^A W(i,j) . \quad (5.2)$$

An exact solution of this equation is not possible and the simplification is made that the overall effect of the sum of the two-body interaction for all nucleons can be approximated by an average potential. The expression for the Hamiltonian in equation 5.2 can be rewritten as,

$$H = \sum_{i=1}^A \{T(i) + U(i)\} + \left\{ \sum_{1=i<j}^A W(i,j) - \sum_{i=1}^A U(i) \right\} . \quad (5.3)$$

The term in the second brackets is called the residual interaction and, assuming the validity of the above approximation, this term will be small and can thus be treated using perturbation theory.

It can be shown, in general, using perturbation theory that the residual interaction for n valence nucleons outside an inert closed core of A-n nucleons can be expressed as a sum of two-body matrix elements, TBME, (BG77). The Hamiltonian is written as,

$$H = \sum_{i=1}^n \epsilon_i + \sum_{\substack{i,j, \\ k,l}} \langle (\phi_i \phi_j)_{JT} | O^{2b} | (\phi_k \phi_l)_{JT} \rangle \quad (5.4)$$

where ϵ_i are the single particle energies (SPE) for the active orbitals and the ϕ_i in the TBME are single particle wavefunctions. Therefore the essential ingredients in a

shell-model calculation are the ϕ_i and the interaction which is specified by single particle energies and the two-body matrix elements. Harmonic oscillator wavefunctions are usually chosen for the single particle states because of their mathematical simplicity.

Once the configuration space is defined the energy levels are obtained by solving the eigenvalue problem using matrix diagonalization in the chosen set of basis states. There are two methods for choosing a basis. One method is to form states with good J and T ; however this requires extensive tables of coefficients of fractional parentage in order to do further calculations in this basis. The other method circumvents this large requirement of computer memory by using the basis states in an m -scheme representation and translating the effective interaction into this basis. This latter method exploits the power of binary computation since the value of a single bit, 1 or 0, is used to denote the presence or absence of a particle in a given orbit.

The shell-model code OXBASH (BE84) used for the calculations presented below uses the m -scheme representation which greatly reduces calculation time. The problem of diagonalizing the large matrices which often result is handled using the LANCZOS method. This method calculates the lower energy eigenvalues and eigenstates without diagonalizing the entire matrix. More information about the structure of this code is available in the lucid and

thorough documentation available from the authors.

An extensive treatment of effective interactions is presented by Brussard and Glaudemans (BG77), and included here is a brief summary in order to provide a framework for later discussions of the effective interactions used in the shell model calculations for ^{34}P . The two-body matrix elements and single-particle energies which constitute the effective nuclear interaction for the chosen configuration space can be determined in several ways. The empirical method assumes that the TBME are constant over the mass region and determines their value by doing a least-squares fit to the low-lying energy levels with known J and T in nuclei included in the region. In this method the analytical form of the interaction need never be specified. At the other extreme, the TBME are calculated starting with the nucleon-nucleon interaction obtained by fitting phase-shifts from scattering data and properties of the deuteron wavefunction. Because the shell model calculation is eventually carried out in a truncated basis, a realistic interaction of this kind does not yield good agreement with spectroscopic data. Perturbation theory can be used to take account of interactions outside the configuration space, however this often proves a complex and difficult task plagued with problems of convergence. A compromise to the above approaches is to calculate the TBME from a schematic nucleon-nucleon interaction such as an attractive central

potential plus exchange potentials. This approach is particularly useful for large configuration space calculations. A widely used schematic interaction, because of its mathematical simplicity, is the surface-delta interaction (SDI).

The basic test of the validity of the shell model calculation is to determine its accuracy in the prediction of observed level schemes for nuclei in the region of applicability. A more stringent test, since it is more sensitive to the various components of the wavefunctions, is the prediction of measurable quantities such as the spectroscopic factors, electromagnetic transition strengths and β -decay strengths. Spectroscopic factors will not be dealt with here as there are no such data in ^{34}P available in the present literature.

The electromagnetic and β -decay transition operators are single particle operators. The general expression for such an operator, using the creation and annihilation operators of second quantization, has the form

$$Q_{\mu}^{\lambda} = \sum_{j_1 j_2 t_3} \langle \phi(j_2 t_3) | q^{\lambda} | \phi(j_1 t_3) \rangle \sum_{m_1 m_2} \{ (j_1 m_1 \lambda \mu | j_2 m_2) \times a(j_2 m_2 t_3)^{\dagger} a(j_1 m_1 t_3) \} \quad (5.5)$$

The first factor on the right is called the reduced single-particle matrix element (RSPME) and includes the quantities specific to that operator. The second factor, a sum of pro-

ducts of Clebsch-Gordan coefficients and, creation and annihilation operators, contains the details of the coupling of single-particle wavefunctions. This latter sum can be written as a coupling of the creation and annihilation operators to a final value of λ , to yield a final expression for the reduced matrix element for the operator Q^λ between two nuclear states given by:

$$\langle \Psi(J_f T_3) | Q^\lambda | \Psi(J_i T_3) \rangle = \sum_{j_1 j_2 t_3} \left(\frac{2j_2+1}{2\lambda+1} \right)^{1/2} \times \\ \langle \phi(j_2 t_3) | Q^\lambda | \phi(j_1 t_3) \rangle \langle \Psi(J_f T_3) | (a^\dagger \times \bar{a})^\lambda | \Psi(J_i T_3) \rangle \quad (5.6)$$

where the arguments for the creation and annihilation operators have been suppressed. The first matrix element is the RSPME and the second defines the one-body transition density (OBTD). All single-particle-operator matrix elements can be expressed in this form. The OBTD are common to all operators and are calculated in the shell-model code once the eigenfunctions for the different nuclear states have been determined. The RSPME are calculated a priori from the known form of the real operator interaction. However, often an effective interaction for the operator must be introduced to compensate for the effect of the truncated shell model space and the difference between the bound and free nucleon form of the operator. Similar methods to ones outlined above for the TBME are used to obtain the RSPME from an

effective-operator interaction.

5.2 POSITIVE PARITY STATES

In the simplest shell-model description of ${}_{15}^{34}\text{P}$ there are eighteen nucleons in the sd-shell outside a closed ${}_{8}^{16}\text{O}$ core. With space for a total of 24 nucleons in the sd shell, the low-lying positive parity states are expected to correspond to excitations within this shell. The configuration space used in the calculation consisted of the three orbitals, $1d_{5/2}$, $2s_{1/2}$ and $1d_{3/2}$, with no restrictions on the distribution of the 18 valence nucleons. The largest basis dimension was 232 for $J^{\pi}=3^{+}$ states and the cpu time required for the calculation was on the order of one hour.

The single-particle energies for the three orbitals plus the 63 two-body matrix elements employed in the calculation were those of Wildenthal's universal sd-shell interaction (Wi82). The TBME and SPE were obtained from a realistic effective interaction based on the Hamada-Johnston potential for the nucleon-nucleon interaction after which, selected two-body matrix elements were adjusted to obtain a best fit between the measured excitation energies of known J^{π} levels in the A=17-39 mass region and the corresponding shell-model eigenvalues. Incorporated into this empirical calculation of the matrix elements was a mass dependence of

the form $(18/A)^{0.3}$ (PW72), (Wi82). Although the excitation energies of the first three excited states in ^{34}P were known at the time this interaction was derived, these states were not used since their spins and parities remained unknown.

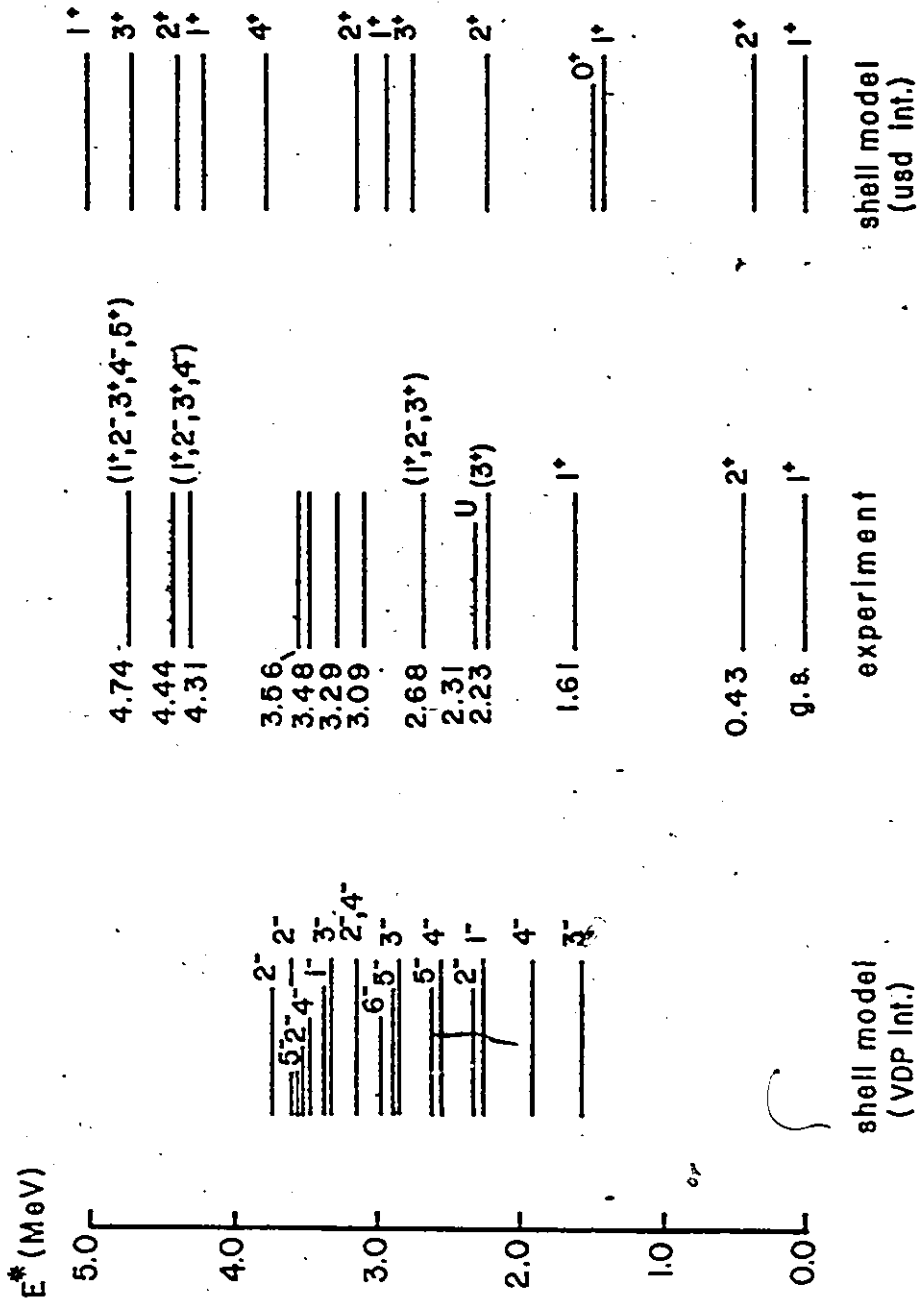
The level scheme for ^{34}P obtained with this interaction as well as that resulting from the angular correlation experiments are illustrated in Figure 5.1. The dominant configuration in the ground state and first excited state wavefunctions is $[(1d_{5/2})_0^{12} (2s_{1/2})_{1/2}^3 (1d_{3/2})_{3/2}^3]_{1^+, 2^+}$ with probability amplitudes of 73% and 78%, respectively. The 1^+ state corresponding to the observed level at 1.61 MeV has a probability amplitude of 55% for the configuration $[(1d_{5/2})_0^{12} (2s_{1/2})_{0(1)}^2 (1d_{3/2})_{1(0)}^4]_{1^+}$, where the odd proton is in either the $1d_{3/2}$ or $2s_{1/2}$ subshell. The calculation yields excellent agreement with the measured levels at low excitation energies, where the average deviation is within 200 keV. It should be noted that population of the 0^+ state predicted at 1.5 MeV is forbidden in the (d, α) reaction at 0° because of conservation of parity and angular momentum. Therefore this state would not have been observed in either the tensor analyzing power or the angular correlation measurements. In the (d, α) scattering experiment away from zero degrees the spectra did not show any evidence for the existence of this state.

A more rigorous test of the shell-model interaction can be obtained from a comparison of the predicted and

Figure 5.1

Level diagrams for ^{34}P . Details of the VDP and usd interactions for the shell model calculations are given in the text. The experimental level scheme comprises the spin and parity assignments from the angular correlation and tensor analyzing power measurements.

34P



measured electromagnetic strengths. Since lifetime measurements were not performed, direct values for these quantities could not be extracted from the experimental results. However, the ratio of the calculated transition strengths can be compared with the experimentally determined mixing-ratio values for transitions between the lowest excited states.

Several studies documented in the literature have investigated the form of the effective operators in the framework of Wildenthal's *usd* shell-model wavefunctions which best reproduce measured multipole moments (up to and including dyotriakontupole) in this mass region. The comprehensive review by Wildenthal and Chung (WC79) summarizes the results from these studies. Values for the single-particle matrix elements constituting the M1 operator were obtained by fitting the 42 measured magnetic moments for *sd*-shell nuclei. In the upper part of the shell, $A=28-39$, the model predictions with this effective operator were within ten percent (i.e. 0.1 nuclear magneton) of the measured values.

The form of the E2 operator used with the Wildenthal wavefunctions has been discussed by Wildenthal and Chung (WC79) for collective E2 transitions and by Brown et al. (BC80) for quadrupole moments in *sd*-shell nuclei. Owing to truncation effects the observed features of electric quadrupole moments and $B(E2)$ strengths across the whole

sd-shell could not be explained using the free proton and neutron charges. The best agreement with the measured values resulted with effective charges of $1.35e$ and $0.35e$ for the proton and neutron, respectively. With these values for the effective charge strong E2 transitions were reproduced to an average deviation of ten percent while the predictions for the much weaker transitions were within fifty percent of the measured values. Quadrupole moments in the mass region $A=17-37$ were also reproduced to within ten percent.

The mixing ratio can be determined from the calculated shell model reduced transition probabilities, $B(L+1)$ and $B(L)$, using the expression:

$$\delta = \pm k \frac{\sqrt{3}}{10} \left[\frac{B(E2)}{B(M1)} \right]^{1/2}, \quad (5.7)$$

where k is the wavenumber of the emitted photon. Thus δ is determined to within a phase factor.

For purposes of comparison the experimental values for the mixing ratio of the transitions from the first and second excited states are listed along with the shell model predictions in Table 5.1. In terms of absolute magnitude, the shell model values generally underestimate the experimental values but give acceptable agreement for all but the transition from the first excited state to the ground state. In that case the predicted ratio is too small by two orders

Table 5.1 Mixing ratio values

$E_i \rightarrow E_f$	experiment $\delta (E2/M1)$	shell model $\delta (E2/M1)$
0.43 \rightarrow g.s.	$1/ (.01 \pm .08)^{a)}$	
	$-.52 \pm .10^{b)}$	1.02×10^{-3}
1.61 \rightarrow g.s.	$-.13 \pm .06$	
	$-1/ (.13 \pm .06)$	2.0×10^{-2}
1.61 \rightarrow 0.43	$.96 \pm .64^{a)}$	
	$.96 \pm .26^{b)}$	1.4×10^{-1}

a), b) matching superscripts indicate the correlation between δ -values obtained from angular correlation data.

of magnitude indicating that either the E2 strength is too small by at most that much or the M1 strength is too large by that same amount. An explanation for this discrepancy may lie with the E2 strength since those E2 transitions with intensities much weaker than the Weisskopf estimates were not well reproduced by the shell model calculation (WC79).

Wildenthal's shell-model wavefunctions for ^{34}p have been verified with results from β -decay measurements. Details of the effective Gamow-Teller operator employed in the calculation are presented in a comprehensive paper on the β -decay of neutron-rich sd-shell nuclei by Wildenthal et al. (WC83). Their prediction of 3.07 seconds for the lifetime of the 0^+ ground state of ^{34}Si , which decays predominantly to the ground state and the 1^+ state at 1.61 MeV via a super-allowed GT transition, is remarkably close to the measured value 2.77 ± 0.20 sec obtained by Nathan and Alburger (NA77) from their delayed β - γ coincidence work. No comparison can be made for the branching ratio to these two states since the β -decay branch to the ground state could not be measured in the experiment.

5.3 NEGATIVE PARITY STATES

The calculation for negative parity states must include configurations with an odd number of p-h excitations

between either the lower energy lp shell and the sd shell or the sd shell and the higher energy fp shell. In the case of the neutron rich ^{34}P , one neutron short of a full sd shell, one expects the low energy negative parity states to consist predominantly of excitations into the fp shell. A calculation including both the sd and fp shell must involve some truncation of the model space otherwise the basis dimension is too large and matrix diagonalization becomes unmanageable. The simplest viable truncation scheme includes the $1d_{3/2}$, $2s_{1/2}$, $1f_{7/2}$ and $2p_{3/2}$ subshells. The largest basis dimension, with the population of the fp shell limited to at most three particles, was 588 occurring for the $J^\pi=3^-$ states.

Two interactions for this model space have been studied recently. The first, by Hasper (Ha79), used a modified surface-delta interaction with the strength parameters optimized separately for positive and negative parity states of nuclei in the region $A=36-39$. As well as not predicting the relative excitation energy of the positive and negative parity states, this interaction also calculates a large amount of mixing between the sd and fp configurations which is not supported by measurements, particularly in the lower end of the mass region (VE82, NV84).

Accordingly van der Poel et al. (VE82) derived a single set of two-body matrix elements and single particle energies for both positive and negative parity states for

A=34-39 nuclei. They assumed a surface-delta interaction for the residual interaction with the strength parameters and single-particle energies obtained from a least-squares fit to the excitation energies of 37 well-established levels in the nuclei ^{33}S , ^{33}P , ^{34}S , ^{34}Cl and ^{35}Cl . Although the interaction was initially derived to study high spin states in these nuclei, it has also been used successfully to explain lower spin states in ^{37}Cl (NV84). In that nucleus a one-to-one correspondence resulted between shell model states and experimentally observed states below 5 MeV with an average deviation of 300 keV. The discrepancy in excitation energy was most pronounced for the low-lying positive parity states. A similar discrepancy has been observed for calculations in all nuclei in this range and is known to be due to the low single-particle energy spacing $\epsilon(1f_{7/2}) - \epsilon(1d_{3/2})$. Our interest, however, is in the negative parity states and their excitation energy relative to the positive parity ground state. In this respect the predictions of this interaction have been demonstrated to give excellent agreement with observations in this region.

The configuration spaces considered in the calculations mentioned above with the VDP interaction all had the form $(1d_{3/2}, 2s_{1/2})^a (1f_{7/2}, 2p_{3/2})^b$ where $a+b=A-28$ and A is the number of nucleons. Limitations on the size of the calculations restricted the space to configurations with $b = 0$ or 2 for positive parity states and $b=1$ for negative parity

states. For the nucleus ^{34}P , with only 6 valence nucleons outside a closed ^{28}Si core, it was possible to also include configurations with up to three nucleons in the fp shell. Two calculations were performed for the negative parity states; the first with $b = 1$ and the other with $b = 1$ or 3. The low-lying states in the level scheme obtained with the two different configuration spaces had similar wavefunctions and relative excitation energies. However, the states predicted using the larger configuration space were shifted down in excitation energy by one MeV compared to those obtained with the smaller configuration. Because this interaction has been successfully used previously for configuration spaces with only one single particle in the fp-shell, the calculation results presented here, are those using the smaller configuration space. Hence, the lowest negative parity states in ^{34}P , which are expected to consist mostly of single particle excitations into the fp shell, should be well reproduced with this calculation.

The spectrum for negative parity states is displayed in the right hand side of Figure 5.1. The two lowest excited states are the 3^- and 4^- member of the configuration $[(1d_{3/2})_0^2 (2s_{1/2})_{1/2}^3 (1f_{7/2})_{7/2}^1]_{3^-,4^-}$ while the dominant configuration for the next two excited states is $[(1d_{3/2})_0^2 (2s_{1/2})_{1/2}^3 (2p_{3/2})_{3/2}^1]_{1^-,2^-}$. There is no experimental evidence for the natural parity 3^- state predicted at 1.6 MeV, however the 4^- could correspond to the observed level

at 2.31 MeV. Above this energy the large number of predicted states renders establishment of a correspondence with measured energy levels impossible. Also, above 3 MeV the validity of the calculation is dubious since configurations with holes in the $d_{5/2}$ subshell, predicted to be dominant for states above this excitation energy by Wildenthal and Chung's full sd -shell calculation, are not considered in this present calculation.

CONCLUSION

The usefulness of Litherland and Ferguson method II angular correlations using polarized beam, combined with tensor analyzing power measurements at zero degrees has been demonstrated in application to spin and parity assignments in the odd-odd nucleus ^{34}P . The advantages of a polarized deuteron beam in this method, where two polarization states yield two independent correlations, was first studied by Jones et al. (JG75). The results of their study for initial spin values $J_1 \leq 4$ have been summarized in Figure 1.2. The assumptions of 100% polarized beam and detection of the outgoing particle at zero or 180° in this study had to be relaxed in the analysis of measured angular correlations. These two factors lead to the population of substates in the residual nucleus other than the selected beam substate, with a magnitude which necessarily depends on the nuclear reaction mechanism. In chapter one it was shown that the measurement of reaction yields for both beam substates combined with an order of magnitude estimate for the finite angle correction, based on a first order expansion of the particle detector efficiency tensor about the z-axis,

permitted a unique determination of the population parameters for the residual nucleus. This eliminated the one variable describing the orientation of the initial state and allowed a simultaneous minimization of the combined chi-square for the two correlations in the parameter space consisting of $w_0^{m=0,1}$ and δ .

The spin and parity assignments for the low-lying excited states in ^{34}P , obtained using these techniques, are in complete agreement with the shell model calculations using Wildenthal's universal sd-shell interaction (see Figure 5.1). Assignments of definite spin values were limited to these low-lying states since the level density at higher excitation energy was too high and the levels were not strongly populated.

The most important factor affecting the ability to make spin and parity assignments using this technique was the large uncertainty in the measured correlation points due to poor statistics. Unfortunately, areas where changes could potentially result in an increased count rate are constrained for various reasons;

- (1) Increasing the target current would result in a higher singles count rate in the gamma-ray detector and the ratio of real to random coincidences, which varies inversely with the current, would decrease.
- (2) An increase in the target thickness is limited since the resulting increase in energy loss of the

alpha particles would deteriorate the particle resolution.

- (3) The particle detector solid angle cannot be increased since this would destroy the aligned geometry required for method II angular correlations.
- (4) Similarly, increasing the gamma-ray detector efficiency by increasing the solid angle subtended would result in greater attenuation of the observed correlation.

Although the statistical uncertainty of the measurements could not be improved upon within the bounds set by the experimental method, improvements in the resolution of the NaI detectors would have been possible. Evidence of this is contained in Table 4.2 which shows an increase of 20 percent in the FWHM for in-beam compared with source detection. This deterioration in the resolution is attributable to gradual gain shifts in the detectors caused by the high singles count rate. These gain shifts could be eliminated through the use of a gain stabilization system. One such system could be a pulsed LED mounted on the side of the crystal, whose signal out of the photomultiplier stage would be recorded and used later to calculate a gain correction. Given sufficient interest in setting up a dedicated facility to do this type of measurements, one could justify the laborious task of installing such a gain stabilizing system for every NaI detector.

In conclusion, method II ($d, \alpha\gamma$) angular correlations combined with the tensor analyzing power measurements, T_{20} , at zero degrees have proved useful in measuring the spin and parity of the low-lying levels in the neutron rich isotope ^{34}P .

APPENDIX

A DERIVATION FOR THE SIMPLE γ -RAY CORRELATION

Several sources in the literature comprise a complete formulation of angular correlation theory with applications to diverse problems in nuclear physics. The principal reference consulted for the following derivation was that by Ferguson (Fe65). His notation, using statistical and efficiency tensors, ρ_{kq} and ϵ_{kq} , analogous to the respective tensors used in polarization measurements, was employed. In the end, the final expression was written using the notation of Rose and Brink (RB67) since their notation and, specifically, their definition of the mixing ratio in terms of the reduced matrix elements for the electromagnetic operators, is used extensively in shell model calculations and in the analysis of correlation data.

The simplest γ -ray correlation occurs when the angular distribution of the γ -ray decay of the residual nucleus populated in a nuclear reaction is measured relative to the beam direction (z -axis). This simple case is depicted in Figure 1.1 of chapter one.

As discussed in chapter one, the angular distribution yield can be expressed as a product of the statistical tensor of the reaction products, ρ_{kq} , and the efficiency tensor, ϵ_{kq}^* , for detecting these products. That is,

$$W = \sum_{kq} \rho_{kq} \epsilon_{kq}^* \quad (\text{A.1})$$

The efficiency tensor is analogous to that in (1.7), aside from the normalization, and the statistical tensors of equations (1.1) and (A.1) are related by,

$$\rho_{kq}^s = (\hat{s})^{-1} t_{kq}^s, \quad \text{with } \hat{s} \equiv \sqrt{2s+1}.$$

In this simple example the emitted particle is not detected and the reaction products considered include the residual nucleus in state J_2 and the emitted γ -ray. The angular distribution function is then,

$$W(\theta) = \sum \rho_{k_2 q_2}(J_2) \rho_{kq}(L) \epsilon_{k_2 q_2}^*(J_2) \epsilon_{kq}^*(L), \quad (\text{A.2})$$

where the sum runs over k_2 , q_2 , k , and q . Note that the above expression holds for well-defined spins, J_2 , and a pure γ -ray transition of multipolarity L . In order to express $W(\theta)$ in terms of the spin of the initial state J_1 , which is usually the desired quantity, one needs to relate the statistical tensor for the coupled J_2 and L to that for J_1 , where $\vec{J}_1 = \vec{J}_2 + \vec{L}$. These are related as follows;

$$\rho_{k_2 q_2}(J_2) \rho_{k q}(L) = \sum_{k_1 q_1} \rho_{k_1 q_1}(J_1) (k_2 q_2, k q | k_1 q_1) \begin{Bmatrix} J_2 & L & J_1 \\ J_2 & L & J_1 \\ k_2 & k & k_1 \end{Bmatrix} \\ \times (\hat{J}_1)^2 \hat{k}_1 \hat{k} \times |\langle J_2 | L | J_1 \rangle|^2. \quad (\text{A.3})$$

The first factor in the summation is the statistical tensor for the initial state J_1 . The next two terms are a Clebsch-Gordan coefficient, $(\quad |)$, and a 9-j symbol, $\{ \quad \}$, which contain the angular momentum coupling algebra. The last factor is the modulus of the reduced matrix element for the electromagnetic operator of multipolarity L effecting the transition, and which, by definition, is proportional to the transition probability.

Since the residual nucleus is not detected its efficiency tensor is equivalent to that of a detector with 4π solid angle which cannot have any tensorial moments. Therefore,

$$\epsilon_{k_2 q_2}^* = \hat{J}_2 \delta_{k_2, 0} \delta_{q_2, 0}.$$

With this reduction the C-G coefficient and the 9-j symbol in (3) can be rewritten

$$(00, k q | k_1 q_1) = \delta_{k, k_1} \delta_{q, q_1} \\ \text{and } \begin{Bmatrix} J_2 & L & J_1 \\ J_2 & L & J_1 \\ 0 & k & k \end{Bmatrix} = \frac{(-)^a}{J_2 k} W(J_1 L, J_1 L; J_2 k) \quad (\text{A.4})$$

In the above equations $\alpha = J_2 - J_1 + l + k$ and W is a Racah coefficient (Fe65). Substituting into the equation for the angular distribution yields,

$$W(\theta) = \sum_{kq} \rho_{kq}(J_1) (-)^{\alpha} (\hat{J}_1)^2 W(J_1 L J_1 L; J_2 k) |\langle J_2 | L | J_1 \rangle|^2 \times \epsilon_{kq}^*(L) \quad (A.5)$$

It should be noted that the reduced matrix element contains all the nuclear structure information and does not have any angular dependence.

The explicit angular dependence can be obtained by evaluating the efficiency tensor for the γ -ray detector. The general case of two multipolarities L and L' is presented here and the case of one γ -ray multipolarity is obtained by letting $L=L'$. Using the transformation properties for tensors under rotation, the efficiency tensor for a cylindrical, polarization insensitive γ -ray detector with its symmetry axis along the z -axis is,

$$\epsilon_{kq}^0(LL') = 8\pi C_{k0}(LL') J_k \delta_{q,0} \quad (A.6)$$

where $J_k = \int_{\theta} \epsilon(\theta') P_k(\cos\theta') \sin\theta' d\theta'$.

$\epsilon(\theta')$ is the efficiency of detector material and the integration is over the active volume of the detector. The J_k 's represent the attenuation of the finite detector relative to the same efficiency 'point' detector. Thus, the attenuation

coefficients are defined as

$$Q_k = \frac{J_k}{J_0} \quad (\text{A.7})$$

The radiation parameter, $C_{k0}(LL')$, takes into account the coupling of the γ -ray spin and angular momentum;

$$C_{k0}(LL') = (-)^{L'-1} \left(\frac{\hat{L} \hat{L}'}{8\pi} \right) (L1, L'-1|k0) \quad (\text{A.8})$$

The superscript '0' on ϵ in equation (6) denotes the orientation of the detector symmetry axis along the z-axis. Applying a rotation to the detector to place it at (θ, ϕ) in the laboratory frame yields,

$$\epsilon_{kq}(LL'; \theta\phi) = D_{q0}^k(\theta, \phi) \epsilon_{k0}^0(LL') \quad .$$

The rotation matrices, D_{q0}^k , are related to the spherical harmonic functions,

$$D_{q0}^k(\theta, \phi) = \frac{\sqrt{4\pi}}{k} Y_{kq}^*(\theta, \phi) \quad ,$$

and substituting with (6) and (8), the expression for the efficiency tensor becomes,

$$\epsilon_{kq}(LL'; \theta\phi) = (-)^{L'-1} \frac{\sqrt{4\pi}}{k} \hat{L} \hat{L}' (L1, L'-1|k0) J_k Y_{kq}^*(\theta, \phi) \quad .$$

Substituting for the efficiency tensor in equation (2) for

the angular correlation yields:

$$W(\theta, \phi) = \sum_{kq} \rho_{kq}(J_1) (-)^{q+L-1} \left(\frac{\sqrt{4\pi}}{k} \right) (\hat{L} \hat{J}_1)^2 (L1, L-1|k0) \\ \times W(J_1 L J_1 L; J_2 k) |\langle J_2 | L | J_1 \rangle|^2 J_k Y_{kq}(\theta, \phi). \quad (A.9)$$

With the explicit angular dependence included in the correlation function one obtains that for a uniformly populated initial state J_1 , since the only non-vanishing statistical tensor is ρ_{00} , the angular distribution is isotropic, as expected. In the more general case, since the outgoing particles from the nuclear reaction are not detected the state populated in the residual nucleus will have axial symmetry and the components of the statistical tensor with $q \neq 0$ vanish. Also, for a scattering reaction with unpolarized beam, assuming the state J_1 has definite parity, the residual nucleus is aligned and ρ_{kq} is zero for odd k values. Therefore the sum in (9) is over even k only, and with $q=0$, the ϕ dependence disappears since,

$$\frac{\sqrt{4\pi}}{k} Y_{k0}(\theta, \phi) = P_k(\cos \theta).$$

Writing the correlation function with the notation of Rose and Brink (RB67) since this was the notation used in the analysis program, we make use of the following correspondences:

$$B_k(J_1) = \hat{J}_1 \rho_k(J_1)$$

$$R_k(LL'J_1J_2) = (-)^{\alpha'} \hat{J}_1 \hat{L} \hat{L}' (L1, L'-1 | k0) W(J_1 L J_1 L'; J_2 k)$$

$$\text{with } \alpha' = 1 + J_1 - J_2 + L' - L - k$$

With this notation the γ -ray angular correlation function for a particle -induced reaction, where the γ -ray is emitted by the initial state populated in the residual nucleus, becomes

$$W(\theta) = W_0 \sum_{k \text{ even}} B_k(J_1) R_k(LL'J_1J_2) Q_k P_k(\cos\theta) \quad (\text{A.10})$$

where $W_0 = |\langle \quad \rangle|^2 J_0$, and Q_k is defined in (7).

The normalization W_0 is chosen such that the $k=0$ coefficient of $P_k(\cos\theta)$ in the sum is unity.

For the more general case one has to allow for more than one multipolarity for the γ -ray transition, and for nuclear states with definite parity one expects only two multipolarities to contribute; $L=|J_1-J_2|$ and $L'=L+1$. In this case the initial expression for the correlation, (2), would include a coherent sum over both multipolarities. If the mixing ratio, δ , is defined as the ratio of the reduced matrix elements for the electromagnetic operators in the following way,

$$\delta \equiv \frac{\langle J_1 | L+1 J_2 \rangle / (2L+3)^{1/2}}{\langle J_1 | L J_2 \rangle / (2L+1)^{1/2}} \quad (\text{A.11})$$

then the correlation function can be written as,

$$W(\theta) = W_0 \sum_{k \text{ even}} B_k(J_1) R_k(J_1 J_2) Q_k P_k(\cos \theta) \quad (\text{A.12})$$

$$\text{where } R_k(J_1 J_2) \equiv \{ R_k(LLJ_1 J_2) + 2\delta R_k(LL'J_1 J_2) + \delta^2 R_k(L'L'J_1 J_2) \} (1+\delta^2)^{-1}$$

Again the normalization W_0 is chosen such that the coefficient of $P_0(\cos \theta)$ is unity.

Method II angular correlations

In deriving the expressions in (10) and (12) no information about the nuclear reaction producing the residual nucleus was considered except the incident-beam direction which was used to define the quantization axis in order to exploit the cylindrical symmetry of the problem. For a complete discussion of method II angular correlations one should carry through the expansion of the statistical tensor, $P_{kq}(J_1)$, in (9) and obtain an expression in terms of the incident beam and the appropriate reduced matrix elements for the operators effecting the nuclear reaction. As well, the efficiency tensor for the particle detector must be included in the expression for $W(\theta)$ where it must be evaluated for the particular detector geometry. This

derivation has been outlined in the original paper on method II angular correlations (LF61). The resulting expression is discussed in section 1.3.2.

Ultimately one is interested in determining the population parameters of the initial state J_1 . The method employed in section 1.3.4 to determine the population parameters treats the nuclear reaction as a black box and expresses the density matrix of the ensemble of residual nuclei in terms of that of the incident polarized beam;

$$\rho_{mn}^{\text{out}} = \sum_{\mu\nu} F_m^\mu \rho_{\mu\nu}^{\text{in}} F_n^{\nu*} .$$

Using this approach one is able to estimate the effects of less than 100% polarized beam and a finite detector solid angle on the population parameters.

REFERENCES

- (AB85) - F. Ajzenberg-Selove, R.E. Brown, E.R. Flynn and J.W. Sunier, Phys. Rev. C32 (1985) 756.
- (AF77) - F. Ajzenberg-Selove, E.R. Flynn, S. Obersen and J.W. Sunier, Phys. Rev. C15 (1977) 1.
- (BC80) - B.A. Brown, W. Chung and B.H. Wildenthal, Phys. Rev. C22 (1980) 774.
- (Be69) - P.R. Bevington, Data Reduction and Error Analysis for the Physical Sciences (McGraw-Hill 1969)
- (BE84) - B.A. Brown, A. Etchegoyen, W.D.M. Rae and N.S. Godwin, OXBASH (1984; unpublished)
- (BG77) - P.J. Brussard and P.W.M. Glaudemans, Shell-Model Applications in Nuclear Spectroscopy (North-Holland 1977)
- (BH70) - H.H. Barschall and W. Haerberli, editors of the Proceedings of the Third International Symposium on Polarization Phenomena in Nuclear Reactions (U of Wisconsin Press, Madison 1970)
- (Bo84) - D.O. Boerma, PFIT (1984; private communication)
- (BZ78) - Yu.A. Babenko, K.I. Zherebtsova, V.N. Kuz'min, Yu.A. Nemilov, L.M. Solin, E.D. Teterin and V.S. Romanov, Izvest. Akad. Nauk. (ser. fiz.) 42 (1978) 205.
- (DF85) - P.V. Drumm, L.K. Fifield, R.A. Bark, M.A.C. Hotchkis, C.L. Woods and P. Maier-Komor, Nucl. Phys. A441 (1985) 95.
- (En79) - P.M. Endt, "Strengths of Gamma-Ray Transitions in A=6-44 Nuclei (III)" in Atomic Data and Nuclear Data Tables 23 (1979) 3.
- (EV78) - P.M. Endt and C. VanDerLeun, "Energy Levels of A=21-44 Nuclei (VI)", Nucl. Phys. A310 (1978).
- (Fe65) - A.J. Ferguson, Angular Correlation Methods in Gamma-Ray Spectroscopy (North-Holland 1965).

- (GD73) - D.R. Goosman, C.N. Davids and D.E. Alburger, Phys. Rev. C8 (1973) 1324.
- (GR58) - H.E. Gove and A.R. Rutledge, "Finite Geometry Corrections to Gamma-Ray Angular Correlations Measured with 5 in. diameter by 4 in. long NaI(Tl) Crystals" AECL Chalk River Project CRP-755 (1958).
- (Ha79) - H. Hasper, Phys. Rev. C19 (1979) 1482.
- (He66) - R.L. Heath, Nucl. Inst. and Meth. 43 (1966) 209.
- (HL64) - W.F. Hornyak, C.A. Ludemann and M.L. Roush, Nucl. Phys. 50 (1964) 424.
- (JG75) - G.D. Jones, P.W. Green, J.A. Kuehner and D.T. Petty, Nucl. Inst. and Meth. 129 (1975) 527.
- (LF61) - A.E. Litherland and A.J. Ferguson, Can. J. Phys. 39 (1961) 788.
- (Ma82) - P. Maier-Komor, Proceedings of 11th World Conference of the International Nuclear Target Development Society (Seattle 1982) 164.
- (Mc76) - J.W. McKay, M.Sc. thesis, McMaster University 1976.
- (MR75) - R.G. Markham and R.G.H. Robertson, Nucl. Inst. and Meth. 129 (1975) 131.
- (MY68) - J.B. Marion and F.C. Young, Nuclear Reaction Analysis Graphs and Tables (North-Holland 1968).
- (NA77) - A.M. Nathan and D.E. Alburger, Phys. Rev. C15 (1977) 1448.
- (NV84) - G.J.L. Nooren and C. VanDerLeun, Nucl. Phys. A423 (1984) 197.
- (Oh70) - G.G. Ohlsen, "Los Alamos Lamb-Shift Polarized Ion Source: A User's Guide", Los Alamos Scientific Laboratory Report LA-4451 (1970).
- (Pe76) - D.T. Petty, Ph.D. thesis, McMaster University 1976.
- (PW72) - B.M. Freedom and B.H. Wildenthal, Phys. Rev. C6 (1972) 1633.
- (RB67) - H.J. Rose and D.M. Brink, Rev. of Mod. Phys. 39 (1967) 306.

- (Ro53) - M.E. Rosé, Phys. Rev. 91 (1953) 610.
- (RR84) - S. Raman, W. Ratynski, E.T. Journey, M.E. Bunker and J.W. Starner, Phys. Rev. C30 (1984) 26.
- (Si74) - M. Simonous, "Theory of Polarization Measurements, Observables, Amplitudes and Symmetries" in Lecture Notes in Physics Vol.30 (Springer 1974) 38.
- (Tw73) - P.J. Twin, Nucl. Inst and Meth. 106 (1973) 481.
- (TW63) - P.J. Twin and C.J. Willmott, Nucl. Inst. and Meth. 22 (1963) 109.
- (VE82) - C.J. VanDerPoel, G.A.P. Engelbertink, H.J.M. Aarts, D.E.C. Scherpenzeel, H.F.R. Arciszewski and B.C. Metsch, Nucl. Phys. A373 (1982) 81.
- (WC79) - B.H. Wildenthal and W. Chung, "Implications of Experimental Magnetic Moment Values in Light Nuclei for the Presence and Characteristics of Mesonic Exchange Currents" in Mesons in Nuclei Vol.2 edited by M. Rho and D.H. Wilkinson (North-Holland 1979) 721.
- (WC83) - B.H. Wildenthal, M.S. Curtin and B.A. Brown, Phys. Rev. C28 (1983) 1343.
- (We63) - C. Weitkamp, Nucl. Inst. and Meth. 23 (1963) 13.
- (Wi76) - G.B. Wilkin, M.Sc. project thesis, McMaster University 1976.
- (Wi82) - B.H. Wildenthal, Bull. Am. Phys. Soc. 27 (1982) 725.